Surface plasmon-coupled emission for applications in biomedical diagnostics

BY

Michal Trnavsky, MEng.

A thesis presented to Dublin City University

for the Degree of Doctor of Philosophy

Research supervisors:

Prof. Brian MacCraith, Prof. Colette McDonagh

School of Physical Sciences

National Centre for Sensor Research

Dublin City University

July 2009

Declaration

I hereby certify that this material, which I now submit for assessment on the programme of study leading to the award of Doctor of Philosophy is entirely my own work, that I have exercised reasonable care to ensure that the work is original, and does not to the best of my knowledge breach any law of copyright, and has not been taken from the work of others save and to the extent that such work has been cited and acknowledged within the text of my work.

Signed: ..... (Candidate) ID No.: .....

Date: .....

Acknowledgements

First of all, I would like to thank Prof. Brian MacCraith and Prof. Colette McDonagh for giving me an opportunity to carry out my Ph.D. study in your group, for your supervision and (sometimes) great deal of patience throughout, and, importantly, for the financial support.

I would like to thank to Dr. Thomas Ruckstuhl, close collaboration with you was enjoyable, and many discussions on the usefulness of the supercritical fluorescence detection and plasmonics were very stimulating. Next, I'd like to thank to Prof. Jörg Enderlein for collaboration and providing the numerical models for calculation of the fluorescence emission profiles.

The invaluable input of Dr. Jongseol Yuk is very much appreciated; without your expertise in assay development and surface plasmon resonance I would not be able to finish this work.

A big thank should be given to Dr. Helen Burke, who introduced me into the lab and supervised my first steps in the OSL. Next, to Dr. Robert Nooney and later Dr. Vladimir Gubala for patiently answering my questions regarding general and surface chemistry.

I would also like to thank to Des Lavelle and Pat Wogan; thanks to your skills and craftsmanship all setups worked as they should and every problem was eventually sorted.

For their help and friendship I would like to thank to Ondra Stranik, Bob Blue, Conor Burke, Rob Nooney and Scott Spillman and later Duncan Hill, Vlado Gubala, Jongseol Yuk and Ivan Dimov.

Finally, I would like to thank my parents for their support and my wife Darina for her love and encouragement during my stay in Ireland.

Table of Contents

Abstract

Surface plasmon-coupled emission (SPCE) is a phenomenon whereby the light emitted from a fluorescent molecule can couple into the surface plasmon of an adjacent metal layer resulting in highly directional emission in the region of the surface plasmon resonance (SPR) angle. As well as the high directionality of emission, SPCE has the added advantage of surface selectivity in that the coupling depends on the distance from the surface. This effect can be exploited in bioassays whereby a fluorescing background from the sample can be suppressed.

This thesis reports, both theoretically and experimentally, the SPCE effect for a fluorophore-spacersilver layer system. Both the angular dependence and the dependence of SPCE emission intensity on fluorophore-metal separation were investigated. It is demonstrated that SPCE leads to lower total fluorescence signal than that obtained in the absence of a metal layer (e.g. when a supercritical angle fluorescence approach is adopted). The experimental results are in good agreement with the theoretical model and with recently published work. Despite the lower overall intensities achievable with SPCE, the advantages of highly directional emission and surface selectivity make it a useful tool for development of high performance fluorescence-based biosensors.

The SPCE principles were exploited to achieve an enhanced optical bioassay using a novel, disposable parabolic biochip. This biochip is designed to capture the light generated near the interface with high efficiency. The plasmonic structure is integrated into the chip by depositing a thin metal film on top of the recognition area and by carrying out appropriate surface modification. An optical reader was designed and validated by raytracing simulations and aspects of illumination and polarisation were broadly discussed. The use of various materials was assessed in terms of both their chemical stability and compatibility with the biochip design. The proof-of-concept has been demonstrated by performing a model human Immunoglobulin G sandwich immunoassay and a limit of detection below 5ng/ml of the analyte was achieved. Real time antibody-antigen binding was also demonstrated.

This works shows the potential of SPCE to become a useful analytical technique which has a high degree of surface sensitivity and the inherent capability to reject background luminescence. Among the additional advantages are compatibility with the electrochemi-luminescence (ECL) technique and multiwavelength discrimination.

Abbreviations and Symbols

αhIgG*	labelled anti-human Immunoglobulin G
ϵ'	real part of dielectric constant
ϵ''	imaginary part of dielectric constant
μg	microgram
μg.ml^{-1}	microgram per millilitre
k_x''	imaginary part of surface plasmon propagation constant
k_x'	real part of surface plasmon propagation constant
k_{nr}	non-radiative decay rate
k_r	radiative decay rate
f	focal length
k	index of absorption
n	refractive index
Ab	antibody
Ab*	detection (labelled) antibody
ADE	angular distribution of emission
Ag	silver; also antigen
Al	aluminium
Au	gold
BSA	bovine serum albumin
cAb	primary (capture) antibody
CCD	charge-coupled device
Cr	chromium
dH_2O	deionised water
ECL	electrochemiluminescence
EDC	1-ethyl-3-(3-dimethylaminopropyl)-carbodiimide
H_2O_2	hydrogen peroxide
hIgG	human Immunoglobulin G
LbL	layer-by-layer

LOD ..... limit of detection
LOQ ..... limit of quantification
mbar ..... millibar
mg ..... milligram
ml ..... millilitre
mM ..... millimolar
MPTMS ..... 3-mercaptopropyl trimethoxysilane
MUA ..... 11-mercaptoundecanoic acid
N_2 ..... nitrogen
NA ..... numerical aperture
NaCl ..... sodium chloride
$ng.ml^{-1}$ ..... nanogram per millilitre
NH_4OH ..... ammonium hydroxide
NHS ..... N-Hydroxysuccinimide
nm ..... nanometer
$nm.s^{-1}$ ..... nanometer per second
PAC ..... poly(acrylic acid)
PAH ..... poly(allylamine) hydrochloride
PBS ..... phosphate buffered saline
PBST ..... phosphate buffered saline + 0.1% Tween20
PEL ..... polyelectrolyte
pH ..... negative logarithm of the activity of dissolved hydrogen ions
pKa ..... negative logarithm of an acid dissociation constant
PMT ..... photomultiplier
PSS ..... poly(styrene sulfonate)
SAF ..... supercritical angle fluorescence
SAM ..... self-assembled monolayer
SiO_2 ..... silicon dioxide; silica
SP ..... surface plasmon
SPCE ..... surface plasmon-coupled emission
SPR ..... surface plasmon resonance
TIRF ..... total internal reflection fluorescence

Chapter 1

Introduction

1.1 Introduction

In recent years, there has been an increasing need for highly sensitive detection methods for biomedical applications such as DNA analysis and affinity-based bioassays. In particular, fluorescence-based detection, using fluorescently-labelled biomolecules, has been established as a highly sensitive technique for detecting low concentrations of analyte. However, there is constant demand for increased sensitivity which will allow the detection of even smaller analyte concentrations down to single molecule level. An additional requirement for many assays is the efficient discrimination of analyte emission from background fluorescence in the solution.

The work presented in this thesis investigates the phenomenon of surface plasmon-coupled emission (SPCE) and explores the use of this technique in fluorescence-based bioassay applications. This chapter presents a brief overview of the literature on optical biosensors and, in particular, on fluorescence-based biosensors. This is followed by a brief account of the structure of the thesis and finally a list of thesis objectives.

1.2 Optical biosensors: overview

An optical biosensor can be defined as a sensor device which makes use of optical principles for the transduction of a biochemical reaction into a suitable optical signal. They can be classified into two major groups [1]: catalytic-based and affinity--based sensors. The first group makes use of biocomponents capable of recognizing

(bio)chemical species and transforming them into a product through a chemical reaction. This type of biosensor is represented mostly by enzymatic biosensors, which make use of specific enzymes or their combinations. The result of the reaction is transferred into an optical signal and detected. The affinity-based sensor types make use of the specific capabilities of an analyte to bind to a biorecognition element. This group can be further divided into immunosensors, relying on specific interactions between an antibody and an antigen [2], nucleic acid biosensors, making use of the affinity between complementary oligonucleotides [3], and biosensors based on interactions between an analyte (e.g. whole cell) and a biological receptor. The recognition elements are most often bound to a the sensor surface thereby forming an active sensor area. With respect to the work presented in this thesis, the affinity-based sensors will be the focus.

The biomolecular interaction at the sensor surface modulates the optical characteristics of the transducer, such as intensity, phase, polarisation etc., and the sensing events can be quantified by the change in diverse optical properties such as absorption, refractive index and luminescence, among others. In recent years, research in the field of optical affinity-based biosensors has focused primarily on refractive index-based and luminescence/fluorescence-based sensor types.

1.2.1 Refractive index-based biosensors

In the former category of refractive index-based biosensors, the probing light wave is modulated by changes of the refractive index in the sensing layer due to the occurrence of binding events between analyte molecules, present in solution, and surface-bound receptors. The sensing of the refractive index changes usually happens via the evanescent tail of the probing optical wave, thereby confining the detection of the binding events very to close to the active sensor layer. The extent of the refractive index change depends on the concentration of the analyte and the parameters of the binding reaction, so the quantitative parameters of the interaction can be extracted. Several transduction schemes have been proposed, depending on the physical principle used to measure the refractive index modulations. They will be briefly described below.

Surface plasmon resonance-based sensors (SPR) are probably the best known. They

make use of the resonant coupling of the optical wave into the evanescent field at the metal-dielectric interface, where local changes of the refractive index induce changes in the condition for surface plasmon coupling. This can be measured as a change in coupling angle, wavelength or the intensity of the reflected light beam. Their attractiveness stems from the fact that no labels are required, the technology is extremely sensitive (down to 10^{-7} refractive index units) and is suitable for real time measurements. To date, large number of sensors have been developed for a wide range of applications in the detection of disease markers, food safety and environmental monitoring [4–6]. SPR-based sensors have been exploited commercially [7, 8]. Some modifications have also been performed for optimisation of the evanescent field so that detection of whole bacteria can be facilitated [9, 10].

Another approach, with design similar to that of SPR-based sensors, is that of the resonant mirror optical biosensor [11]. The system comprises four layers, a sensing layer, high refractive index waveguide layer, low refractive index coupling layer and a prism. Light is coupled into the prism block and at the resonant angle, passes through the low index layer and propagates within the high index layer. This results in an evanescent field in the sensing layer above, which, affected by changes in refractive index in the sensing layer, in turn causes changes in the resonant angle. Sensitivities comparable to those of SPR sensors can be achieved [12].

Techniques based on interferometry [12,13] represent another class of refractive index-based sensors. These sensors compare differences between two light beams; a sensing beam and a reference beam. When combined, they produce an interference pattern of light and dark fringes. A chemical or physical reaction occurring along one of the beams causes a change in the refractive index, which is detected by the evanescent field and results in a shift of the interference pattern. Planar waveguides are a common format for these sensors, due to their long interaction length. Fabrication and optimisation of these waveguides has been assisted by advances in the telecommunications and semiconductor industries, while fluidic design has been significantly improved due to microelectromechanical systems (MEMS) research.

Generally, a major limitation of refractive index-based sensors lies in their limited sensitivity due to the fact that the binding of small molecules results in only small signal changes. Another drawback is that these sensors are sensitive to temperature and

bulk refractive index changes. Also, they require high specificity of the binding layer to capture the target analyte and prevent non-specific binding to the surface, which could be recorded as a positive binding event.

1.2.2 Fluorescence-based biosensors

The drawbacks of the refractive-index based biosensors, which mainly act as label--free (the presence of the analyte molecule itself induces a change in the detected signal) can be overcome by use of detection of the binding event by means of labelled molecules. Extensive research has been carried out in the area of electrochemiluminescence (ECL)-based biosensors. One of the reasons for the popularity of ECL-based biosensors is the attractiveness of the labels, which are sensitive, inexpensive, nonhazardous and linear over a wide range [13].

The largest and most promising class of fluorescence-based biosensors is that employing fluorescent labels. This is due to the significant advantages that fluorophores display over other labels. These include ease of handling, high stability, spatial resolution, multianalyte detection, sensitivity, rapid detection, simple excitation and detection instrumentation and low total system cost with possibility of miniaturisation. Fluorescence-based biosensors typically measure changes in fluorescence intensity, lifetime or polarisation.

The demand for detection of very low concentrations of analytes has lead to the need for improvement in the sensitivity of the fluorescence-based sensors. There are a variety of possible ways of enhancing the performance of the sensors. The most obvious solution is the use of quality optics and a highly sensitive detection system. Currently, detection of single fluorescent molecules and even measurement of their orientation is possible [14, 15]. Therefore, even a single biomolecule could be detected leading to infinitesimally low limit of detection and the limitation of such a sensor would therefore be given by the diffusion rates of reagent (it would take too long for reagents to reach the biorecognition elements for very low concentration) and the affinity of the reagent-biorecognition element interaction (there is an equilibrium between the reagents attached to the substrate and the reagents in the solution). However, these single fluorescence detection systems are very expensive bench-top devices (for example systems from PicoQuant GmbH, Germany [16]) used only in laboratories requiring

skilled personnel and can not be implemented in low-cost, portable biosensors. For this reason, alternative simple, compact and cheap methods for enhancement of detection of the fluorescent signal are sought. Several strategies have been adopted to address the issue, such as plasmonic enhancement of the fluorescence of a single molecule, synthesis of labels encapsulating multiple dye molecules and optimisation of the fluorescence excitation and collection.

Techniques utilising localised surface plasmon resonance (LSPR) on metallic nanostructures have become of great research interest [17–19]. Optical properties of the metallic nanostractures can be tuned by their size, shape and composition. They can be prepared using a large range of techniques, either on a substrate (such as metallic nanoislands [20, 21] or as subwavelength holes in smooth metal films [22]) or in the form of colloidal nanoparticles [23]. Great capability of tailoring their properties renders them attractive for a large variety of applications.

The development of new ultra bright labels is also considered. This involves the chemical engineering of new molecules with desirable emission and excitation wavelengths to form a new class of labels, which can be silica nanoparticles doped with large amount of fluorophore [24] or quantum dots [25]. The advantages compared to a single conventional fluorophore are higher brightness and better photostability. For silica nanoparticles, the shift of the emission wavelength using two dyes incorporated into the particle can be utilised [26].

For the excitation a method called total internal reflection fluorescence (TIRF) has been widely used [27–29], taking advantage of the excitation by an evanescent wave. The extent of the evanescent wave into the solution is only few hundred nanometers, therefore, only the bound fluorophore-labelled molecules are excited and subsequently detected. A complementary effect to this is used in the supercritical angle fluorescence method (SAF) [30, 31]. Due to total internal reflection, fluorescence from unbound labelled molecules in solution will not be emitted into the substrate (the refractive index of the substrate is higher than that the of solution) at angles larger than the critical angle (61° for water-glass interface). However, a fluorophore in the proximity (less than emission wavelength) of an interface emits light into a highly anisotropical pattern and into angles larger than critical angle [32]. Therefore, the fluorescence from bound analytes can be distinguished from fluorescence from unbound analytes

by collecting the fluorescence light from angles above the critical angle [33]. The combination of TIRF and SAF yields a technique with extremely efficient surface discrimination.

Surface plasmon-coupled emission (SPCE), where a semitransparent metal film is deposited between the substrate and the biorecognition layer, is a somewhat similar technique to SAF [34–37]. The metallic layer causes molecules close to the interface to have a distinct angle-dependent emission with the majority of the fluorescence emitted into a very narrow angle range (section 2.4). Fluorescence from the unbound molecules in solution is not transmitted through the metallic layer, therefore only fluorescence from the bound analyte is detected. Enhanced fluorophore excitation near the metal film due to surface plasmon resonance can be achieved [38–40]. Because the angle into which fluorescence is emitted depends on the emission wavelengths, this gives the possibility of multianalyte detection [41]. The presence of the metallic film also makes this technique compatible with ECL-based detection [42, 43].

1.3 Thesis structure

This thesis deals with experimental and theoretical investigation of surface plasmon--coupled emission and its implementation into a novel optical biochip platform. The text is divided into five chapters.

Chapter 1 introduces the field of optical biosensors and gives an overview of the variety of used techniques, with focus on refractive index-based and fluorescence-based biosensors. An outline of the thesis is presented and the objectives of the work are stated.

Chapter 2 describes the theory of luminescence and the fundamental principles of its enhancement. Surface plasmon resonance effect on metal-dielectric interface is detailed. A radiating molecule is described as a dipolar emitter and the theoretical methodology addressing solution of the problem of a radiating molecule in the vicinity of a planar interface is briefly outlined. This is followed by description of the surface plasmon-coupled emission effect. Finally, a brief introduction into immunoassays is given.

Chapter 3 deals with experimental investigation of SPCE, namely the effect of metal-

fluorophore separation on the resultant angular distribution of emission, fluorescence intensity and its comparison with that detectable in the absence of metal film. The experimental data are compared to a numerical model.

Chapter 4 describes the development of the SPCE-based biochip platform. Firstly, the biochip, its design and basic properties are introduced. Integration of the SPCE structure into the chip is described next, and the practical considerations regarding the choice of materials are pointed out. Design of the chip reader and its validation are described next, together with the practical limitation imposed by illumination and polarisation issues. Following a description of the procedure of surface modification and antibody immobilisation, a sandwich bioassay is demonstrated using SPCE.

Finally, chapter 5 summarises the results achieved during the research and describes possible methodologies utilising the SPCE effect to enhance and optimise the performance of the SPCE-based biosensor platform.

1.4 Research objectives

The main research objectives are:

1. To experimentally investigate the surface plasmon-coupled emission effect on a planar surface in terms of the metal-fluorophore separation and to experimentally validate the theoretical model developed earlier.

2. To implement the SPCE structure into a novel parabolic biochip platform and design and validate device for reading-out signal from the biochip

3. To demonstrate a SPCE-based sandwich immunoassay on the parabolic biochip

References

[1] S. M. Borisov and O.S. Wolfbeis. Optical biosensors. *Chemical Reviews*, 108(2):423–461, 2008.

[2] P. B. Luppa, L. J. Sokoll, and D. W. Chan. Immunosensors - principles and applications to clinical chemistry. *Clinica Chimica Acta*, 314(1-2):1–26, 2001.

[3] A. Sassolas, B. D. Leca-Bouvier, and L. C. Blum. DNA biosensors and microarrays. *Chemical Reviews*, 108:109–139, 2008.

[4] J. Homola. *Surface Plasmon Resonance Based Sensors*, Volume 4 of *Springer Series on Chemical Sensors and Biosensors*. Springer, Heidelberg, 2006.

[5] J. Homola and S. S. Yee. Surface plasmon resonance sensors: review. *Sensors and Actuators B*, 54:3–15, 1999.

[6] J. Homola. Surface plasmon resonance sensors for detection of chemical and biological species. *Chemical Reviews*, 108(2):462–493, 2008.

[7] B. Liedberg, C. Nylander, and I. Lundstrom. Biosensing with surface-plasmon resonance - how it all started. *Biosensors & Bioelectronics*, 10(8):R1–R9, 1995.

[8] http://www.biacore.com.

[9] M. Zourob, S. Mohr, B. J. T. Brown, P. R. Fielden, M. B. McDonnell, and N. J. Goddard. Bacteria detection using disposable optical leaky waveguide sensors. *Biosensors & Bioelectronics*, 21:293302, 2005.

[10] M. Zourob, S. Mohr, B. J. T. Brown, P. R. Fielden, M. B. McDonnell, and N. J. Goddard. An integrated metal clad leaky waveguide sensor for detection of bacteria. *Analytical Chemistry*, 77(1):232–242, 2005.

[11] M. Zourob, S. Elwary, X. Fan, S. Mohr, and N. J. Goddard. Label-free detection with the resonant mirror biosensor. Volume 503 of *Methods in Molecular Biology*, p.89–138. Humana Press, Inc., 2009.

[12] L. M. Lechuga. Optical biosensors. In L. Gorton, editor, *Biosensors and Modern Biospecific Analytical Techniques*, Volume 44 of *Comprehensive Analytical Chemistry*. Elsevier, Amsterdam, 2005.

[13] F. Ligler and C. R. Taitt. *Optical Biosensors: Present and Future*. Elsevier, Amsterdam, 2002.

[14] A. P. Bartko and A. M. Dickson. Imaging three-dimensional single molecule orientations. *Journal of Physical Chemistry B*, 103:1123711241, 1999.

[15] P. Dedecker, B. Muls, A. Deres, H. Uji-i, J. Hotta, J. Sliwa, J.-P. Soumillion, K. Mullen, J. Enderlein, and J. Hofkens. Defocused wide-field imaging unravels structural and temporal heterogeneity in complex systems. *Advanced Materials*, 21(10–11):1079–1090, 2009.

[16] http://www.picoquant.com/.

[17] J. R. Lakowicz. Radiative decay engineering 5. metal-enhanced fluorescence and plasmon emission. *Analytical Biochemistry*, 337(2):171–194, 2005.

[18] J. R. Lakowicz, K. Ray, M. Chowdhury, H. Szmacinski, Y. Fu, J. Zhang, and K. Nowaczyk. Plasmon-controlled fluorescence: a new paradigm in fluorescence spectroscopy. *Analyst*, 133(10):1308–1346, 2008.

[19] A. J. Haes and R. P. Van Duyne. Preliminary studies and potential applications of localized surface plasmon resonance spectroscopy in medical diagnostics. *Expert Review of Molecular Diagnostics*, 4(4):527–537, 2004.

[20] C. L Haynes and R. P. Van Duyne. Nanosphere llithography: a versatile nanofabrication tool for studies of size-dependent nanoparticle optics. *Journal of Physical Chemistry B*, 105(24):55995611, 2001.

[21] Y. Fu and J. R. Lakowicz. Enhanced fluorescence of Cy5-labeled oligonucleotides near silver island films: A distance effect study using single molecule spectroscopy. *Journal of Physical Chemistry B*, 110(45):22557–22562, 2006.

[22] W. L. Barnes, A. Dereux, and T. W. Ebbesen. Surface plasmon subwavelength optics. *Nature*, 424(6950):824–830, 2003.

[23] O. Stranik. *Plasmonic enhancement of fluorescence for biomedical diagnostics*. PhD. Thesis, DCU Dublin, 2007.

[24] H. Ow, D. R. Larson, M. Srivanstana, B. A. Baird, W. W. Webb, and U. Wiesner. Bright and stable core-shell fluorescent silica nanoparticles. *NanoLetters*, 5(1):113117, 2005.

[25] X. Michalet, F. F. Pinaud, L. A. Bentolila, J. M. Tsay, S. Doose, J. J. Li, G. Sundaresan, A. M. Wu, S. S. Gambhir, and S. Weiss. Quantum dots for live cells, in vivo imaging, and diagnostics. *Science*, 307:538–544, 2005.

[26] L. Wang, Y. Chaoyoung, and W. Tan. Dual-luminophore-doped silica nanoparticles for multiplexed signaling. *Nano Letters*, 5(1):3743, 2005.

[27] M. N. Kronick and W. A. Little. New immunoassay based on fluorescence excitation by internal-reflection spectroscopy. *Journal of Immunological Methods*, 8(3):235–240, 1975.

[28] D. Axelrod, E. H. Hellen, and R. M. Fulbright. Total internal reflection fluorescence. In J. R. Lakowicz, editor, *Topics in Fluorescence Spectroscopy*, Volume 3. Springer, 1992.

[29] D. Axelrod. Total internal reflection fluorescence microscopy in cell biology. *Traffic*, 2(11):764–774, 2001.

[30] J. Enderlein, T. Ruckstuhl, and S. Seeger. Highly efficient optical detection of surface-generated fluorescence. *Applied Optics*, 38(4):724–732, 1999.

[31] T. Ruckstuhl, J. Enderlein, S. Jung, and S. Seeger. Forbidden light detection from single molecules. *Analytical Chemistry*, 72(9):2117–2123, 2000.

[32] W. Lukosz. Light-emission by magnetic and electric dipoles close to a plane dielectric interface: 3. radiation-patterns of dipoles with arbitrary orientation. *Journal of the Optical Society of America*, 69(11):1495–1503, 1979.

[33] T. Ruckstuhl, M. Rankl, and S. Seeger. Highly sensitive biosensing using a supercritical angle fluorescence (SAF) instrument. *Biosensors and Bioelectronics*, 18(9):1193–1199, 2003.

[34] J. R. Lakowicz. Radiative decay engineering 3. surface plasmon-coupled directional emission. *Analytical Biochemistry*, 324(2):153–169, 2004.

[35] J. Malicka, I. Gryczynski, Z. Gryczynski, and J. R. Lakowicz. DNA hybridization using surface plasmon-coupled emission. *Analytical Chemistry*, 75(23):6629–6633, 2003.

[36] E. Matveeva, Z. Gryczynski, I. Gryczynski, J. Malicka, and J. R. Lakowicz. Myoglobin immunoassay utilizing directional surface plasmon-coupled emission. *Analytical Chemistry*, 76(21):6287–6292, 2004.

[37] J. Borejdo, Z. Gryczynski, N. Calander, P. Muthu, and I. Gryczynski. Application of surface plasmon-coupled emission to study of muscle. *Biophysical Journal*, 91(7):2626–2635, 2006.

[38] T. Neumann, M. L. Johansson, D. Kambhampati, and W. Knoll. Surface-plasmon fluorescence spectroscopy. *Advanced Functional Materials*, 12(9):575–586, 2002.

[39] F. Yu, D. F. Yao, and W. Knoll. Surface plasmon field-enhanced fluorescence spectroscopy studies of the interaction between an antibody and its surface-coupled antigen. *Analytical Chemistry*, 75(11):2610–2617, 2003.

[40] F. Yu, B. Persson, S. Lofas, and W. Knoll. Attomolar sensitivity in bioassays based on surface plasmon fluorescence spectroscopy. *Journal of the American Chemical Society*, 126(29):8902–8903, 2004.

[41] E. Matveeva, J. Malicka, I. Gryczynski, Z. Gryczynski, and J. R. Lakowicz. Multi-wavelength immunoassays using surface plasmon-coupled emission. *Biophys. Biochem. Res. Comm.*, 313(3):721–726, 2004.

[42] J. Zhang, Z. Gryczynski, and J. R. Lakowicz. First observation of surface plasmon-coupled electrochemiluminescence. *Chemical Physics Letters*, 393(4-6):483–487, 2004.

[43] D. M. Koller, A. Hohenau, H. Ditlbacher, N. Galler, F. R. Aussenegg, A. Leitner, J. R. Krenn, S. Eder, S. Sax, and E. J. W. List. Surface plasmon coupled electroluminescent emission. *Applied Physics Letters*, 92, 2008.

Chapter 2

Theoretical background

This chapter reviews the theoretical concepts that are related to the work presented in this thesis. Firstly, molecular photoluminescence is explained in terms of an electron energy level model in molecules and the fundamental principles of fluorescence enhancement are briefly discussed. The radiating molecule is described as a dipolar emitter and it is shown how the emission pattern is altered when a radiating dipole is placed close to a refractive index discontinuity. Surface plasmon resonance at the smooth interface between metal and a dielectric is described, followed by a description of surface plasmon-coupled emission as a result of the fluorescence emission coupling into surface plasmons. In the last section, an overview of the fundamental principles of immunoassays, relevant to this work, is presented.

2.1 Photoluminescence and fluorescence

Photoluminescence is a process in which absorption of light photons by a molecule is followed by re-radiation of photons with lower energy. Generally, it is necessary that the molecule is brought into the excited state before it can emit radiation. Depending on the nature of the ground and the excited state, photoluminescence can be of two types: fluorescence and phosphorescence. In the case of fluorescence, the relaxation of a molecule to the ground state occurs rapidly, with radiative lifetimes typically $\sim 10^{-8}$ sec, whereas the typical radiative lifetime for phosphorescence is $\sim 10^{-3}$ sec.

A molecule can absorb a photon by promoting an electron to a higher excited state and/or by inducing rotational and vibrational transitions in the molecule. The energy levels in a molecule are discrete and depend on the molecular structure. A schematic representation of the energy levels of a molecule is shown in fig. 2.1. The transitions between electronic states typically occur in the UV to visible range ($\sim$1eV). Energies of vibrational and rotational

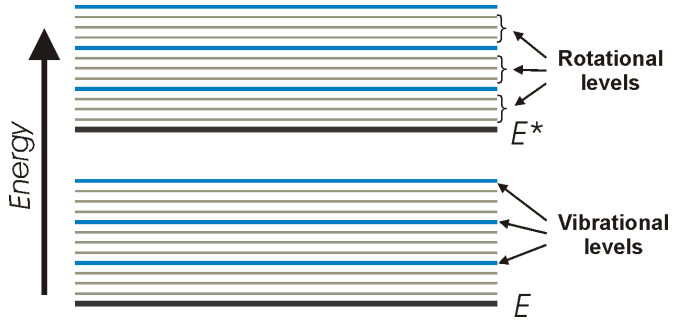

Figure 2.1: Schematic representation of a molecular energy level structure. The E and E^* levels correspond to the electronic states, which are further split into finer structure of vibrational and rotational levels

transitions correspond to infrared ($\sim$0.1eV) and microwave ($\sim$1meV) region respectively.

2.1.1 The absorption and emission process

The process of absorption and emission in a molecule is graphically illustrated by the Jabloński diagram shown in fig. 2.2. The photoluminescence process is initiated by the absorption of a photon by a molecule. Depending on the energy of the incident photon the molecule in the ground state (S_0) is promoted to higher excited states (S_1 or S_2). This absorption process, marked by blue arrows in fig. 2.2, is very fast, of the order of 10^{-15}sec.

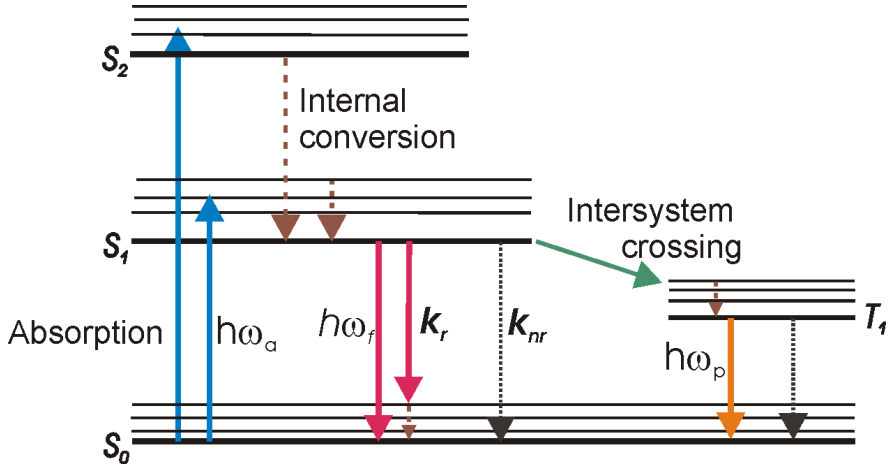

Figure 2.2: Jabloński diagram illustrating the photoluminescence process due to electron transitions from excited states to the ground state

Immediately after absorption the molecule relaxes via an internal conversion mechanism to the lowest excited state S_1. This relaxation process is very rapid, in the order of 10^{-12}sec. The de-excitation to the ground state can follow two pathways [1]: in the case of fluo-

rescence, where the transition occurs between two singlet states (spin of the molecule is maintained), typical transition times are of the order of 10^{-8}sec. This radiation process (denoted by k_r in fig. 2.2) can be accompanied by a decay through a non-radiative pathway (denoted by k_{nr}), which can be caused by either internal mechanisms or by external quenching. The parameters k_r and k_{nr} are called radiative and non-radiative decay rates respectively.

The phosphorescence process is characterised by an inter-system crossing from the singlet state S_1 to the so-called triplet state T_1. The inter-system crossing process is accompanied by a change of the total spin of the molecule. The triplet levels are generally lower in energy than singlet states. The triplet state can be de-populated by the same mechanisms as in the case of fluorescence, i.e. either by emission of the photon (illustrated by the yellow arrow in fig. 2.2) or by a non-radiative decay process. The transition from T_1 back to the ground state, accompanied by change of the electron spin, is forbidden (from the quantum mechanical point of view) and therefore the decay rates are much lower then in fluorescence (with decay times typically above 10^{-3}sec).

For both fluorescence and phosphorescence, the amount of energy released during the relaxation to the ground state is less than that absorbed, meaning that the emitted light occurs at a longer wavelength (lower energy) than the excitation. The difference in wavelength between absorption and emission maxima of a fluorescent molecule (illustrated for Cy5 molecule which was used in this work) is called the Stokes shift and is indicated by the arrow in fig. 2.3.

Fluorescence quantum yield and lifetime

The phenomenon of fluorescence quantum yield and lifetime can be explained with reference to the decay rates k_r and k_{nr} illustrated in the Jabloński diagram. Fluorescence quantum yield Q is defined as the number of photons emitted to the number of photons absorbed and can be expressed as [1]

$$Q = \frac{k_r}{k_r + k_{nr}} \tag{2.1}$$

where the parameters k_r and k_{nr} are defined above. The quantum yield can lie between 0 and 1 and, in practice, is always lower then unity because of the radiationless losses caused by collision mechanisms, effect of matrix, proximity to a quencher etc.

The lifetime τ of the excited state is defined as the average time the molecule spends in

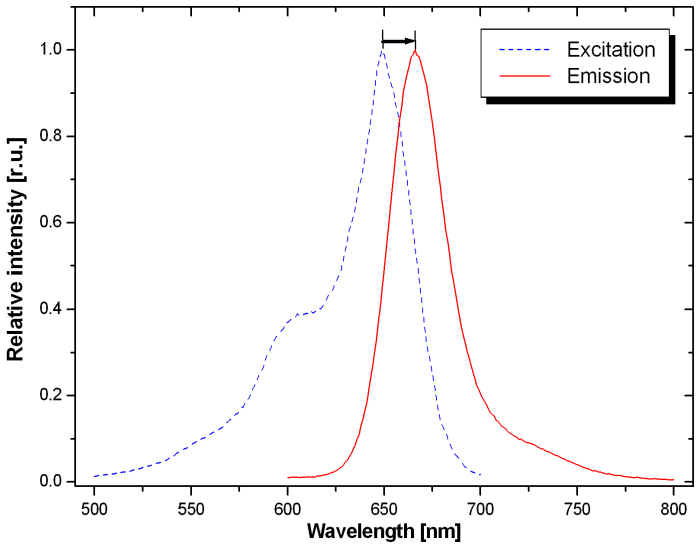

Figure 2.3: Normalised absorption and emission spectra of Cy5 dye. The black arrow indicates the Stokes shift

the excited state prior to return to the ground state and is given by

$$\tau = \frac{1}{k_r + k_{nr}} \tag{2.2}$$

Since the emission is a random process and only a few molecules will emit their photons at $t = \tau$, the lifetime is an average value of the time spent in the excited state. Modification of fluorescence lifetime and hence quantum yield can be achieved by factors which affect either of the rate constants.

Fluorescence quenching

Fluorescence quenching refers to any process which decreases the fluorescence intensity of a given substance. Depending on the nature of the molecule-quencher pair, a variety of processes can result in quenching. These include excited state reactions, energy transfer, complex formation and collisional quenching. A whole class of fluorescence-based optical sensors is based on measurements of quenching activity of analyte molecules. A particular type of fluorescence quenching, when a fluorophore is placed in the proximity of a metal, will be discussed further.

Photobleaching

Photobleaching occurs when a molecule permanently loses the ability to fluoresce due to photon-induced chemical damage or other modification. Molecules are prone to photo-

bleaching with increasing number of excitation and emission cycles and may also photobleach following exposure to excessive excitation intensity. Fluorophore photostability, expressed in terms of the average number of excitation and emission cycles that occur for a particular fluorophore before photobleaching or a period of continuous illumination with particular intensity before photobleaching, is dependent upon the molecular structure and the local environment. As an example, AlexaFluor 647 and Cy5 dyes used in this work exhibit almost identical excitation/emission properties (fig. 2.3), but the former offers significantly higher resistance to photobleaching [2].

2.1.2 Fundamental principles of fluorescence enhancement

The term fluorescence enhancement is defined as any process whereby a larger number of photons can be emitted by a single molecule. The graphical illustration of the excitation and emission process in a molecule in the Jabloński diagram suggests that engineering both the excitation and emission process can be used to enhance fluorescence.

As will be described in section 2.3.1, from the point of view of electromagnetic theory, the fluorophore molecule can be described as an oscillating dipole. If the absorption of a molecule is in the linear range (i.e. far from saturation), the absorption rate is proportional both to the intensity of the incident light and to the capability of the molecule to absorb light. The absorption rate also depends upon the orientation of the molecule to the excitation electric field, where molecules with their dipole moments perpendicular to the vector of the electric field are not excited. By placing a molecule into the environment which

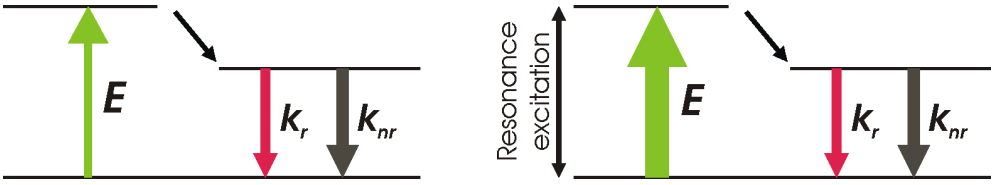

Figure 2.4: Simplified Jabloński diagram of the excitation enhancement process due to enhanced resonance illumination

enhances the field of the incident light, e.g. in the proximity of a metal nanostructure [3,4] or at a metal-dielectric interface [5]) the (locally) enhanced electric field in turn provides an enhanced excitation rate (fig. 2.4). Enhanced excitation may, however, result in saturation and eventual photobleaching of the molecule unless a mechanism providing sufficiently fast de-population of the excited state acts simultaneously.

As described by eq. (2.1) the modification of the decay rates will result in modification of

the quantum yield. Modification of a local environment of the molecule (e.g. by placing the molecule into the proximity of a metal) results in a creation of a new decay channel, described by decay rate k_m and illustrated by fig. 2.5. The quantum yield will then have the form

$$Q_m = \frac{k_r + k_{r,m}}{k_r + k_{nr} + k_{r,m} + k_{nr,m}} \tag{2.3}$$

where the k_m is expressed as the sum of the induced radiative rate $k_{r,m}$ and non-radiative rate $k_{nr,m}$. The corresponding fluorescence lifetime (eq. 2.2) changes to

$$\tau_m = \frac{1}{k_r + k_{nr} + k_{r,m} + k_{nr,m}} \tag{2.4}$$

It is clear from this equation that the lifetime τ_m is shorter than τ. An enhanced fluorescence emission can be achieved if the modified quantum efficiency Q_m is larger than the initial quantum efficiency of a dye. The emission enhancement strongly depends on the quantum

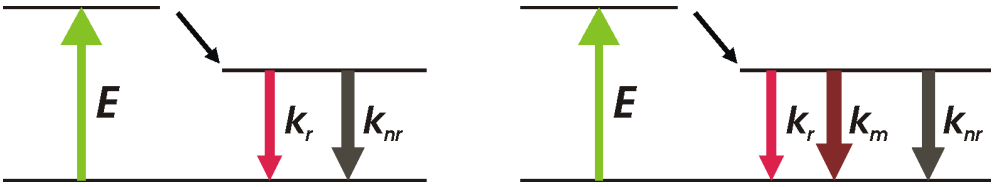

Figure 2.5: Simplified Jabloński diagram of the emission enhancement process due to creation of a new decay channel, described by decay rate k_m

efficiency of the dye. A dye with a low quantum efficiency has a non-radiative rate much larger than the radiative rate ($k_{nr} >> k_r$). Its quantum efficiency can be significantly enhanced provided that $k_{nr,m} << k_{r,m}$ and $k_{r,m} >> k_r$. From this it also follows that the fluorescence emission can not be increased significantly for a dye which has a high quantum efficiency and the only effect will be in shortening of the fluorescence lifetime τ, which can lead to increased photostability of the dye [6].

2.2 Surface plasmon resonance at a smooth surface

2.2.1 An evanescent wave at the interface of two dielectrics

An evanescent field at the interface of two dielectrics with refractive indices n_1 and n_2 (where $n_1 = \sqrt{\epsilon_1}$ and $n_2 = \sqrt{\epsilon_2}$) is produced by a light beam travelling in the medium with higher refractive index (n_1) which is incident upon an interface at an angle higher than the critical angle of the interface $\theta_c = \sin^{-1}(n_2/n_1)$. In the reflectivity curve shown in fig.

2.7a, the reflectivity as a function of the incidence angle θ reaches unity when the critical angle θ_c is approached, but the light intensity does not fall abruptly to zero in the second medium. There is instead a harmonic evanescent wave travelling parallel to the surface with an amplitude decaying exponentially normal to the surface. The penetration depth d (at which the field amplitude falls to $1/e$) is a function of the incidence angle θ and is written

$$d = \frac{\lambda}{2\pi\sqrt{(n_1^2 \sin^2\theta) - n_2^2}} \tag{2.5}$$

This penetration depth is of the order of the the wavelength λ of the incident light and decreases as the angle of incidence increases. The evanescent wave can be excited by both *s*- and *p*- polarisations of the incident light and the dependence of the evanescent wave intensity is similar for both polarisations. A moderate field enhancement of the evanescent wave of the order of 3 to 4 can be achieved at the critical angle of glass with $n = 1.52$ and water interface due to the constructive interference between the incident and reflected wave, and decreases with increasing angle of incidence [7].

2.2.2 Surface plasmon at a metal-dielectric interface

Surface plasmons (SPs) are electromagnetic waves that propagate along the surface of a conductor, usually a noble metal (such as Au, Ag, Pt, etc.). They are essentially light waves that are bound to the surface by the interaction with the free electrons of the conductor. As a result, the free electrons respond collectively by oscillating in resonance with the light wave. The resonant interaction between the surface charge oscillation and the electromagnetic field of the light constitutes the SP and gives rise to its unique properties.

2.2.2.1 Fundamental properties of surface plasmons

The condition for the existence of the surface plasmon resonance wave at a simple metal--dielectric interface is obtained by solving Maxwell's equations and applying appropriate boundary conditions [8,9]. Their solution yields a wave which obeys the dispersion relation

$$k_x^2 + k_{z,i}^2 = \epsilon_i \left(\frac{\omega}{c}\right)^2 \tag{2.6}$$

where k_x and $k_{z,i}$ are components of the wave-vector along the respective axis, c is the speed of light in vacuum, ω the angular frequency and ϵ_i the dielectric constant. The subscript i in $k_{z,i}$ can stand for m (metal) or d (dielectric). The coordinates x and z are mutually

perpendicular and lie in a plane, and x is parallel to the interface. Since we deal with the interface where the metal is described by the complex dielectric constant $\epsilon_m = \epsilon'_m + i\epsilon''_m$, both k_x and k_z are complex functions and therefore represent waves which are attenuated along the respective directions. It can be shown [8, 9] that the surface plasmon wave can only exist if the condition

$$\epsilon'_m < -\epsilon_d \tag{2.7}$$

is satisfied. Furthermore, this wave is p-polarised, i.e. with electric vector lying in the x-z plane. If the condition (2.7) is satisfied equation (2.6) can be re-written in the form [8, 9]

$$k_x = \frac{\omega}{c}\left(\frac{\epsilon_m \epsilon_d}{\epsilon_m + \epsilon_d}\right)^{1/2} \tag{2.8}$$

Assuming that $\epsilon''_m < |\epsilon'_m|$ (which is satisfied for the most widely used silver and gold in the visible range), the complex propagation constant k_x can be written as $k_x = k'_x + ik''_x$, where

$$k'_x = \frac{\omega}{c}\left(\frac{\epsilon'_m \epsilon_d}{\epsilon'_m + \epsilon_d}\right)^{1/2} \tag{2.9}$$

and

$$k''_x = \frac{\omega}{c}\left(\frac{\epsilon'_m \epsilon_d}{\epsilon'_m + \epsilon_d}\right)^{3/2} \frac{\epsilon''_m}{2\epsilon'^2_m} \tag{2.10}$$

where ϵ_d is the dielectric constant of the dielectric.

Equation (2.9) defines the spatial period of the surface plasmon wave and expression (2.10) characterises the attenuation of the SP wave along its direction of propagation. This attenuation is characterised by propagation length L_x, which is defined as the distance in the direction of propagation at which the energy of the surface plasmon decreases by a factor $1/e$ and can be written as [8]

$$L_x = \frac{1}{2k''_x} \tag{2.11}$$

Since $\epsilon'_m + \epsilon_d < 0$ it can be shown [8] that the wave-vectors $k_{z,m}$ and $k_{z,d}$ are purely imaginary. The optical fields decay exponentially as $exp(-|k_{z,i}||z|)$ into both metal and dielectric. The penetration depth d_i of the field into each medium (distance where the field intensity decreases to $1/e$) is expressed as

$$d_i = 1/|k_{z,i}| \tag{2.12}$$

For instance, the penetration depths for gold/water interface for wavelength 635nm are $d_m \sim$30nm and $d_d \sim$250nm respectively.

2.2.2.2 Excitation of surface plasmons by light

The dispersion relation for a free photon propagating in a medium with ϵ_d is given by

$$k_{ph,d} = \frac{\omega}{c}\sqrt{\epsilon_d} \tag{2.13}$$

where $k_{ph,d}$ is always smaller than the wave-vector of surface plasmons at the dielectric/metal interface (k_x expressed by eq. (2.8)). This is shown graphically as the $\omega(k_x)$ plots in fig. 2.6, where line **a** represents the dispersion of the free photon. The dark gray marked area represents the frequency versus x component of the wave vector combinations that are accessible by light in the medium with ϵ_d. The $\omega(k_x)$ curve of SPs approaches asymptotically the dispersion curve of the free photon ($|\epsilon'_m| >> \epsilon_d$ for $\omega \rightarrow 0$) with no intersection of the curves. Thus, the SP cannot directly transform into light on a smooth surface, i.e., it is a non-radiative wave. Another consequence is that light cannot be used to excite SPs directly, due to its insufficient k_{ph}. It is therefore necessary to employ a supporting mechanism for excitation of SP on the metal-dielectric interface. Techniques such as prism coupling, grating coupling, waveguide coupling or coupling by means of a rough surface are used to enhance the lightwave momentum and thus excite surface plasmons by light.

Prism coupling is one of the most widely used coupling techniques for enhancing the wave--vector of the incident light. Photons are not coupled directly to the metal/dielectric interface, but via the evanescent tail of the light which is totally internally reflected at the base of a high-index prism (with the dielectric constant $\epsilon_p > \epsilon_d$). There are two different configurations for exciting surface plasmons by use of a high refractive index prism. In the Otto configuration [10], the evanescent field bridges a 200nm wide air gap between the prism and the metal and the plasmons are excited at the metal/air interface. In the predominantly used Kretschmann configuration [11], the light couples through a thin metal layer ($<$100nm for light in the visible spectrum), which is directly evaporated onto the base of the prism (or a substrate which is optically matched to the prism). This configuration will be considered in further text.

The propagation constant of the surface plasmon propagating along the metal-dielectric interface is influenced by the presence of the prism on the opposite side of the metal. This

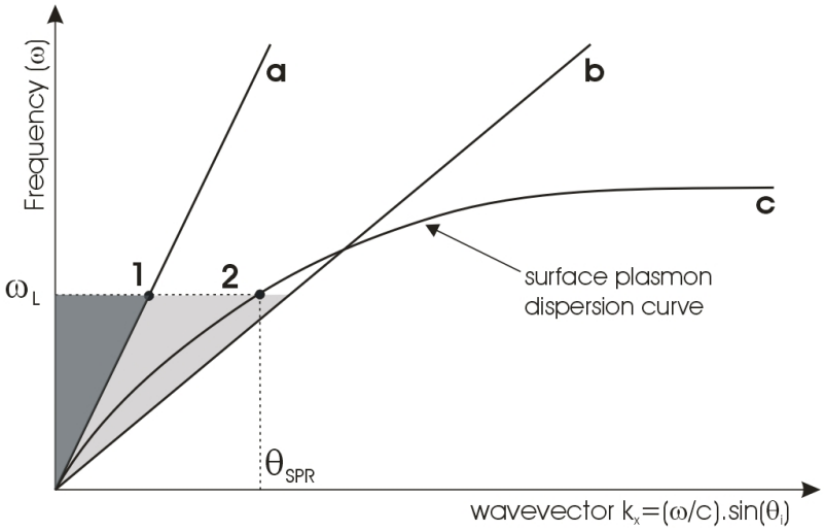

Figure 2.6: Dispersion relation of (a) free photons in a dielectric, (b) free photons propagating in a coupling prism, and (c) the dispersion relation of surface plasmons at the interface between the metal and the dielectric in the three-phase prism-metal--dielectric system. The intersection point **1** denotes the wave-vector magnitude corresponding to the laser light with frequency ω_L propagating in the medium with ϵ_d, the point **2** denotes the condition for coupling of incident light from the prism side to the surface plasmon

modified propagation constant $k_{SPR,x}$ can be written [9]

$$k_{SPR,x} = k_x + \Delta k_x \tag{2.14}$$

where k_x is the propagation constant of the surface plasmon propagating along the metal-dielectric interface in the absence of the prism (described by eq. (2.8)) and Δk_x accounts for the finite thickness of the metal and the presence of the prism.

The momentum of the light wave propagating in the prism changes to $k_{ph,p}$, and is equal to

$$k_{ph,p} = \frac{\omega}{c}\sqrt{\epsilon_p} \tag{2.15}$$

The slope of the corresponding dispersion curve is decreased, compared to the wave with wave-vector $k_{ph,d}$, and is shown as line **b** in fig. 2.6. The range of wave-vectors accessible from the prism side, denoted by the light-grey area, can be tuned by varying the angle of incidence or wavelength of the excitation light. For a laser with certain frequency ω_L the dispersion curve of the surface plasmon determines the laser incident angle θ for the excitation of the SP (the intersection point **2**). This occurs if the projection of the wave-vector $(\omega/c)\sqrt{\epsilon_p}$ on the x-axis matches the x-component of k_{SPR}. The coupling condition

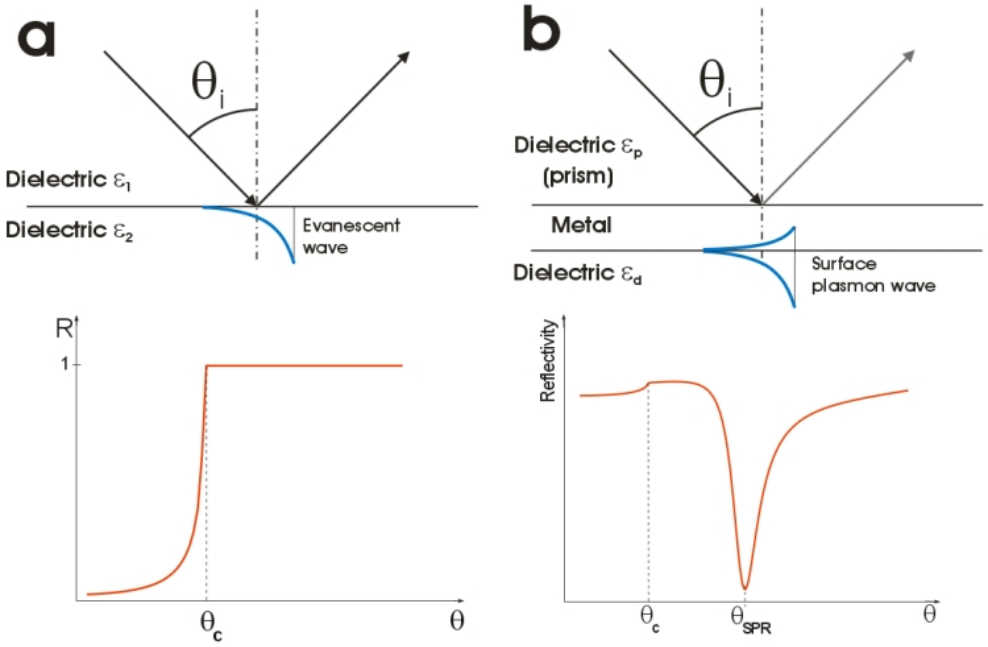

Figure 2.7: (a) Total internal reflection of a plane wave at the interface of 2 dielectrics, (b) excitation of surface plasmon at the interface of metal and dielectric ϵ_d in Kretschmann geometry

can be written as

$$\frac{\omega_L . \sin\theta_{SPR}}{c}\sqrt{\epsilon_p} = k_{SPR,x} \tag{2.16}$$

The existence of the coupling condition expressed by eq. (2.16) leads to a modification of the reflectivity on the dielectric-metal-dielectric interface as opposed to a simple dielectric-dielectric interfaces, which is illustrated in fig. 2.7. Unlike the dielectric-dielectric interface (fig. 2.7a), where the reflectivity is constant above the critical angle, the excitation of a surface plasmon is characterised by a sharp dip in the reflection curve (fig. 2.7b), which denotes resonant energy transfer from the incident wave to the surface plasmon. It can be shown [9] that the surface plasmon wave can only be excited with *p*-polarised incident wave.

Calculation of the reflection curves for a multilayer system is based on the Fresnel equations [8]. The position, depth and halfwidth of the reflectivity dip is dependent on the dielectric constants of the dielectric material and the supporting prism and thicknesses and dielectric constants of any additional intermediate layers [12]. The system is analogous to a damped oscillator (plasma wave) driven by an external force (incident light wave). A system in resonance is characterised by the value of reflectivity dropping almost to zero, which means that nearly all the incident light is coupled into the surface plasmon. For a three-phase glass-metal-water system, the maximum coupling efficiency (at λ=635nm) is achieved for

metal layer thicknesses around 50nm (for silver, and slightly lower for gold). The half-width of the reflection dip is mainly determined by the imaginary part of the metal dielectric constant [9].

2.2.2.3 Effect of a thin dielectric layer on the SPR spectrum

The evanescent field of a surface plasmon wave reaches its maximum strength directly at the metal-dielectric interface and decays exponentially into the dielectric medium at a distance of several hundreds of nanometers. Therefore the surface plasmon resonance technique is extremely sensitive to changes of the optical properties of the adjacent dielectric medium. This means that a variation of the ϵ_d in eq. (2.8) changes $k_{SPR,x}$ and consequently, changes the surface plasmon resonance angle defined by equation (2.16). The addition of

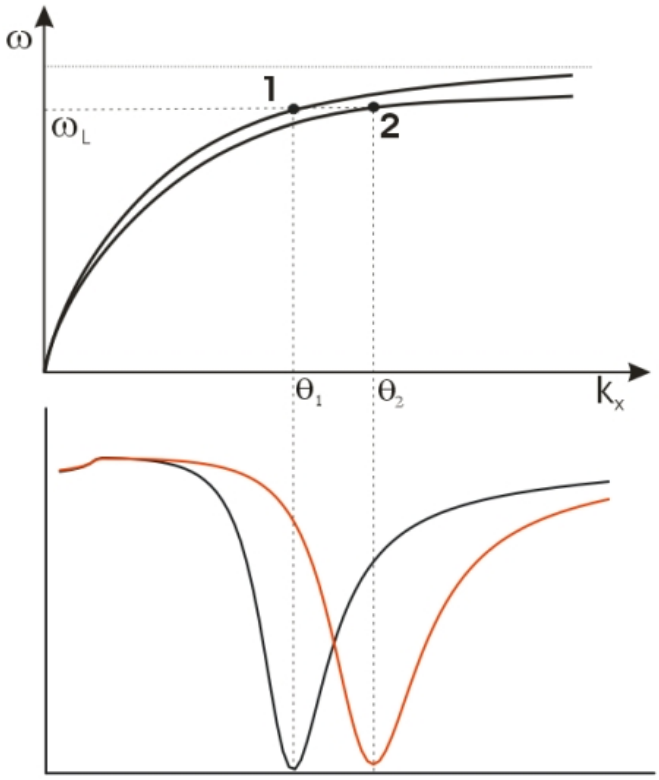

Figure 2.8: Shift of the SP dispersion curve when a thin dielectric film is added between the metal and dielectric. The intersection points **1** and **2** denote the coupling conditions without and with the presence of the thin film, respectively

a thin (with thickness d_f much smaller than the SP decay length along the z-axis) and non-absorbing layer with dielectric constant $\epsilon_f \neq \epsilon_d$ also induces a change in the overall dielectric constant integrated over the evanescent field, therefore shifts the SPR angle. The mean dielectric constant within the evanescent field increases assuming $\epsilon_f > \epsilon_d$. Therefore, the dispersion relation of eq. (2.8) shifts to a larger wave-vector. Consequently, a higher

light incident angle $\theta_2 > \theta_1$ is required to fulfill the resonance as illustrated in fig. 2.8. The rising thickness of the dielectric film also causes that the halfwidth of the reflection dip broadens. The broadening is a result of lower coupling efficiency into surface plasmon due to the presence of the additional layer with different value of refractive index.
For a thin, non-adsorbing layer defined by a thickness d and a refractive index n, the resonant angle displacement $\Delta\theta$ is linear with respect to the optical thickness $n \cdot d_f$ of the layer. If the film is sufficiently thick that it can form a waveguide, it is possible to observe reflection minima at multiple angles [13].

2.2.2.4 Field enhancement

Meeting the condition in eq. (2.16) means that the wave-vector of the incident light matches that of the surface plasmon wave supported by the metal. The resonant oscillations result in almost all of the energy of the incident radiation being converted into the surface plasmon wave and, thus, the electromagnetic field at the interface is greatly enhanced. The enhancement factor is expressed as a ratio of the field intensity at the metal-dielectric interface and the incident field intensity. For the three-phase (glass-metal-water/air) system the enhancement factors at the metal-water interface, calculated from [8], are $\sim$70 for silver and $\sim$28 for gold, and at the metal-air interface $\sim$120 for silver and $\sim$50 for gold. The factors were calculated for the optimum metal film thickness ($\sim$50nm) and wavelength 635nm and the dielectric constants of gold and silver were taken from [14]. The higher enhancement factor, obtainable for silver around λ=635nm, is mainly due to its more favourable value of ϵ'_m at this wavelength (since the enhancement factor is $\sim |\epsilon'_m|^2$ for a three-layer system [8]), and also its smaller imaginary part of the dielectric constant ϵ''_m, which results in lower dissipation of the optical field. The SP field is pushed more into the metal by the optically denser dielectric (water) compared to the air and, consequently, the field enhancement is lower in metal/water than in metal/air.

2.3 Molecular fluorescence near interfaces

The underlying principles of the interaction of molecular radiation with interfaces will be addressed in this section. Detailed description of the theoretical approach, used in this thesis, can be found in the publications of J. Enderlein. The mathematical model, used for calculations of the emission patterns and fluorescence intensities throughout the thesis, is based on this theory and was also developed by J. Enderlein.

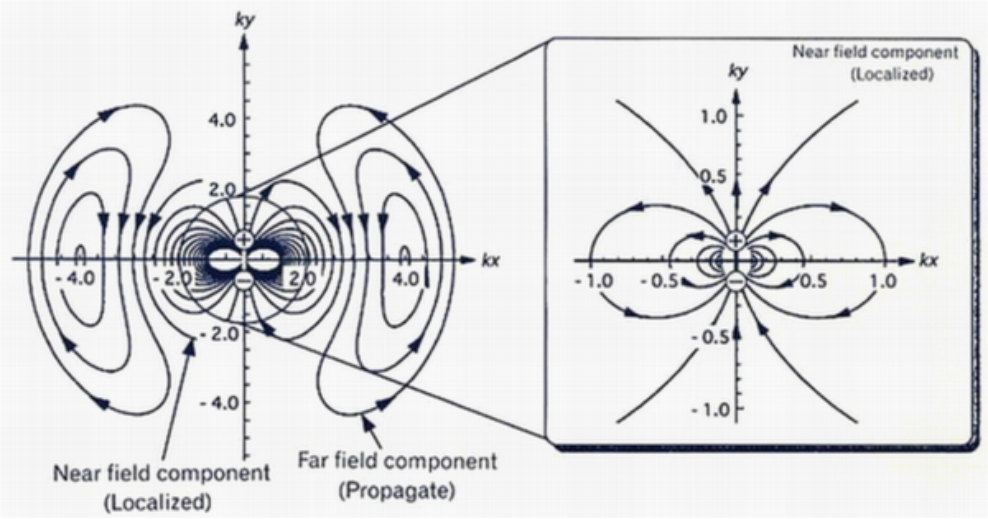

Figure 2.9: Electric field of the oscillating dipole. Image adopted from [16]

2.3.1 Description of a fluorophore as a dipole emitter

From the point of view of electromagnetism, a radiating molecule can be conveniently described as an oscillating point dipole with angular frequency ω and dipole momentum vector $\vec{p}$. The electric field pattern of a dipole located in a homogeneous medium can be derived by solving Maxwell's equations for a homogeneous medium with the oscillating dipole acting as a current source. Since we are interested in the solution in the form of plane waves, to express the spatial variation of the field, the harmonic, time-dependent factor can thus be omitted. The full derivation can be found in [15]. The resultant expression for the electric field vector $\vec{E}$ for the dipole located at the origin of the coordinate system can be written as

$$\vec{E}(\vec{r}) \approx \left[\left(-1 - \frac{3i}{kr} + \frac{3}{(kr)^2}\right)\vec{n}(\vec{n}\cdot\vec{p}) + \left(1 + \frac{i}{kr} - \frac{1}{(kr)^2}\right)\vec{p}\right]\frac{exp(ikr)}{kr} \tag{2.17}$$

where $\vec{r}$ is the position vector and $\vec{n}$ a unit vector along the direction of $\vec{r}$. Expression (2.17) consists of two major components. The propagative component, which is proportional to r^{-1}, contributes to the energy transport towards infinity. The components proportional to r^{-2} and r^{-3} describe the non-propagative (near) field, with range in the order of the emission wavelength λ. Schematically, the two field components are illustrated in fig. 2.9. It can be derived that the angular distribution of the far-field radiation of the free dipole follows a $\sin^2\theta$ dependence, where θ is the angle between the orientation of the dipole transition momentum vector $\vec{p}$ and the direction of observation. This also implies that no energy is emitted along the direction of the dipole axis.

2.3.2 Dipole emitter in the vicinity of an interface: theoretical description

When a radiating dipole is placed in close proximity to an interface the radiation pattern illustrated in fig. 2.9 is altered by the presence of the discontinuity of the refractive indices of the two macroscopic media. The two media are often divided by a microscopic layered structure. The angular distribution of fluorescence emission (ADE), fluorescence intensity and the modification of the fluorescence photodynamics due to the energy transfer are the quantities of interest.

Theoretical approaches to the solution of this problem have been addressed by a number of authors [17–26]. The solution, outlined below, is based on a semiclassical approach, where Fresnel equations for the layered structure are solved for each plane wave component of the dipole radiation. The problem is illustrated in fig. 2.10. The dipole, depicted

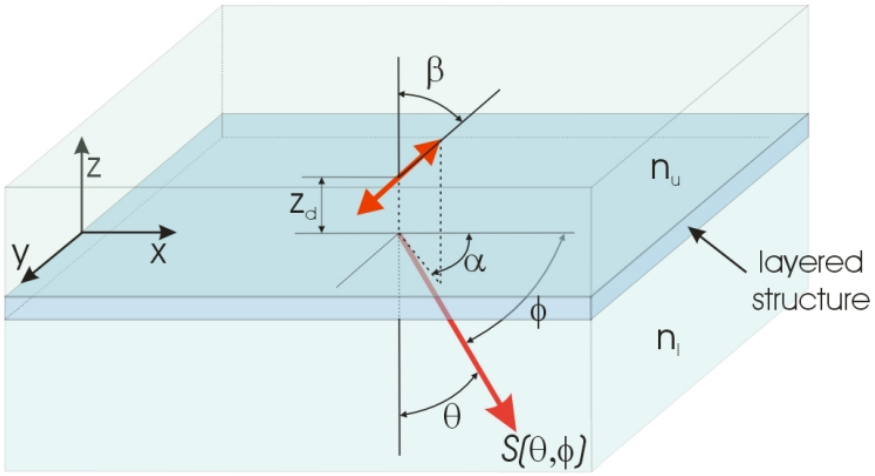

Figure 2.10: Sketch of a system with a dipole being placed close to the interface of two macroscopic media, separated by a multilayer structure

with the arrow and described by the dipole momentum vector $\vec{p}$, is placed in the upper (macroscopic) medium, characterised with refractive index n_u, at the distance z_d from the interface. The projection of the vector $\vec{p}$ into the three main axes is described by angles (α,β), where β denotes the inclination towards the z-axis and α around this axis. A layered (microscopic) planar structure divides the upper medium from the lower (macroscopic) medium, characterised with refractive index n_l. Both macroscopic media are assumed to be isotropic and homogeneous and with $n_l > n_u$. The layered structure comprises N layers, which are characterised by their (complex) refractive indices n_i and thicknesses d_i, where $i \in 1, \cdots, N$ (with regard to the studies presented in chapters 3 and 4 the

multilayer structure accommodates a metal or a metal-dielectric layer with well defined, ideal interfaces).

The calculation of the field magnitudes and hence angular distribution of the fluorescence emission intensity $S(\theta, \phi)$ can be summarised in three major steps. Full details of the calculation can be found in [15, 22–24].

1. The electric field of the dipole (eq. (2.17)) is re-written in integral form (Weyl identity), with the *s*- and *p*-polarised components of the plane waves expressed separately

2. Fresnel coefficients for the multilayer system are calculated for both the *s*- and *p*-polarisations, followed by tracing each plane wave component in the integral through the layered structure

3. Magnitudes of the field intensities emitted into both upper and lower media are calculated with respect to the total emission power of the dipole; this includes calculation of non-radiative losses due to absorption, quenching etc.

The emission into the substrate at angles (θ, ϕ) will be of interest further. In the general form, the dependence of the ADE can be written as [27, 28]

$$\begin{aligned} S(\theta, \phi, \alpha, \beta, z_d, n_i, d_i, n_u, n_l, \lambda) \approx & \\ \approx \quad & S^{\perp}(\theta, z_d, n_i, d_i, n_u, n_l, \lambda) \cos^2 \beta \\ + \quad & S^{\parallel,c}(\theta, z_d, n_i, d_i, n_u, n_l, \lambda) \sin^2 \beta \cos^2(\phi - \alpha) \\ + \quad & S^{\parallel,s}(\theta, z_d, n_i, d_i, n_u, n_l, \lambda) \sin^2 \beta \sin^2(\phi - \alpha) \end{aligned} \tag{2.18}$$

The emission intensity into the given angle (θ, ϕ) described by eq. (2.18) is expressed as a sum of three terms, where each term denotes the contribution from the projections of the vector $\vec{p}$ along the coordinate axes. The first term on the right hand side of eq. (2.18) is proportional to the projection into *z*-axis, and the next two into *x*- and *y*-axis, respectively. The coefficients $S^{\perp}$, $S^{\parallel,c}$ and $S^{\parallel,s}$ are functions of the system parameters and the emission angle θ (but not ϕ due to the cylindrical symmetry of the emission pattern).

Calculation of the field intensities also shows [15] that the near-field component of the radiation, not contributing to the far field in the homogeneous medium, modifies the far-field emission pattern when placed near the interface. This can be explained by the creation of new decay channels through which energy can dissipate (in both a radiative and non--radiative way). This has two consequences. First, a higher proportion of light is emitted into the medium with higher refractive index (the lower medium, called substrate) and is

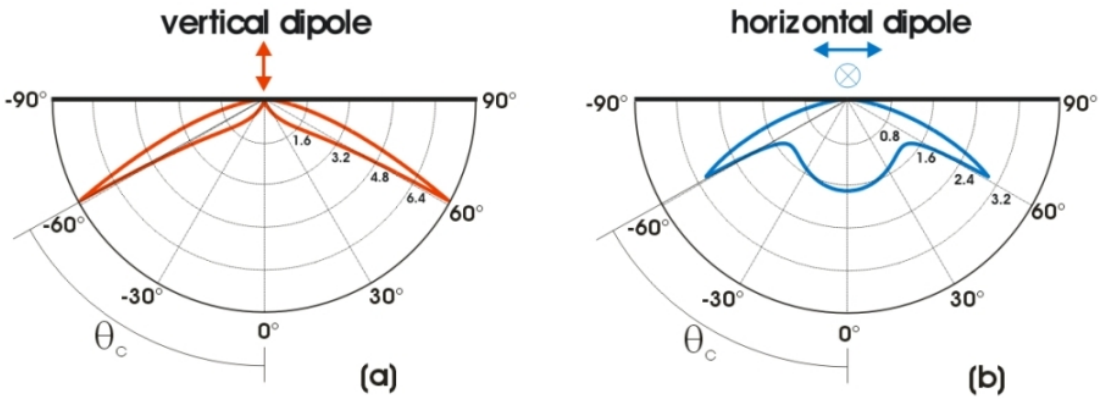

Figure 2.11: Far-field intensity profiles of fluorescence emerging from dipole emitters placed on a water/glass interface, expressed as a function of angle θ ($\phi = 0°$). (a) Dipole oriented perpendicularly to the interface ($\beta = 0°$) and (b) dipole oriented parallel to the interface ($\beta = 90°$), expressed as the sum of 2 components ($\alpha = 0°$ and $\alpha = 90°$), where each component contributes by one half. The strength of each dipole is assumed to be equal. The critical angle θ_c of the water/glass interface is 61°

proportional to the ratio of the refractive indices values n_u and n_l. Second, emission into the substrate is highly anisotropic, and a large proportion occurs above the critical angle of the interface, where $\theta_c = \sin^{-1}(n_u/n_l)$. The presence of the discontinuity has also an impact on the fluorescence emission dynamics [20, 29].

2.3.3 Interface of two dielectrics: emission anisotropy

The emission anisotropy is illustrated for the most simple case, where the fluorescent molecule is placed at the interface of water (*n=1.33*) and glass (*n=1.52*) and the distance $z_d = 0$. The emission patterns for molecules with both vertically and horizontally oriented transition moments are illustrated in fig. 2.11.

For the surface-bound fluorophores, maximum light intensity is emitted into the critical angle of the interface, but the contribution to the supercritical fluorescence intensity (SAF) is significantly higher for the vertically oriented molecules than for the horizontal ones, where much of the power is emitted below the critical angle. The peak intensity is also higher for the vertical dipole for which the coupling is more efficient. With increasing distance of the molecule from the interface the near-field coupling becomes weaker and leads to a reduction of the supercritical angle fluorescence intensity. As reported in [30] the distance of a molecule from the water-glass interface at which the SAF intensity is reduced by 1/e is about $\lambda/6$, where λ is the wavelength of fluorescence emission.

In the real bio- and chemoanalytical applications the dipole moments of surface-bound

molecules are rather randomly oriented, meaning that each orientation contributes equally to the resultant emission field. Here, about 34% of the total fluorescence emission intensity is emitted above the critical angle.

2.4 Surface plasmon-coupled emission

Surface plasmon-coupled emission (SPCE) is a result of the near-field interaction of a radiating molecule with a layered structure containing a thin metal film. The plasmon-mediated emission was first reported by Benner [31], when he observed sharp emission peaks in the glass prism originating from the molecules near the metal film, when excited by a surface-plasmon field. Recently, SPCE has been subject of numerous theoretical [27, 32, 33] and experimental [28, 34–36] studies.

2.4.1 Fluorophore near a metal film

As described in section 2.3.2, placing a fluorescent molecule in close proximity to an interface leads to the modification of its emission profile and dynamics. As compared to a simple dielectric interface, metal induces new decay channels through which energy can dissipate. The strength of the various decay channels depends on metal-fluorophore separation, local conditions and orientation of the molecule.

Considering the system depicted in fig. 2.10, the fluorophore is placed in the medium with lower refractive index, separated from the higher-index medium by a thin metal film. A plasmon at the metal-upper dielectric interface would not be excited by a simple plane wave due to momentum mismatch (fig. 2.6), but some plane-wave components of the molecular radiation which have sufficient momentum can couple into the surface plasmon at the upper interface. These plasmons can be re-radiated into the lower medium (with higher refractive index) in a narrow range of angles around the SPR angle corresponding to the fluorophore emission wavelength [37].

2.4.2 Effect of metal-fluorophore separation

Three different decay regimes for fluorescence near the metal film may be considered as schematically presented in fig. 2.12. It should be noted that the described decay mechanisms are generic , but vary quantitatively depending on the local environment and orientation of molecules.

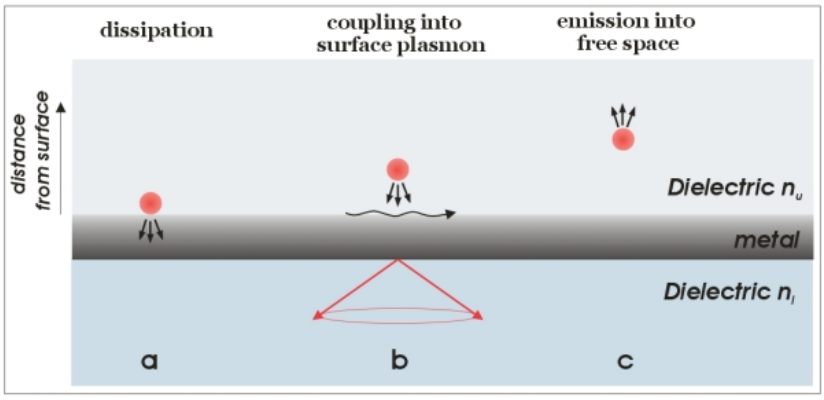

Figure 2.12: Illustration of the three main regimes of interaction of an excited fluorophore surrounded by a dielectric at different distances z_d from metallic film. The refractive indices of the dielectrics are same as in fig. 2.10. (a) For the molecules in a close vicinity to the metal the fluorescence radiation energy is drawn by the metal and predominantly dissipated in a non-radiative way. (b) By increasing the distance, the near-field of fluorophore radiation excites surface plasmon oscillations. The plasmons can out-couple into propagating modes in the glass substrate in a form of hollow cone. (c) Farther away from the metal, coupling into SP is weakening, and normal de-excitation unaffected by the presence of metal dominates. Fluorescence is mainly emitted into the superstrate

Non-radiative transitions and exciton coupling

Very close to the metal surface, up to 10nm from the surface, electron-hole pairs (excitons) can be excited by the near field of the dipole and thus the interaction is of dipole-dipole nature. For very small metal-dye distances d the dipole field is dominated by the near field the strength of which decreases with r^{-3} (eq. (2.17)). The classical Förster model for the interaction between two individual dipoles involves the distance dependence of both acceptor and donor and thus results in a d^{-6} dependence [15]. However, integrating over all possible sites of an entire surface of acceptors will yield a d^{-4} dependence. A d^{-3} dependence is obtained if the excitation of excitons in the bulk of the substrate is considered. When the interaction with excitons on the surface of the sample is considered, the distance-dependent interaction will be in the d^{-4} [38]. Although very close distances lead to significant shortening of the lifetime and thus increased quantum efficiency of the fluorophore [27], the fluorescence is lost in the metal in a non-radiative way (by quenching).

Coupling to surface plasmon modes

At an intermediate distance from the surface, a radiating dipole can excite surface plasmon modes at the upper metal-dielectric interface. This again can couple to light and can be observed in the lower environment in the form of a hollow cone of emission. The angular

distribution of this plasmon coupled fluorescence emission is determined by the fluorophore emission spectrum and the surface plasmon dispersion [39]. The range of coupling distances (typically tens of nanometers for glass/metal/water or glass/metal/air systems) is dependent on the dielectric constants of the materials, and, generally, vertically oriented dipoles couple into the surface plasmons more efficiently than the horizontal ones [27].

Free space emission

For even larger metal-dye distances (exceeding those for coupling into surface plasmons), free emission of photons in the bulk is dominant over the other modes of excitation discussed above. The emission rates are not affected by the interface and are (almost) the same as for free molecules. Since the metal film behaves as a mirror for the fluorescence, the resultant field pattern is determined by the interference effects of the radiated and reflected fluorescence.

Unlike the SPCE intensity variations, dependent on the metal-fluorophore distance as discussed above, the SPCE angle remains constant as long as the changes of the metal--fluorophore distance occur within a homogeneous medium. If the separation distance is realised by means of a dielectric spacer layer (which is assumed to have higher refractive index than the surrounding medium), the SPCE angle changes according to the conditions expressed by equations (2.8) and (2.16). If the spacer thickness is large enough that it can form a waveguide layer, multiple emission peaks can be observed. Emission into multiple angles is also valid when the fluorophores are entrapped in a sufficiently thick dielectric layer [36, 40].

2.4.3 SPCE observation: practical considerations

Since SPCE is the 'reverse' effect to SPR, the same metals (mainly gold and silver for applications in the visible and near infrared spectrum) are used. The optimum silver or gold film thickness is also 50nm [41]. SPCE was also observed with other metals. The use of an aluminium film was reported in the ultraviolet range [42], a zinc film in ultraviolet and visible range [43], and a platinum film in the visible range [44].

As a consequence of the strong dependence of the dielectric constants of metals on wavelength, the plasmon-coupled fluorescence originating from fluorophores emitting at different wavelengths is observed at different angles. This effect may be useful e.g. for multianalyte detection [45]. It is, however, important to properly consider the metal type and the

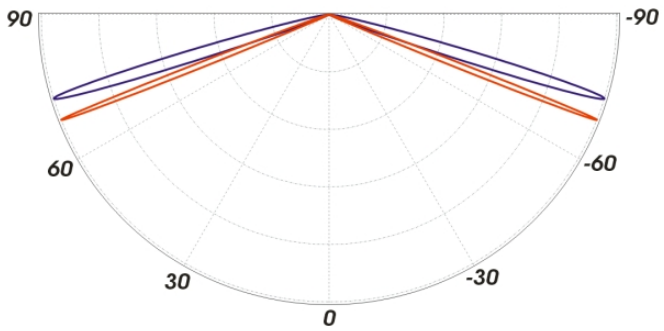

Figure 2.13: Angular separation of the plasmon-coupled peaks originating from Cy5 (blue line) and Cy7 (red line) emission. The angular profiles are calculated for glass-water interface and 50nm thick gold film

emission wavelengths of thr fluorophores used so that sufficient angular separation can be achieved. Fig. 2.13 shows the calculated angular emission profile of plasmon-coupled emission for Cy5 (peak emission at 670nm) and Cy7 dyes (peak emission at 770nm), supported by a 50nm gold film. The curves were calculated using the model described earlier.

Since SPCE is the result of fluorescence radiation coupling into surface plasmon modes, its observation is not dependent on the way the fluorophores are excited. The two possible methods are showed in fig. 2.14. With direct illumination (also denoted as reverse Kretschmann [34]), a direct light beam excites the fluorophores, and fluorescence from those within the plasmon-coupling distance from the metal film can be observed as SPCE. Since the metal film serves as a mirror, the incident light is reflected, so the intensity of

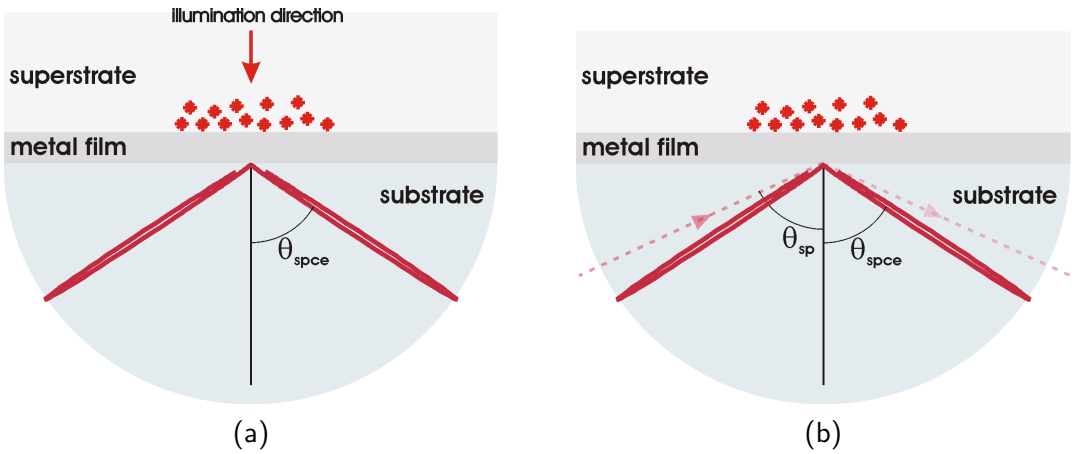

(a) (b)

Figure 2.14: Excitation geometries for observation of SPCE. (a) excitation by direct illumination and (b) excitation by surface plasmon generated at the metal-superstrate interface

the fluorophore excitation field is a result of the interference of the incident and reflected beam. Whether it is minimised or maximised, will depend on the wavelength and direction of the incident beam and the distance of the molecule from the metal film. As illustrated

in fig. 2.6, due to the mismatch of the wavevectors, a surface plasmon can not be excited by the incident light. Primarily horizontally-oriented dipoles are excited with the direct illumination.

Excitation via an SPR wave generated at the interface provides enhanced field intensity in the vicinity of the interface and primarily targets vertically-oriented dipoles, which couple more strongly into SPCE. However the fluorophores will not be excited with the maximum field enhancement factor since this can only be achieved directly at the interface, where the fluorescence is quenched. The spatial confinement of the SP field also suggests that it is more suitable for surface-selective illumination. On the other hand, a comparison between the spatial extent of the SP field (several hundred nm) and the fluorescence coupling distance (tens of nm) suggests that it is the fluoresence coupling distance rather than the spatial extent of the SP wave which is the determining factor for the fluorescence detection distance in the SPR-SPCE scheme.

2.5 Immunoassays: basic principles

The principles of immunoassay-based biosensing are briefly explained in the context of this work. A more thorough overview can be found in [46].

An immunoassay is a biochemical test that measures the concentration of a substance in a biological liquid (typically blood serum or urine), using the binding reaction of an antibody (abbreviated Ab hereafter) to an antigen (abbreviated Ag), taking advantage of the specific binding of an antibody to its antigen. Antibodies are a product of an immunoreaction of the living organism to the presence of a pathogen. They are produced by a maturation of so called B-lymphocyte cells into antibody producing plasma cells. The presence of a pathogen triggers the production of antibodies which possess a specific antigen binding fragment.

A simplified structure of an antibody with an illustration of the variable binding fragment is shown in fig. 2.15.

The Ab-Ag binding process is governed by the affinity of the antigen to its antibody and in general terms is a measure of how quickly and strongly the Ab-Ag pair is

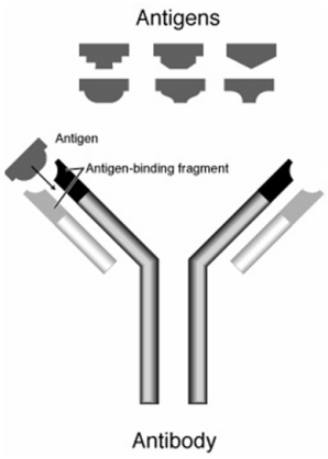

Figure 2.15: Simplified structure of an antibody with a variable Ag binding fragment

formed. There are a number of factors that affect the affinity such as pH, temperature and ionic strength and they need to be controlled in order to optimise the binding process. It is desirable for the immunoassay technology to use antibodies with the highest affinity possible to the detected antigen. Usually the higher is the affinity the more accurate the measurement is and hence lower concentrations can be detected.

The majority of immunoassays can be categorised as either label-free or labelled. In the label-free assay formats, the concentration of the detected substance expressed by number of Ab-Ag conjugates is usually measured indirectly. In the best known example of label-free assays, based on surface plasmon resonance [9], local changes in refractive index is the determining factor. In label-based immunoassays, where one of the constituents is labelled with a tag (radioisotope, enzyme, fluorophore, etc.) the number of observed binding events is proportional to the measured intensity of the signal produced by the labels. The use of fluorescence tags offers a number of advantages over other types such as biocompatibility, availability in a wide range of wavelengths, ease of conjugation to proteins etc. Hereafter, fluorescence-based assays will be the focus.

The assay formats can be divided into two major categories: non-competitive and competitive. The non-competitive category encompasses direct and sandwich assays (fig. 2.16). The direct binding assay (fig. 2.16a) is the simplest to perform. Antibodies specific to the

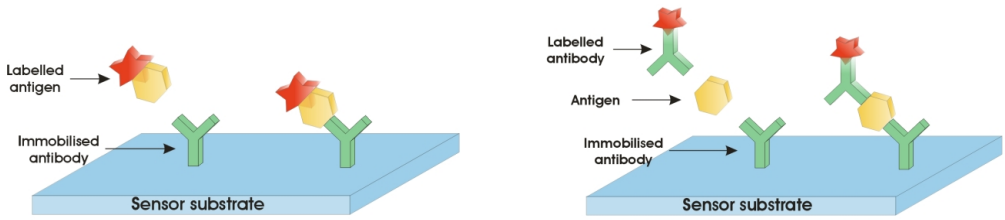

(a) (b)

Figure 2.16: Schematic of non-competitive assay formats: (a) direct and (b) sandwich

antigen of interest are immobilised onto the sensor surface, and the antigens are introduced to bind to the antibodies. This assay can also be performed by immobilising antigens on the sensor surface and allowing antibodies to bind to them. The sandwich assay format (fig. 2.16b) also involves the immobilisation of antibodies, followed by the attachment of antigens but in this case the presence of the antigen is detected by a second, labelled antibody. For sandwich assays to be effective, the antigen of interest must be large enough with sufficient epitopes to bind two antibodies simultaneously. A major advantage of the sandwich format is a reduction of the number of false detections as the detected antigen needs to bind to two antibodies. These two assay formats were pursued in this work.

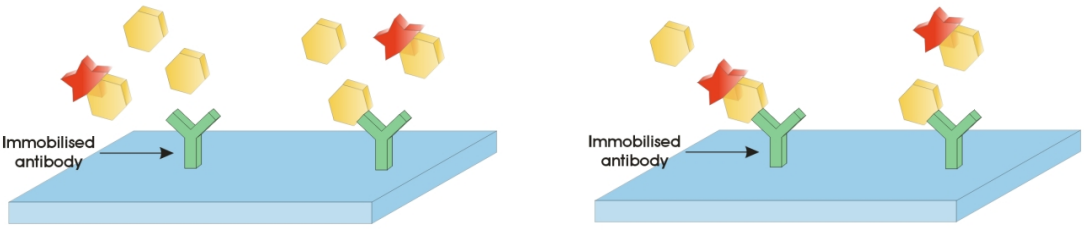

(a) (b)

Figure 2.17: Schematic of (a) competitive and (b) displacement assay formats

In a competitive assay (fig. 2.17a) a known quantity of labelled Ag is introduced along with a test sample containing the unknown amount of Ag which compete for binding sites with antibodies immobilised onto the sensor surface. Finally, in a displacement assay (fig. 2.17b) immobilised antibodies are saturated by labelled antigens and a portion of unlabelled antigens from the test sample displaces the bound labelled ones. Competitive or displacement assays are capable of detection of small molecules.

For quantitative results, for any assay format the response of the fluid being measured must be compared to standards of a known concentration. This is usually done by plotting a standard (or calibration) curve. The position of the curve at the response of the unknown sample is then examined, and so the quantity of the unknown analyte is found. For the direct and sandwich formats, the standard curve increases with rising analyte concentration and decreases for competitive and displacement formats, as is illustrated in fig 2.18.

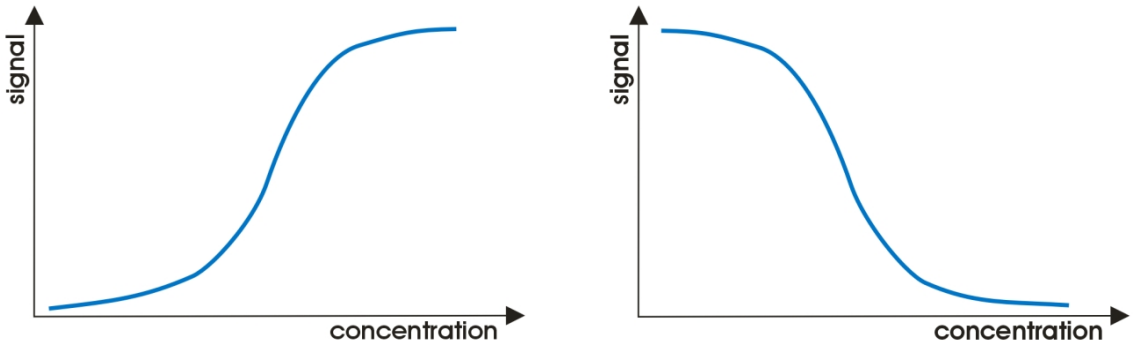

(a) (b)

Figure 2.18: Trend of the standard curve in (a) non-competitive and (b) competitive assay formats

In real measurement conditions analyte molecules float in the entire volume of the fluid delivery system as illustrated on fig. 2.19. Only those within a short distance of the surface--immobilised capture antibodies are bound. Some of these are also non-specifically bound to the sensor surface and contribute to a false positive reading when a labelled counterpart is bound to them. It is therefore necessary to employ mechanisms to minimise non-specific

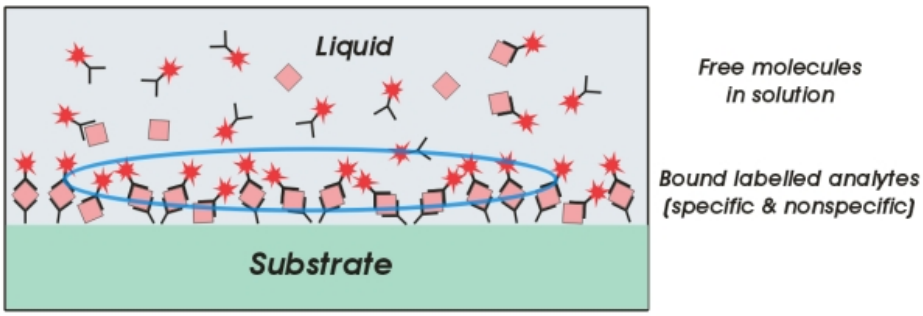

Figure 2.19: Illustration of real measurement conditions in a fluorescence-based immunoassay. The detection volume of interest is highlighted with the blue line, and, depending on the type of biomolecules and assay format, stretches from several nanometers to a few tens of nanometers into the upper, aqueous medium

binding. It is also desirable to only detect binding events between surface-bound receptors and analyte molecules and not any fluorescence events from the bulk of the fluid delivery system. A stretch of the detection volume, shown in fig. 2.19 and highlighted with the blue circle, should therefore be in the order of dimensions of the biomolecules (typically nanometers to a few tens of nanometers).

2.6 Conclusion

This chapter has provided a description of the underlying principles and theoretical aspects of the work being investigated in this thesis. Firstly, molecular fluorescence and principles of its enhancement were described. This was followed by a description of the surface plasmon resonance effect on a planar surface and the major properties of surface plasmons were outlined. It was shown that a radiating molecule can be treated as a dipolar emitter and this approach enables the prediction of the emission characteristics when a molecule is placed in the proximity of a layered structure. Surface plasmon-coupled emission was introduced. Finally, the basic concepts of immunoassays were described.

References

[1] J. R. Lakowicz. *Principles of fluorescence spectroscopy*. Plenum Press, New York, 1st edition, 1983.

[2] J. E. Berlier, A. Rothe, G. Buller, J. Bradford, D. R. Gray, B. J. Filanoski, W. G. Telford, S. Yue, J. X. Liu, C. Y. Cheung, W. Chang, J. D. Hirsch, J. M. Beechem, and R. P. Haugland. Quantitative comparison of long-wavelength alexa fluor dyes to cy dyes: Fluorescence of the dyes and their bioconjugates. *Journal of Histochemistry and Cytochemistry*, 51(12):1699–1712, 2003.

[3] O. Stranik. *Plasmonic enhancement of fluorescence for biomedical diagnostics*. Phd. thesis, DCU Dublin, 2007.

[4] J. R. Lakowicz, K. Ray, M. Chowdhury, H. Szmacinski, Y. Fu, J. Zhang, and K. Nowaczyk. Plasmon-controlled fluorescence: a new paradigm in fluorescence spectroscopy. *Analyst*, 133(10):1308–1346, 2008.

[5] T. Neumann, M. L. Johansson, D. Kambhampati, and W. Knoll. Surface-plasmon fluorescence spectroscopy. *Advanced Functional Materials*, 12(9):575–586, 2002.

[6] K. Vasilev, F. D. Stefani, V. Jacobsen, W. Knoll, and M. Kreiter. Reduced photobleaching of chromophores close to a metal surface. *Journal of Chemical Physics*, 120(14):6701–6704, 2004.

[7] http://www.olympusmicro.com/primer/java/index.html.

[8] R.H. Raether. *Surface plasmons on smooth and rough surfaces and on gratings*. Springer-Verlag, Berlin, 1988.

[9] J. Homola. *Surface Plasmon Resonance Based Sensors*, volume 4 of *Springer Series on Chemical Sensors and Biosensors*. Springer, Heidelberg, 2006.

[10] A. Otto. Excitation of nonradiative surface plasma waves in silver by method of frustrated total reflection. *Zeitschrift Fur Physik*, 216(4):398–410, 1968.

[11] E. Kretschmann and H. Raether. Radiative decay of non radiative surface plasmons excited by light. *Zeitschrift Fur Naturforschung Part a-Astrophysik Physik Und Physikalische Chemie*, A 23(12):2135–2136, 1968.

[12] D. Roy. Surface plasmon resonance spectroscopy of dielectric coated gold and silver films on supporting metal layers: Reflectivity formulas in the kretschmann formalism. *Applied Spectroscopy*, 55(8):1046–1052, 2001.

[13] S. Herminghaus and P. Leiderer. Improved attenuated total reflectance technique for the investigation of dielectric surfaces. *Applied Physics Letters*, 54(2):99–101, 1989.

[14] E. D. Palik. *Handbook of Optical Constants of Solids*. Academic Press, 3rd edition edition, 1998.

[15] J. Enderlein. Electrodynamics of fluorescence. Technical report, 2003.

[16] http://dept.physics.upenn.edu/courses/gladney/phys151/lectures/lecture_apr_07_2003.shtml.

[17] W. Lukosz and R. E. Kunz. Light-emission by magnetic and electric dipoles close to a plane interface .1. total radiated power. *Journal of the Optical Society of America*, 67(12):1607–1615, 1977.

[18] W. Lukosz. Light-emission by magnetic and electric dipoles close to a plane dielectric interface .3. radiation-patterns of dipoles with arbitrary orientation. *Journal of the Optical Society of America*, 69(11):1495–1503, 1979.

[19] W. Lukosz. Light-emission by multipole sources in thin-layers .1. radiation-patterns of electric and magnetic dipoles. *Journal of the Optical Society of America*, 71(6):744–754, 1981.

[20] R. R. Chance, A. Prock, and R. Silbey. Molecular fluorescence and energy transfer near interfaces. *Advanced Chemical Physics*, 60:1–65, 1978.

[21] E. H. Hellen and D. Axelrod. Fluorescence emission at dielectric and metal-film interfaces. *JOSA B - Optical Physics*, 4(3):337–350, 1987.

[22] J. Enderlein. Single-molecule fluorescence near a metal layer. *Chemical Physics*, 247(1):1–9, 1999.

[23] J. Enderlein. Fluorescence detection of single molecules near a solution/glass interface - an electrodynamic analysis. *Chemical Physics Letters*, 308(3-4):263–266, 1999.

[24] J. Enderlein, T. Ruckstuhl, and S. Seeger. Highly efficient optical detection of surface-generated fluorescence. *Applied Optics*, 38(4):724–732, 1999.

[25] J. Enderlein. A theoretical investigation of single-molecule fluorescence detection on thin metallic layers. *Biophysical Journal*, 78(4):2151–2158, 2000.

[26] L. Polerecky, J. Hamrle, and B.D. MacCraith. Theory of the radiation of dipoles placed within a multilayer system. *Applied Optics*, 39(22):3968–3977, 2000.

[27] J. Enderlein and T. Ruckstuhl. The efficiency of surface-plasmon coupled emission for sensitive fluorescence detection. *Optics Express*, 13(22):8855–8865, 2005.

[28] M. Trnavsky, J. Enderlein, T. Ruckstuhl, C. McDonagh, and B. D. MacCraith. Experimental and theoretical evaluation of surface plasmon-coupled emission for sensitive fluorescence detection. *Journal of Biomedical Optics*, 13(5), 2008.

[29] K.H. Drexhage. Influence of a dielectric interface on fluorescence decay time. *Journal of Luminescence*, 1-2:693–701, 1970.

[30] T. Ruckstuhl, J. Enderlein, S. Jung, and S. Seeger. Forbidden light detection from single molecules. *Analytical Chemistry*, 72(9):2117–2123, 2000.

[31] R. E. Benner, R. Dornhaus, and R. K. Chang. Angular emission profiles of dye molecules excited by surface-plasmon waves at a metal-surface. *Optics Communications*, 30(2):145–149, 1979.

[32] N. Calander. Theory and simulation of surface plasmon-coupled directional emission from fluorophores at planar structures. *Analytical Chemistry*, 76(8):2168–2173, 2004.

[33] N. Calander. Surface plasmon-coupled emission and fabry-perot resonance in the sample layer: A theoretical approach. *J. Phys. Chem. B*, 109(29):13957–13963, 2005.

[34] J. R. Lakowicz. Radiative decay engineering 3. surface plasmon-coupled directional emission. *Analytical Biochemistry*, 324(2):153–169, 2004.

[35] I. Gryczynski, J. Malicka, Z. Gryczynski, and J. R. Lakowicz. Radiative decay engineering 4. experimental studies of surface plasmon-coupled directional emission. *Analytical Biochemistry*, 324(2):170–182, 2004.

[36] I. Gryczynski, J. Malicka, K. Nowaczyk, Z. Gryczynski, and J. R. Lakowicz. Effects of sample thickness on the optical properties of surface plasmon-coupled emission. *Journal of Physical Chemistry B*, 108(32):12073–12083, 2004.

[37] W. H. Weber and C. F. Eagen. Energy-transfer from an excited dye molecule to the surface-plasmons of an adjacent metal. *Optics Letters*, 4(8):236–238, 1979.

[38] T. Liebermann and W. Knoll. Surface-plasmon field-enhanced fluorescence spectroscopy. *Colloids and Surfaces A-Physicochemical and Engineering Aspects*, 171(1-3):115–130, 2000.

[39] W. L. Barnes. Fluorescence near interfaces: The role of photonic mode density. *Journal of Modern Optics*, 45(4):661–699, 1998.

[40] I. Gryczynski, J. Malicka, K. Nowaczyk, Z. Gryczynski, and J. R. Lakowicz. Waveguide-modulated surface plasmon-coupled emission of nile blue in poly(vinyl alcohol) thin films. *Thin Solid Films*, 510(1-2):15–20, 2006.

[41] G. Winter and W. L. Barnes. Emission of light through thin silver films via near-field coupling to surface plasmon polaritons. *Applied Physics Letters*, 88(5), 2006.

[42] I. Gryczynski, J. Malicka, Z. Gryczynski, K. Nowaczyk, and J. R. Lakowicz. Ultraviolet surface plasmon-coupled emission using thin aluminum films. *Analytical Chemistry*, 76(14):4076–4081, 2004.

[43] K. Aslan, M. J. R. Previte, Y. X. Zhang, and C. D. Geddes. Surface plasmon coupled fluorescence in the ultraviolet and visible spectral regions using zinc thin films. *Analytical Chemistry*, 80(19):7304–7312, 2008.

[44] K. Ray, M. H. Chowdhury, and J. R. Lakowicz. Observation of surface plasmon-coupled emission using thin platinum films. *Chemical Physics Letters*, 465(1-3):92–95, 2008.

[45] E. Matveeva, J. Malicka, I. Gryczynski, Z. Gryczynski, and J. R. Lakowicz. Multi-wavelength immunoassays using surface plasmon-coupled emission. *Biophys. Biochem. Res. Comm.*, 313(3):721–726, 2004.

[46] H. McEvoy. *Development and Optimisation of Patterned Optical Immunosensors*. Phd. thesis, DCU Dublin, 2005.

Chapter 3

SPCE on a planar surface

3.1 Introduction and motivation

As discussed in chapter 1, fluorescence-based detection, due to its high sensitivity, is the technique of choice for detecting low concentrations of biomolecules in optical bioassays. Techniques such as TIRF [1], SAF [2] and SPCE [3, 4] have been used to provide the additional benefits of background discrimination due to their inherent surface selectivity. As discussed earlier, SPCE is also characterised by highly directional emission. Some authors have reported enhancements of $\sim$1000 for SPCE-based fluorescence detection [5] and studies have been published regarding the dependence of fluorescence intensity on distance from the metal film [6–8]. However, no direct comparison has been carried out between the performance of SPCE-based systems and similar systems without a metal film. A theoretical study was published by Enderlein [9] which concludes that SPCE does not produce any increase in intensity compared to that detected in the absence of the metal film. In fact, the model predicts that the presence of the metal film leads to a reduction in the detected fluorescence intensity.

This study is aimed at the experimental corroboration of the conclusions obtained from the theoretical model, developed by Jörg Enderlein (now with Georg August University, Göttingen, Germany) as a part of project collaboration. The experimental system employs a commonly used biological label, Cy5, which is separated from a thin silver film by silica spacer layers of varying thickness. The angular distribution of the SPCE intensity was investigated as a function of spacer layer thickness. Direct comparison of the total SPCE intensity and that measured in the absence of the metal layer was facilitated by using samples coated half with silver film and half without. A theoretical analysis of the system

was carried out , and the predictions were compared with experimental results. The key significance of this study is that it is the first experimental verification of the attenuation in SPCE intensity compared to that detected in the absence of the metal layer as predicted by Enderlein [9]. The experimental validation of the numerical model also provides a tool for optimisation of the layered structure and illumination.

3.2 Description of the experiment

This section describes the methods used for preparation and characterisation of samples for the fluorescence measurements. The experimental methodology for the detection of fluorescence is also described in detail.

3.2.1 Sample preparation

3.2.1.1 Cleaning and vacuum coating

Standard microscope glass slides (Menzel Gläser) were used throughout. They were cut to 1.5×2.5cm to fit the face of the hemicylindrical prism. First, the visible debris was removed mechanically by wiping. Then, slides were cleaned by sonicating in a mixture of ethanol and deionised water (mixture ratio 2:1) for 30 minutes, rinsed with deionised water and dried in a nitrogen stream. Subsequently, the clean slides were chemically treated by immersion in 1:3 30%-solution H_2O_2 and 98%-solution H_2SO_4 (Piranha solution) for at least 3 hours at room temperature, followed by thorough rinsing in deionised water and final drying with a nitrogen stream. By performing this step the surface will be free of any (hydrocarbon) contaminants and will be chemically homogenous with a high density of silanol (Si-OH) groups. Such slides were used immediately, without storage.

It is well known that the adhesion of thin films of noble metals formed by physical vapor deposition directly onto glass substrates is very poor. Ultimate cleanliness and preheating of the substrate and optimum choice of the deposition parameters as well as post-deposition treatment can improve the overall quality of the deposited layer. Application of a very thin film of a metallic adhesion promoter (Cr, Ti, Ni) or a thiol-terminated organosilane linker such as 3-mercaptopropyl trimethoxysilane (MPTMS) [10] or methods such as ion beam--assisted deposition [11, 12] may yield vapour-coated metallic films with good to excellent adhesion to the glass substrate. The intermediate metallic films (Cr, Ti) are widely used in surface plasmon resonance applications however they lead to an alteration of the dielectric constants of the system and an overall loss of signal due to their high absorption.

The method using MPTMS as a molecular adhesive was employed to promote the adhesion of the metallic films to the glass substrates. MPTMS was applied from a boiling aqueous solution of isopropanol. The silanization solution was prepared by adding 0.5g of MPTMS to a solution of 0.5g dH_2O and 20g of isopropanol. When the solution was brought to the boil and started to condense and reflux, glass slides were immersed for 10 mins, then carefully rinsed with isopropanol, blown with a nitrogen stream and cured in the oven at 105°C for 8 min. In order to increase surface coverage with MPTMS, the procedure of immersing in MPTMS, rinsing and curing was carried out three times altogether. The presence of the MPTMS layer was confirmed by contact angle measurements. The adhesion of the silver films was found to be good enough to withstand all subsequent treatment steps without affecting their optical properties.

A 50nm thick silver film (>99.99% purity, Aldrich) was deposited in an Edwards Auto 306 vacuum deposition system equipped with e-beam heating apparatus. Using an adjustable shutter, half of the slide was coated with silver. The vacuum was then broken so that the thickness and dielectric constants of the silver films could be measured (results presented in the next section). Prior to the deposition of the spacer layer, the slides which were half-coated with a silver film were carefully cleaned by rinsing in isopropanol and dH_2O. A silica spacer layer (silicon dioxide, 99.99%, Aldrich) with varying thickness was grown subsequently onto the whole slide. The range of silica thicknesses is tabulated in table 3.1. Silica represented a suitable candidate for a spacer material because of simplicity of deposition within a broad range of film thickness, a medium-high value of the refractive index ($\sim$ 1.46 at 670nm) and its good reproducibility. The growth of the films was monitored in-situ by a thin film monitor (TFM 5, Edwards). Normally, the deposition process was commenced when a pressure below 3×10^{-6}mbar was reached and the typical process pressure ranged between 10^{-5} and 2×10^{-5}mbar. The deposition rate as well as temperature of the substrates slightly varied from deposition to deposition.

3.2.1.2 Fluorophore immobilisation

Cy5 fluorescent dye (Amersham Bioscience) was immobilised on the silica film. To guarantee the formation of the dye monolayer, the dye molecule was chemically modified so that it can be attached to the glassy surface (such as silica) in a single step. The method of dye modification as described in [13] was used. As part of this process, the polyelectrolyte (charged polymer molecule) [14] poly(allylamine) hydrochloride (PAH) was used, which is, at neutral pH, a positively charged molecule with chemical structure shown in fig. 4.6a.

Polyelectrolytes (PELs) will be discussed in more detail in section 4.3.2.

In this procedure, PAH (10^{-4}mol) and sodium hydrogen carbonate (5×10^{-5}mol) were dissolved in 5ml of dH_2O. Separately, 10^{-5}mol of Cy5 dye (monofunctional, with one NHS reactive group) was dissolved in dimethylformamide (DMF) at 2°C. The dye solution was added to the polyelectrolyte solution with rapid stirring and then incubated in the dark for 2 hours. Acetone was then added to precipitate the Cy5-polyelectrolyte conjugate from solution. The polyelectrolyte was recovered by centrifugation followed by drying at room temperature. The Cy5-polyelectrolyte conjugate is positively charged and soluble in aqueous solution.

In the immobilisation procedure the slides were first treated in an oxygen plasma (Harrick) for two minutes to establish a negative surface charge. Plasma-treated slides were subsequently immersed in aqueous solution of Cy5-PAH for 25 minutes, carefully rinsed in deinonised water and dried. Attachment is achieved by electrostatic attraction of the Cy5-PAH molecule compound to the negatively charged surface via a positively charged amino group. The electrostatic nature of attachment guarantees the formation of a molecular monolayer of the compound. The cross-section of the sample is illustrated in fig. 3.1. The advantage of such a sample profile is two fold. Firstly it combines both the metal

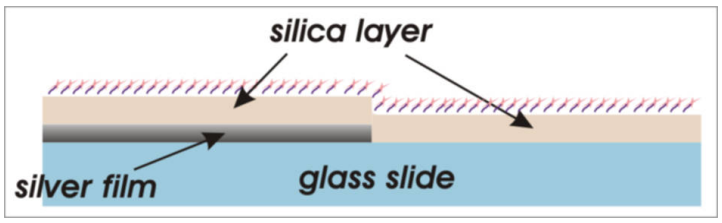

Figure 3.1: Schematic of the sample layered structure for SPCE measurements

and metal-free area onto a single sample, where the surface density of the fluorophore should not vary significantly over the entire sample area. Secondly the dye molecules are concentrated on the surface in the form of a molecular monolayer. This strictly surface--bound immobilisation scheme features zero bulk-generated fluorescence and enables both far-field measurement of the fluorophore-layered structure interaction and the detection of fluorescence intensity variations.

3.2.2 Sample characterisation

3.2.2.1 Ellipsometric measurements

The major characterisation steps involved the determination of thicknesses and dielectric constants of the silver and silica films by means of spectroscopic ellipsometry. A precise knowledge of the film thicknesses (beyond the accuracy offered by the thickness monitor) and their dielectric constants was necessary for interpretation of the experimental results and to facilitate comparison between the experiment and the mathematical model.

Ellipsometry is a technique which enables determination of thicknesses and dielectric constants from the properties of the light reflected from the measured sample. Linearly polarised light at the input generally becomes elliptically polarised after the reflection from a flat surface. The two components of the linearly polarised wave (*p*- and *s*-) experience different attenuation and phase shift at the reflection [15], which can be described by complex Fresnel reflection coefficients r_p and r_s. Ellipsometry measures the ratio of these complex reflection coefficients. The measured data is expressed using Ψ and Δ, which represent the change in amplitude and phase, respectively, after reflection. Ψ and Δ are related to the ratio or r_p and r_s in the form (called the ellipsometric equation) [16]

$$\frac{r_p}{r_s} = \tan\Psi \cdot e^{i\Delta} \tag{3.1}$$

and the parameters Ψ and Δ are defined as

$$\tan\Psi = \frac{|r_p|}{|r_s|} \qquad \text{and} \qquad \Delta = \delta_p - \delta_s \tag{3.2}$$

where δ_p and δ_s refer to the phase of the *p*- and *s*- component of the reflected wave, respectively. In a multi-wavelength measurement (spectroscopic ellipsometer) the parameters are measured for each wavelength.

In the measurements performed by means of polarisation modulation ellipsometry [16] (which was the case in this work) it is convenient to express the measurement data using parameters I_s and I_c. They are functions of both Ψ and Δ and their mathematical description depends on the configuration of the polarising elements in the system [17]. The accurate determination of Ψ and Δ for arbitrary sample composition can be obtained from the parameters I_s and I_c for measurements performed at two configurations of the polarising elements (i.e. orientations of their polarisation axes) in the ellipsometer optical path (fig. 3.2).

Generally, for a multilayer system information such as refractive index and thickness of the layers can not be directly extracted from the wavelength-dependent parameters Ψ and Δ. A model is required to fit the experimental data and the characteristics of the sample can be obtained from this fit.

Experimental

The measurements were carried out on the spectroscopic ellipsometer Jobin-Yvon UVISEL (France). A schematic diagram of the instrument is shown in fig. 3.2. Polychromatic light

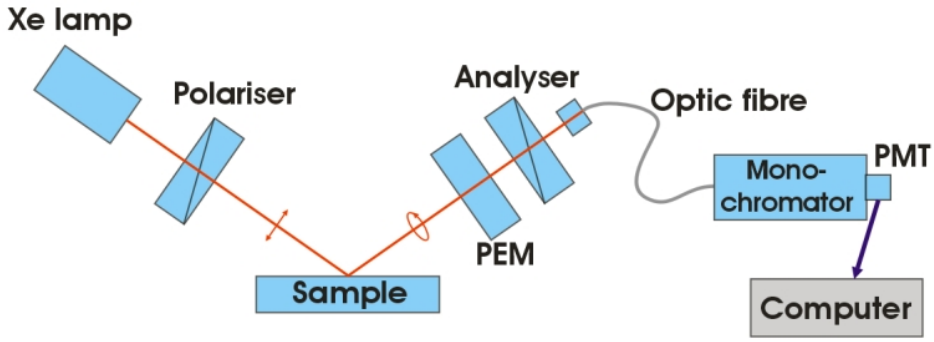

Figure 3.2: Schematic of the spectroscopic ellipsometer Jobin-Yvon UVISEL

from a xenon lamp passes through the first polarizer which establishes a linear polarization. The probing beam reflects at an oblique angle from the sample surface. The output head comprises a photoelastic modulator (PEM) and an analyzer that resolves the polarization state of the reflected beam. A high-resolution grating monochromator selects sequentially each wavelength onto the detector (PMT).

For the measurement, two geometries were used. Reflection geometry with a 60° angle of incidence for determination of the ellipsometric parameters and transmission geometry for measurement of transmission of the silver films. The measurement comprised two steps. In the first step, dielectric constants and thicknesses of the silver films were determined. Since 50nm silver behaves as an opaque layer, the dielectric constants could be determined directly from the measurement in the reflection geometry. Subsequently, measurements in the transmission geometry were performed in order to determine the thicknesses of the silver films. In the second step, the ellipsometric parameters of the silver-silica layered system were measured and thickness and refractive index of the silica films were obtained from the model. Dispersion of the silica layer was modelled using the DeltaPsi^{TM} software by a Cauchy dispersion formula including absorption [16]. Measurements were carried out on each sample and the experimentally-determined values are displayed in table 3.1.

	Thickness [nm]	Diel. constant measured [n+kj]	Diel. constant reference [n+kj]
Silver	49 $\pm$ 3	0.15 - 0.19 + 4.3j	0.14 + 4.3j
SiO_2	10 - 480	1.42 - 1.46 + 0j	1.46 + 0j

Table 3.1: Thickness and dielectric constants of the silver and silica films obtained from ellipsometric measurements. 10-480nm is the range of silica film thicknesses. The n and k values are displayed for wavelength 670nm. The reference values were taken from [18]

The measured thicknesses of silver films were very close to the nominal value (50nm). The measured refractive index of the silver varied slightly from sample to sample, but the index of absorption was almost constant and close to the reference value. The dielectric constants of the silica spacer layer were almost constant within the broad range of thickness as prepared and also were very close to the reference values.

3.2.2.2 Other characterisation methods

Contact angle measurements were used to measure the hydrophobicity of the sample before and after the MPTMS deposition. A FTÅ-200 instrument was used. The computer software analyses the drop shape of a liquid on the surface and reports the contact angle with minimum intervention of an operator. The presence of an MPTMS layer on glass was accompanied by an increase of the water contact angle from less than 4° for piranha-cleaned slide to >50° after the MPTMS deposition.

For confirmation of the presence of dye on top of the silica film, slides were analyzed in a fluorescence array scanner (Affymetrix, GMS 418). The scanner measures the spatial density of fluorescence from the area of a sample. Two light sources can be used (green laser diode with λ_{em}=532nm and red laser diode with λ_{em}=635nm). Focused laser beam illuminates the sample from above and the fluorescence, emitted above (i.e. into the air) is detected with a photomultiplier tube. Sample, placed onto a linear translation stage, is continuously moved while scan is being performed line-by-line across the sample. The fluorescence images can be plotted in false colours (as presented later in chapter 4) with a spectral range of colours.

The scanner measurements (performed with the red laser) indicated that the coverage was homogenous and uniform but that the coverage density fluctuated from sample to sample. These fluctuations did not affect the SPCE measurements, as a ratiometric approach was employed.

3.2.3 SPCE measurements

The sample slide is attached to a hemi-cylindrical prism made of BK7 glass which is designed in a manner to ensure that the illuminated spot on the sample lies at the center of curvature of the slide-prism system. A laser diode with peak emission wavelength λ=635nm (Hitachi HL6344G, Thorlabs) delivering an output optical power up to 10mW in a single mode, linearly polarised beam, was used as an illumination source. The output optical power is monitored by an integrated photodiode and controlled with a laser diode controller (LDC500, Thorlabs). In these experiments, the output power was maintained at 0.8mW in continuous mode. The laser beam was passed through a 1mm-diameter circular aperture, bandpass excitation filter (Omega Optical XF1069) and focused by a pair of lenses into a 1.5mm-diameter spot. The prism-slide assembly is positioned on a motorised rotary stage (Physik Instrumente M-038DG) which co-rotates with the excitation light source. Rotation and scanning parameters, as well as data acquisition are computer-controlled with a custom-written LabVIEW program.

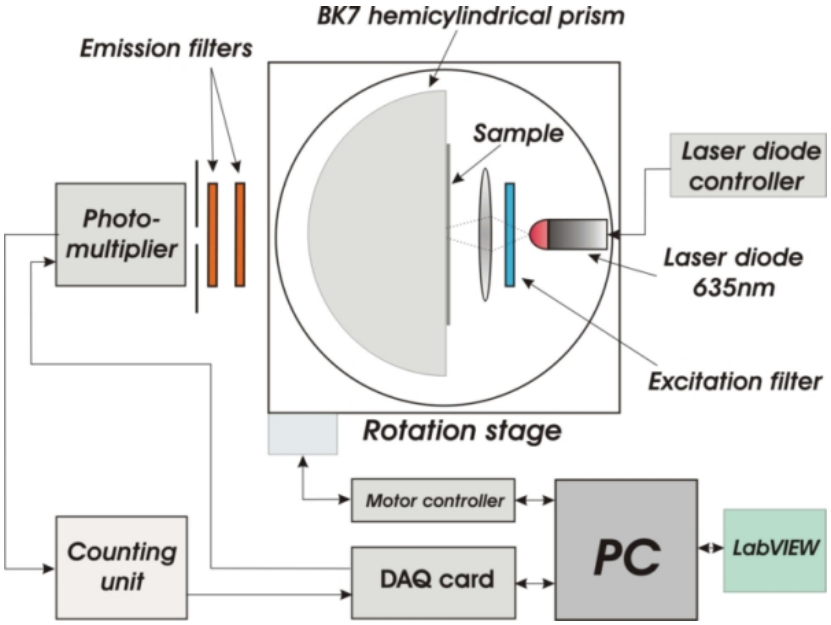

Figure 3.3: Plan view of the experimental setup for detection of a fluorescence anisotropy

The light source - prism system is rotated through a predefined angular range and the intensity corresponding to each angular position is detected with a photomultiplier tube (Hamamatsu H6780-20), which is coupled to a photon counting unit (Hamamatsu C6465). This unit generates pulses compatible with TTL logic, and are counted by the Counter/Timer feature of the data acquisition card (Keithley). Two bandpass emission filters (both Omega

Optical XF3076) are used to suppress scattered and reflected excitation light. The fluorescent spot-detector distance was 15 cm. A 1mm wide vertical slit placed in front of the PMT aperture restricts the acceptance angle to less than 0.5°. The plan view of the experimental setup is displayed in fig. 3.3.

A fixed angle of incidence of 50° with respect to the sample normal was chosen to enable excitation of both vertically and horizontally oriented dipoles. A schematic of the excitation/detection geometry is shown in fig. 3.4. Fig. 3.4a illustrates the orientation and polarisation of the laser with respect to the sample surface in a perspective view. For the whole set of experiments only p-polarised orientation of the laser was used. Fig. 3.4b shows the orientation and polarisation of the laser with respect to the detection direction in a side view. It can be seen that the sample is excited externally to the prism and detection is

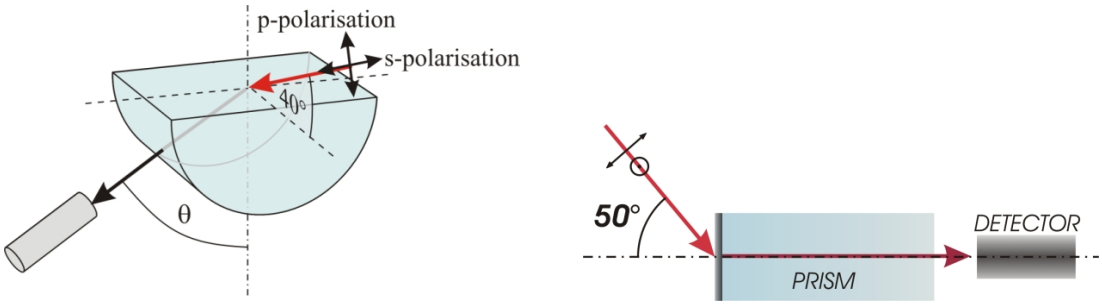

Figure 3.4: Experimental geometry used for the detection of SPCE from fluorophores immobilised on top of a thin silica layer. (a) Perspective view: detector position is fixed, represents the actual polar angle of fluorescence emission. P-polarisation of the incident beam denotes that orientation of laser electric field is lying in plane of incidence. (b) Experimental geometry - side view. P-polarised orientation of laser beam is represented by the arrow lying in the plane of incidence

through the prism at an angle θ. This corresponds to the reversed-Kretschmann configuration where the excitation is not coupled to a surface plasmon. All experiments were carried out in air.

3.3 Theoretical model

Theoretical calculations of the angular distribution of radiation as well as the detectable emission intensities were based on the mathematical model described in section 2.3.2 and which was developed by Jörg Enderlein as a part of the project collaboration.

The modeling procedure proceeds in several steps. First, the excitation intensity of a molecule of a given orientation and position is calculated. The excitation intensity is proportional (neglecting any saturation effects) to the absolute square of the product of the

local electric field amplitude vector and the molecule excitation dipole vector. The electric field $\vec{E}_{ex}$ of the excitation light is expressed as a sum of the field incident and reflected from the multilayer structure in the form

$$\vec{E}_{ex} = \sqrt{w_p}\left[\vec{n}_p + \vec{n'}_p r_p\left(\theta_{inc}\right)\right] + \sqrt{w_s}\vec{n}_s\left[1 + r_s\left(\theta_{inc}\right)\right] \tag{3.3}$$

where $r_{p,s}(\theta_{inc})$ are the reflection coefficients for a plane *p*- or *s*-wave incident at angle θ_{inc} on the layered system, w_p and w_s are the relative intensities of the *p*- and *s*-wave components of the incident light, $\vec{n}_p$ and $\vec{n'}_p$ are unit vectors along the polarization of the incident and reflected *p*-wave, and $\vec{n}_s$ is the unit vector along the polarization of the *s*-wave. The radiation of the dipole through a layered structure is described by the equation (2.18) on page 27.

The measurable angular distribution of radiation is now given by the integral of the product of eq. (3.5) (excitation efficiency) and eq. (2.18) (emission strength) over all molecule orientations (α, β) weighted with a distribution function of molecule orientations $w(\alpha, \beta)$:

$$I_{em}(\theta, \phi) = \int_0^{\pi} \sin\beta\, d\beta \int_0^{2\pi} w(\alpha, \beta) I_{ex}(\alpha, \beta) S(\theta, \phi, \alpha, \beta, z_d, n_i, d_i, n_{glass}, n_{air})\, d\alpha \tag{3.4}$$

where $i \in 1, 2$ (only 2 intermediate layers, silver and silica).

The function $S(\theta, \phi, \alpha, \beta, z_d, n_i, d_i, n_{glass}, n_{air})$ is defined in section 2.3.2. Distance z_d in eq. (3.4) is equal to zero as flurophores are placed directly upon the layered structure. The excitation efficiency $I_{ex}(\alpha, \beta)$ is given by

$$I_{ex}(\alpha, \beta) = \left|E_{ex,x} \sin\beta\cos\alpha + E_{ex,y} \sin\beta \sin\alpha + E_{ex,z} \cos\beta\right|^2 \tag{3.5}$$

with $E_{ex,x}$, $E_{ex,y}$ and $E_{ex,z}$ are the *x*, *y* and *z* components of the excitation field amplitude as given by eq. (3.3).

The calculations were performed for the emission wavelength λ=670nm and for the following values of refractive indices: n_{glass}=1.52, n_{air}=1.0 and refractive index of silica n_{SiO_2}=1.46 was assumed to be equal for all samples (see table 3.1). Since the thicknesses and dielectric constants of the silver films did not vary significantly they were also fixed for all samples. Silver thickness d_{Ag}=49nm and dielectric constant 0.17+4.3j were used. To allow for inaccuracies in the determination of spacer thickness, this parameter was allowed to vary during fitting. The orientation of the dipoles was also varied during the modelling procedure so that the best fit of the experimental and model SPCE angular profiles was achieved.

3.4 Results and discussion

The angular scans were carried out through the angular range $(-80°, 80°)$ of the glass half--space with 0.5° step increment. Integration time at a single position, PMT gain settings and laser output power were kept constant throughout the entire set of experiments. With reference to figures 2.10 and 3.4 the fluorescence emission profile is recorded for varying angle θ while ϕ=0°.

3.4.1 ADE measurements

The graphs of the SPCE angular profiles with varying spacer thickness are plotted in fig. 3.5. As expected, the angular position of the SPCE peaks shift toward larger angles as the spacer thickness increases as a consequence of the coupling condition described in section 2.4.2. The SPCE peak halfwidth broadens when shifted towards larger angles, from ∼1° for 10nm spacer thickness to ∼5.5° at 130nm. At around 130nm of the spacer thickness a second peak emerges just above the critical angle (fig. 3.5c). As the silica thickness further rises, the peak present at larger angle further broadens and decreases in intensity, until finally disappearing around 260nm (fig. 3.5e). The halfwidth of the lower-angle peak rises only negligibly from ∼1° at ∼140nm to maximum 2° at 260nm and then decreases again. The appearance of multiple peaks with rising spacer thickness is consistent with the experimental observations of Gryczinski [19, 20] and the theoretical work of Calander [21]. Their origin will be discussed in more detail in the next section.

The experimentally measured data (denoted with dots in the graphs displayed in fig. 3.5) are overlaid with the best fit curves obtained from the model (solid lines). As can be seen, very good agreement between model and experiment has been achieved. The effect of broadening of the peaks bases, observed for larger spacer thicknesses, will be addressed in the next section. The modelling procedure comprised several steps. First, the angular emission profiles were modelled using the experimentally determined values of silica film thickness and an isotropic dipole orientation of molecules was assumed. In the second step, the spacer thickness was allowed to vary so that the best match of the experimental and model curve is achieved. The dipole orientation remained isotropic. The graph in fig. 3.6 shows the comparison between the experimentally determined spacer thickness values (represented by the straight blue line) and the best fit obtained by the modelling procedure described above (red dots). In the ideal case of perfect experiment-model thickness match the red dots would coincide with the blue line. Also this result indicates that overall good

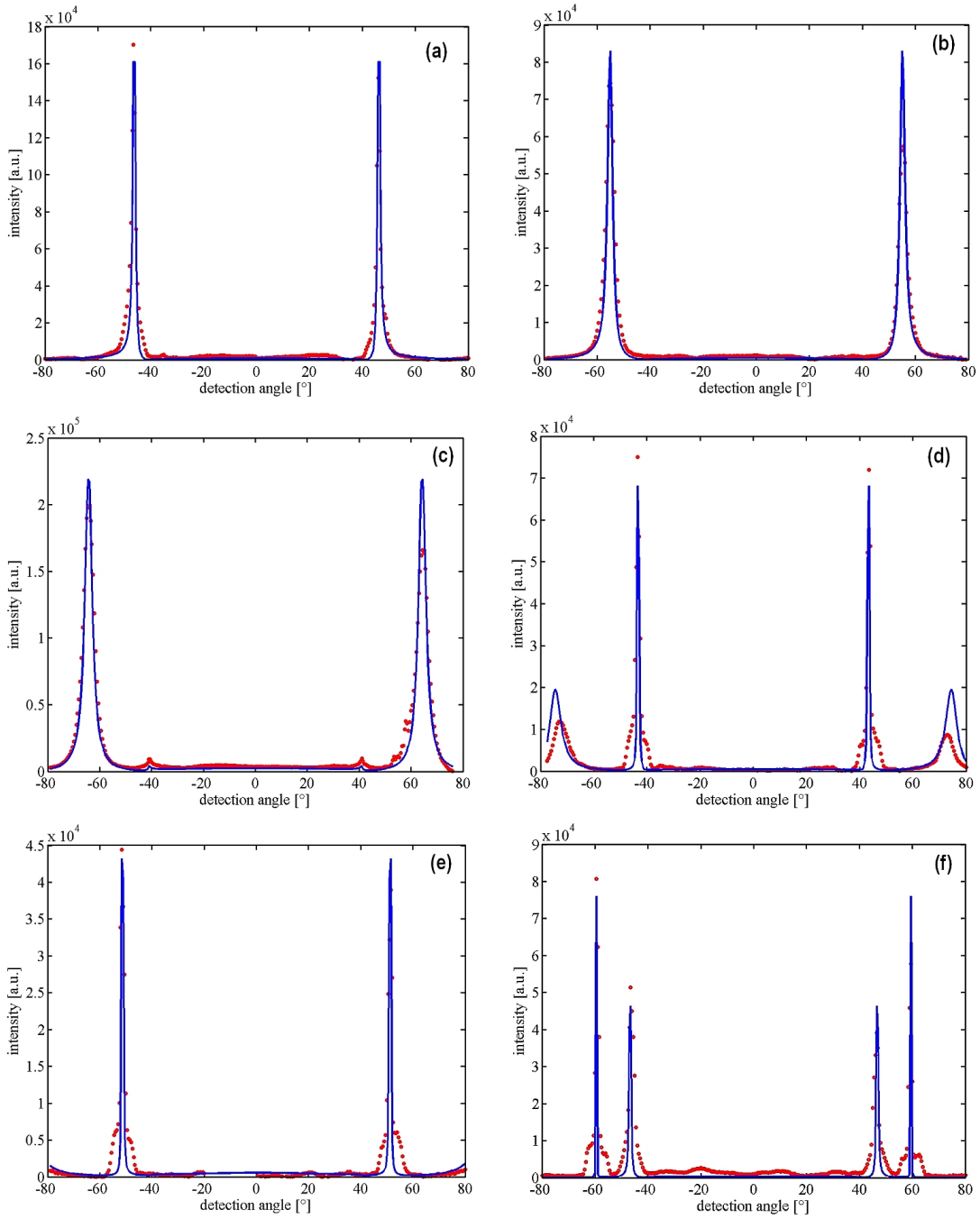

Figure 3.5: Experiment-model comparison of SPCE angular profiles for various values of the spacer thickness. Experimental data (dots) for an experimentally determined spacer thickness are overlaid with best-fit model curves (solid lines)

agreement between experimental data and the theoretical model was achieved. In the final step, the molecule orientations were fitted for the spacer thickness obtained from the second fitting step and the best correlation between experimental data and theory was achieved for purely horizontal orientation of molecules (lying in the sample plane). It is important to note that the orientation was modelled for all samples simultaneously.

During the whole fitting procedure the remaining model parameters such as silver film

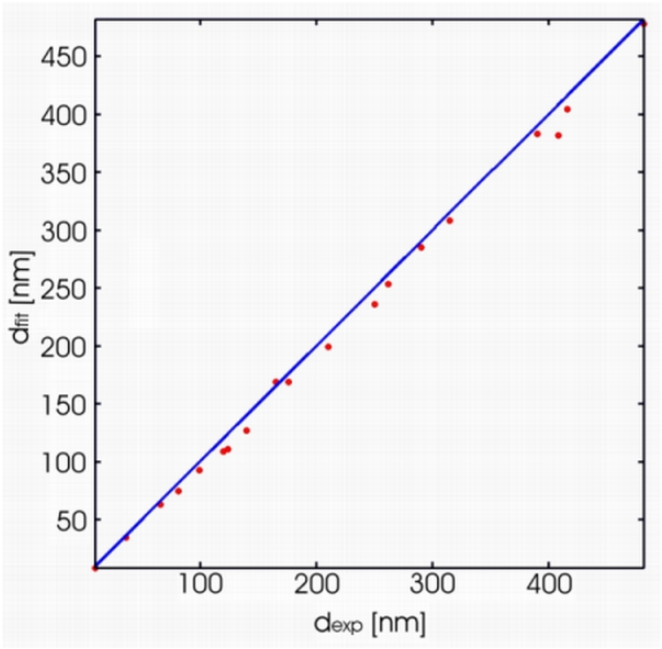

Figure 3.6: Comparison between experimentally determined spacer thickness value (straight blue line) and the best fit obtained by the modelling procedure described in the text (red dots). In the ideal case of perfect experiment-model match, the dots and the line would overlap

thickness and silver/silica dielectric constants, that were obtained from the ellipsometric measurements were kept constant in the model. For their values see section 3.3. The small sample-to-sample fluctuations in silver thickness and dielectric constants (table 3.1) had a negligible effect on both shape and width of the peaks.

3.4.2 Polarisation of SPCE

The appearance of multiple peaks is an interesting phenomenon. The first step to reveal their origin is to realise how dipoles with various orientations contribute to the emission pattern. The emission intensity into angle (θ, ϕ) is described by eq. (2.18) as a sum of components along each major coordinate axis. If the plane of observation is restricted to θ (i.e. $\phi = 0°$), with respect to eq. (2.18) the emission pattern is written as a sum of coefficients $S^{\perp}$, $S^{\parallel,c}$ and $S^{\parallel,s}$, which are only functions of angle θ and thicknesses and dielectric constants of the layers. Calculated emission patterns for dipoles oriented along the x, y and z axes (with reference to fig. 2.10) and for the sample structure corresponding to the angular profile in fig. 3.5f (50nm silver and 390nm silica spacer) are presented in fig. 3.7. It is interesting that the emission angle is the same for dipoles with orientation vertical and horizontal in the plane of observation (around 47°), whereas a horizontal dipole with

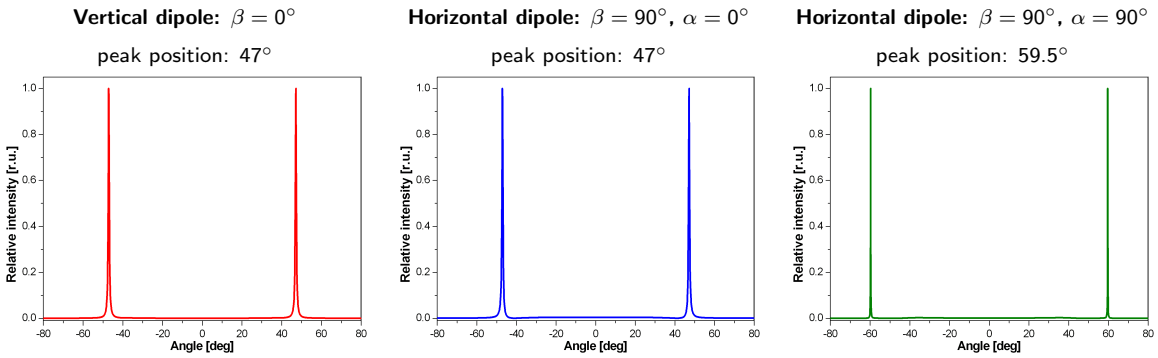

Figure 3.7: Angular positions of the emission peaks originating from the dipoles oriented along the major coordinate axes, observed for varying angle θ. The layered structure corresponds to that in fig. 3.5f

orientation perpendicular emits into a different angle (around 59°). This effect was also observed for even larger values of spacer thickness.

In the previous section it was mentioned that the best fit of the experimental data with the model curve was obtained for purely horizontal dipoles ($\beta = 90°$). The orientation of the dipoles within this plane is expected to be uniform with $\alpha \in (0°, 90°)$. In the experiment, the *p*-polarisation of the illumination beam was chosen (section 3.2.3) which targets only dipoles with angle $\alpha = 90°$. With respect to figures 3.5f and 3.7b,c it is therefore interesting to ask why the peak at 47° is observed. Since the excitation field is equal to the sum of the incident and reflected field (eq. (3.3)) and with the reflection coefficients $r_{p,s}$ dependent on the composition of the layered structure, the reflected field also contains a non-zero component along the x-axis, exciting dipoles with $\alpha = 0°$ orientation.

Gryczinski et al. [19] reported that peaks at various angles can be both p- or s-polarised, which is interesting, as SPCE, as a reverse SPR effect, is expected to be only *p*-polarised. To verify this, the polarisation of the SPCE peaks was measured by placing a linear polariser between the prism and detector. In the experimental geometry used the *p*-polarisation denotes that the electric vector is oriented parallel to the detection plane (or along the *x*-axis with respect to fig. 2.10). Table 3.2 summarises the angular positions and peak polarisations of the profiles presented graphically in fig. 3.5 (in the polarisation measurements the sample with 142nm spacer was used instead of that with 130nm). The fluorescence emitted into a single peak is *p*-polarised. As the spacer thickness increases, the newly emerging peak changes polarisation to *s*- and the alternation of *p*- and *s*- polarisations continues with further rising spacer thickness.

Since multiple peaks appear after sufficient thickness of the spacer layer has been achieved, their angular position and polarisation can be explained by a coexistence of surface plasmon

Spacer thickness [*nm*]	Peak position [*deg*]	Peak polarisation
36	47.5	p
120	63.5	p
142	41.5	s
	67.5	p
176	43.5	s
	73.5	p
262	51.5	s
390	47.0	p
	59.0	s

Table 3.2: Experimental results of polarisation measurements of the emission peaks for various values of the silica spacer thickness

modes and waveguide modes in the silica layer with air and silver cladding. The *p*-polarised peaks originate from hybrid plasmon-coupled and waveguide modes (plasmon modes, out-coupled into the glass side are supported by the *p*-polarised (or TM) modes within the spacer layer), whereas the origin of the *s*-polarised peaks stems from waveguide modes only [21]. The emission from the fluorophores with given orientation is affected by the existence of the waveguide structure. The mode structure of the waveguide for each silica layer thickness defines the angles and polarisations at which the modes can exist, thereby peaks with *p*- and *s*- polarisations occur at different angles.

The origin of the peak bases broadening, observed experimentally for larger spacer values (figs. 3.5d-f), can be distinguished with regard to the peak polarisations. Since the out-coupled modes are waveguide-supported, imperfections of the interfaces (such as surface roughness) on both silver-silica and silica-air will have an effect due to multiple reflections within the spacer-formed waveguide. This contrasts with the pure surface-plasmon modes (those in figs. 3.5a-c), where the fluorescence radiation excites surface plasmons directly and therefore the effect of surface roughness is not so significant (perfect match of the experimental and theoretical peak shape in figs. 3.5a-c). Larger amount of broadening, which can be seen for the *s*-polarised peaks as compared to the *p*-polarised ones. This could be attributed to the fact that the electromagnetic field, corresponding to the *s*-polarised modes, is less concentrated to the silver-silica interface and therefore these modes are more scattered at the silica-air interface roughness, which in turn results in a certain peak dispersion.

By comparing the polarisation of the peaks at the given angle (table 3.2) and the contribution from dipoles with various orientations (fig. 3.7) it can be seen that the peak at 47°

originates from the dipoles with momentum component parallel to the detection plane and that at 59° from the dipole with component lying perpendicular to this plane. With regard to the previous findings no vertically-orientated dipoles were assumed to contribute to the detected signal. By performing calculations for other spacer thicknesses it can be concluded that dipoles oriented vertically and horizontally in the plane of detection contribute the *p*--polarised light, whereas horizontal dipoles oriented perpendicular to the detection plane contribute solely to the *s*-polarised light. This also explains why an *s*-polarised peak is not observed if the spacer layer is too thin.

3.4.3 Fluorescence intensity measurements

In the quantitative study the fluorescence intensities emitted from both the silver-coated and silver-free area of a single slide (fig. 3.1) were directly compared. For each value of the spacer thickness, the SPCE intensity is expressed as a fraction of the total amount of fluorescence emitted into the glass in the absence of metal. The assumption of homogenous surface coverage density over the whole slide is crucial for the ratiometric intensity evaluation. This assumption can be justified by the fact that the dye is immobilised onto a single type of surface, with no reason for variations across either type of material underneath. Moreover, ratiometric analysis ensures independence of the experimental geometry (distance from prism to detector, dimensions of prism and illuminated spot diameter). Although all the parameters are kept constant throughout the whole set of measurements, it is in fact only necessary that they are maintained for the course of the measurement on a single slide.

Prior to the measurement of the SPCE versus non-SPCE intensity, experiments were carried out in order to establish the effect, if any, of the variable thickness SiO_2 layer on the measured intensity in the absence of a metal layer. It is expected that the presence of silica with variable thickness would have a very negligible effect on the detected fluorescence intensity as its refractive index is almost equal to the refractive index of the glass substrate. Unlike the excitation field above the metal-silica layers, described in previous section, the excitation field is constant in this case. As only the *p*-polarised orientation of the laser is used, the reflected wave is almost equal to zero due to the $\theta_{inc} = 50°$, which is very close to the Brewster angle of the silica/air interface. The excitation field is thus equal to the incident field.

To investigate this, a special batch of glass slides which were overcoated with silica was prepared for several values of silica thickness. For each thickness, 3-4 samples were pre-

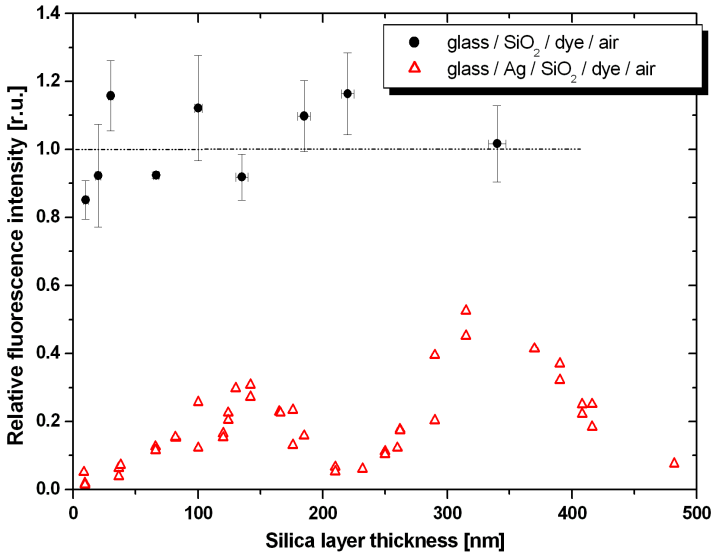

Figure 3.8: Effect of a semitransparent silver film on the fluorescence intensity emitted into the glass slide. Each experimental data point (triangles) represents the ratio of plasmon-coupled fluorescence intensity and intensity in the absence of the metal film for a particular spacer thickness value. The metal-free intensity profile, obtained from an independent set of measurements, is also plotted (black dots)

pared, followed by deposition of the Cy5 dye monolayer. Following measurements in the fluorescence scanner it was found that surface density of the immobilised dye was constant on a single slide, but rather large fluctuations were observed from sample to sample. Fluorescence intensities obtained from the angular scans were averaged over the number of measurements and are shown in fig. 3.8 (full black dots). The horizontal line at unity illustrates the ideal case, with zero effect of spacer thickness variations on the intensity. Although the experimental data oscillate about this line, no trend with increasing silica thickness is observed, suggesting that the effect of an intermediate SiO_2 layer is negligible. The large error bars are caused by the sample-to-sample fluctuations of dye surface coverage density.

For the ratiometric measurements, two samples, half-coated with silver, were prepared for each spacer layer thickness. Two angular scans were carried out on each of the metal and metal-free areas of the slide. The total intensity was calculated and averaged, and the ratio of intensity with and without metal was plotted in the graph in fig. 3.8 (triangles). The results indicate that the optimum silica spacer thickness for a single emission peak is 130nm, which is coincidently the largest thickness where fluorescence is emitted into a single peak. It can be seen from the graph that the intensity corresponding to this spacer thickness is only $\sim$30% of that measured in the absence of a metal layer. A second max-

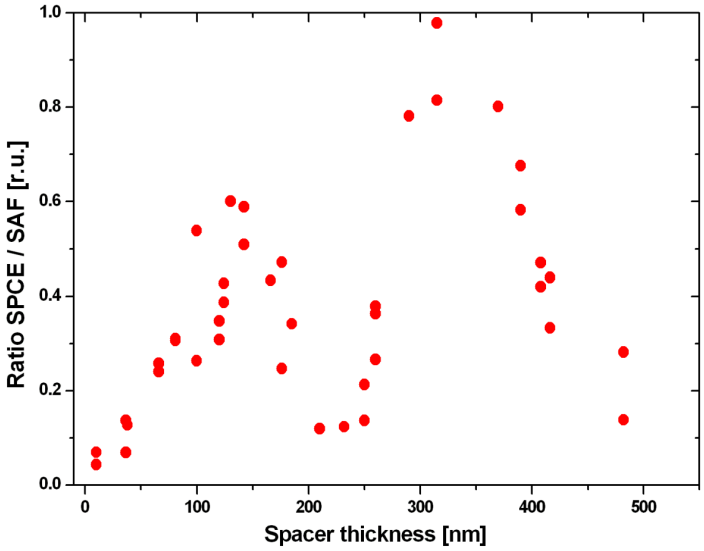

Figure 3.9: Ratio of plasmon-coupled fluorescence intensity and intensity emitted into the SAF angular range in the absence of a metal film

imum is observed for the spacer thickness ∼340nm, where the total out-coupled intensity rises by a factor of two to ∼60% of the metal-free intensity, but this is counterbalanced by the loss of the fluorescence directionality (since fluorescence is emitted into multiple peaks at different angles). When only the fluorescence emitted into the SAF range (i.e. 41° - 80°) was extracted from the total emission it was found that the SPCE/SAF ratio increases to ∼60% for the spacer thickness 130nm as shown in fig. 3.9.

It is important to note that the quantitative data presented above are *only* valid for the given experimental geometry and structure of the sample, as the excitation field intensity varies significantly within the broad range of spacer thicknesses as a result of interference effects.

In fig. 3.10, the ratiometric experimental data which were plotted in fig. 3.8 were compared with the theoretical model. The parameters of the model are exactly matched to the experimental parameters. Agreement between the experimental data (dots) and the model curve (solid line) is very good up to ∼300nm of silica thickness. However, for large values of the spacer thickness, although there is a general agreement with regard to the thickness value which yields maximum ratiometric signal, the experimental data for the second peak yields a maximum ratiometric signal which is about twice that of the theoretical value. It is believed that this discrepancy can be caused by the choice of the illumination geometry: since the illumination beam makes an angle of 50° with respect to the sample normal, following the reflection from the silver film it is likely that a fraction of the focused excitation light may be captured within the silica layer, occurring above the critical angle of the

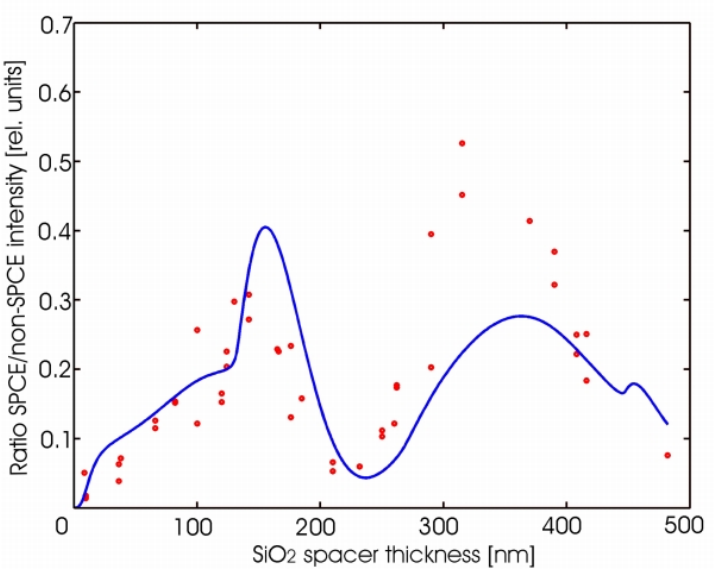

Figure 3.10: Comparison of experimental ratiometric data (solid dots) and the model curve (solid line) of the total glass-emitted fluorescence

silica-air interface ($\sim 43°$). Such a wave is capable of efficiently exciting the surface-bound molecules via the evanescent field from the totally internally reflected wave. This effect is not taken into account in the theoretical description of the excitation field expressed by eq. (3.3).

3.5 Conclusions

The emission profile and dependence of emitted intensity on the metal-fluorophore spacer thickness for a silver-Cy5 dye SPCE system was studied in this work. The broad range of silica spacer layer thickness was chosen to facilitate a comparison between experimental results and the results of theoretical modelling. Excellent agreement was achieved between model and experiment for the ADE and its variation with spacer thickness. The origin of the multiple emission peaks with alternating polarisation was explained as a consequence of discrete waveguide mode structure supported by surface plasmon resonances in the metal. From the quantitative analysis of the metal-dye separation dependence, it has been demonstrated for the first time that SPCE intensity is reduced compared to the data obtained in the absence of the metal layer, as predicted in [9] and by the model used here. For single-peak SPCE emission, a maximum intensity of 30% of the metal-free value was achieved at the optimal metal-dye spacer thickness of 135 nm for the particular experimental geometry and sample structure. Despite the complexity of the system parameters, which need to be

taken into account, overall good agreement was obtained between experimental results and the theoretical model.

This chapter has presented SPCE results using a basic measurement system where the dependence of emission on the metal-spacer layer and the polarisation behaviour of the emission has been characterised and modelled. The second part of my work, the implementation of an SPCE-based bioassay using a parabolic biochip platform, will be presented in the next chapter.

References

[1] D. Axelrod. Total internal reflection fluorescence microscopy in cell biology. *Traffic*, 2(11):764–774, 2001.

[2] T. Ruckstuhl, M. Rankl, and S. Seeger. Highly sensitive biosensing using a supercritical angle fluorescence (SAF) instrument. *Biosensors and Bioelectronics*, 18(9):1193–1199, 2003.

[3] E. Matveeva, Z. Gryczynski, I. Gryczynski, J. Malicka, and J. R. Lakowicz. Myoglobin immunoassay utilizing directional surface plasmon-coupled emission. *Analytical Chemistry*, 76(21):6287–6292, 2004.

[4] E. Matveeva, Z. Gryczynski, J. Malicka, J. Lukomska, S. Makowiec, K. W. Berndt, J. R. Lakowicz, and I. Gryczynski. Directional surface plasmon-coupled emission: Application for an immunoassay in whole blood. *Analytical Biochemistry*, 344(2):161–167, 2005.

[5] J. R. Lakowicz. Radiative decay engineering 3. surface plasmon-coupled directional emission. *Analytical Biochemistry*, 324(2):153–169, 2004.

[6] K. Vasilev, W. Knoll, and M. Kreiter. Fluorescence intensities of chromophores in front of a thin metal film. *Journal of Chemical Physics*, 120(7):3439–3446, 2004.

[7] F. D. Stefani, K. Vasilev, N. Bocchio, N. Stoyanova, and M. Kreiter. Surface plasmon-mediated single-molecule fluorescence through a thin metallic film. *Physical Review Letters*, 94(2), 2005.

[8] K. Ray, H. Szmacinski, J. Enderlein, and J. R. Lakowicz. Distance dependence of surface plasmon-coupled emission observed using Langmuir-Blodgett films. *Applied Physics Letters*, 90(25), 2007.

[9] J. Enderlein and T. Ruckstuhl. The efficiency of surface-plasmon coupled emission for sensitive fluorescence detection. *Optics Express*, 13(22):8855–8865, 2005.

[10] C. A Goss, D. H. Harych, and M Majda. Application of (3-mercaptopropyl)trimethoxysliane as a molecular adhesive in the fabrication of vapor-deposited gold electrodes on glass substrates. *Analytical Chemistry*, 83(1):85–88, 1991.

[11] P. J. Martin, H. A. Macleod, R. P. Netterfield, C. G. Pacey, and W. G. Sainty. Ion beam-assisted deposition of thin films. *Applied Optics*, 22(1):178–184, 1983.

[12] C. K. Hwangbo, L. J. Lingg, J. P. Lehan, H. A. Macleod, J. L. Makous, and S. Y. Kim. Ion assisted deposition of thermally evaporated Ag and Al films. *Applied Optics*, 28(14):2769–2778, 1989.

[13] J. Kerimo, D. M. Adams, P. F. Barbara, D. M. Kaschak, and T. E. Mallouk. NSOM investigations of the spectroscopy and morphology of self-assembled multilayered thin films. *Journal of Physical Chemistry B*, 102(47):9451–9460, 1998.

[14] G. Decher. Fuzzy nanoassemblies: Toward layered polymeric multicomposites. *Science*, 277(5330):1232–1237, 1997.

[15] M. Born and E. Wolf. *Principles of Optics*. Pergamon Press, Oxford, 6th edition, 1980.

[16] H. G. Tompkins and W.A. McGahan. *Spectroscopic Ellipsometry and Reflectometry: A User's Guide*. John Wiley & Sons, Inc., New York, 1999.

[17] Jobin-Yvon UVISEL user manual.

[18] E. D. Palik. *Handbook of Optical Constants of Solids*. Academic Press, 3rd edition edition, 1998.

[19] I. Gryczynski, J. Malicka, K. Nowaczyk, Z. Gryczynski, and J. R. Lakowicz. Effects of sample thickness on the optical properties of surface plasmon-coupled emission. *Journal of Physical Chemistry B*, 108(32):12073–12083, 2004.

[20] I. Gryczynski, J. Malicka, K. Nowaczyk, Z. Gryczynski, and J. R. Lakowicz. Waveguide-modulated surface plasmon-coupled emission of nile blue in poly(vinyl alcohol) thin films. *Thin Solid Films*, 510(1-2):15–20, 2006.

[21] N. Calander. Surface plasmon-coupled emission and Fabry-Perot resonance in the sample layer: A theoretical approach. *J. Phys. Chem. B*, 109(29):13957–13963, 2005.

Chapter 4

SPCE on a parabolic biochip platform

The previous chapters dealt with the theoretical description of the SPCE effect and its experimental investigation on a planar surface. This chapter describes the implementation of SPCE on a low-cost, high collection efficiency biochip platform. A novel biochip platform based on an array of parabolic elements is described and so also is the modification of this platform for SPCE measurements. The issue of choice of the materials is addressed in terms of both their compatibility with the chip design as well as the stability of the coatings. The design of the read-out device and its raytracing validation are described and the issues of illumination and polarisation are broadly discussed. Ultimately, the proof-of-concept is demonstrated by carrying out a SPCE-based model sandwich bioassay.

4.1 Introduction

It is desirable for afinity-based biosensors to restict the detection of the binding events to the surface containing the immobilised receptors as shown in fig. 2.19. The spatial extent of the detection volume should ideally be of the order of the physical dimensions of the reaction moieties, thereby rendering the sensor immune to reactions occurring in the bulk of a sample. In fluorescence-based sensing schemes, evanescenct field illumination techniques such as described in chapter 2 have been widely used to achieve surface-selective fluorophore excitation. Collection of the surface-generated fluorescence, however, remains challenging as large proportion is emitted above the critical angle. High NA microscope objectives are widely employed to achieve surface-sensitive excitation and collection of fluorescence

emitted at large surface angles [1–4]. However the price and bulkiness of such instruments makes them unsuitable for portable, low cost applications. In the work of Polerecky [5, 6] and Ruckstuhl [7, 8] the challenge of supercritical angle fluorescence (SAF) collection was addressed by designing optical elements capable of capturing and redirecting the large angle fluorescence. These elements can be fabricated with high precision and low cost by injection moulding technology and are suitable for large scale production.

In this work, the advantages of SPCE detection as described in previous chapters are combined with the use of the SAF-based high collection efficiency platform. The major objective is to demonstrate a model bioassay using the SPCE-based optical biochip.

4.2 Solid parabolic collector

An elegant solution to capture fluorescence emitted above the critical angle was proposed by Ruckstuhl [7, 8]. He suggested the use of a solid element in the shape of a truncated paraboloid. The parabolic shape of the element acts as a mirror through total internal reflection that collects the fluorescence light, preferably around the angles of maximum emission. This simple element is capable of achieving collection efficiency comparable to an objective with NA exceeding 1.5 [8]. By using this element the entire SAF range can be captured ($\sim$34% of fluorescence is emitted above the critical angle for isotropic orientation of molecules, lying directly at the glass-water interface).

The principle is illustrated in fig. 4.1. Fluorescence originating from a point located at the top plane of the truncated paraboloid is emitted into a known anisotropic pattern (section 2.3.3). If the paraboloid is truncated at the focal plane and the point source lies at the axis of revolution, the fluorescence emitted into large angles is totally internally reflected at the side face of the paraboloid and subsequently collimated due to the geometrical properties of a parabola. The fluorescence light appears below the parabola in the form of a fluorescence ring (fig. 4.2). The dimensions of the parabola define the range of angles it can capture; in practical applications, where fluorescence detection is performed in aqueous solution, the desired angular range of capture angles exceeds 61° (if the parabola is made of glass/polymer with n=1.52). Restriction of the detection angles can be realised by placing an annular aperture underneath the parabolic element. The second role of the mask is to block fluorescence emitted below the critical angle, which originates mainly from the bulk solution. A detailed description of instruments utilising the parabolic collector can be found in [9–14].

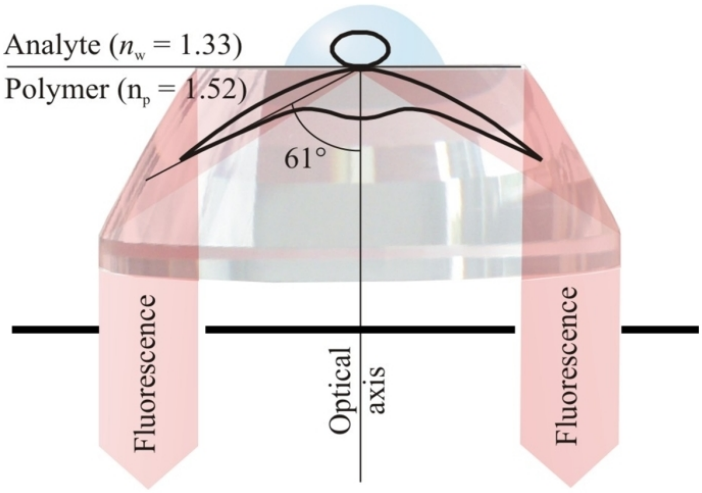

Figure 4.1: Collimation of fluorescence emitted from a point source at a polymer-water interface by a solid parabolic element. Image copyrighted by Thomas Ruckstuhl

The detection scheme can be simultaneously used to provide a TIRF excitation (the left panels in fig. 4.2).

4.3 Array of parabolic elements: optical biochip

The design of the parabolic element facilitates scaling down to millimeter dimensions and integration into an array format. The principle of excitation and detection for a single parabolic element allows the whole array to be illuminated by a single expanded laser beam and the fluorescence collected without element-to-element cross-detection.

4.3.1 Design and fabrication

Our optical biochip comprises a 3×3 array of parabolic elements [15] and is designed as a low cost disposable generic detection platform (fig. 4.2). Each element on the chip is designed with a focal length of f=0.45mm and an upper diameter of 1.8mm, so that the geometrical focus of each truncated paraboloid element lies exactly at its upper surface. This surface serves as the biorecognition area. An annular aperture, placed below each element and setting the range of accessible surface angles between 62° and 80°, is integrated into a single part. The chip is square-shaped with the edge length 20mm. Other important dimensions are shown in fig. 4.2. An image of the chip and the annular mask is shown in fig. 4.3. The chip is fabricated from an optical grade cyclo olefin co-polymer *ZEONEX 480R* (Zeon Corp., Japan) by injection moulding. With this technology, accuracies required

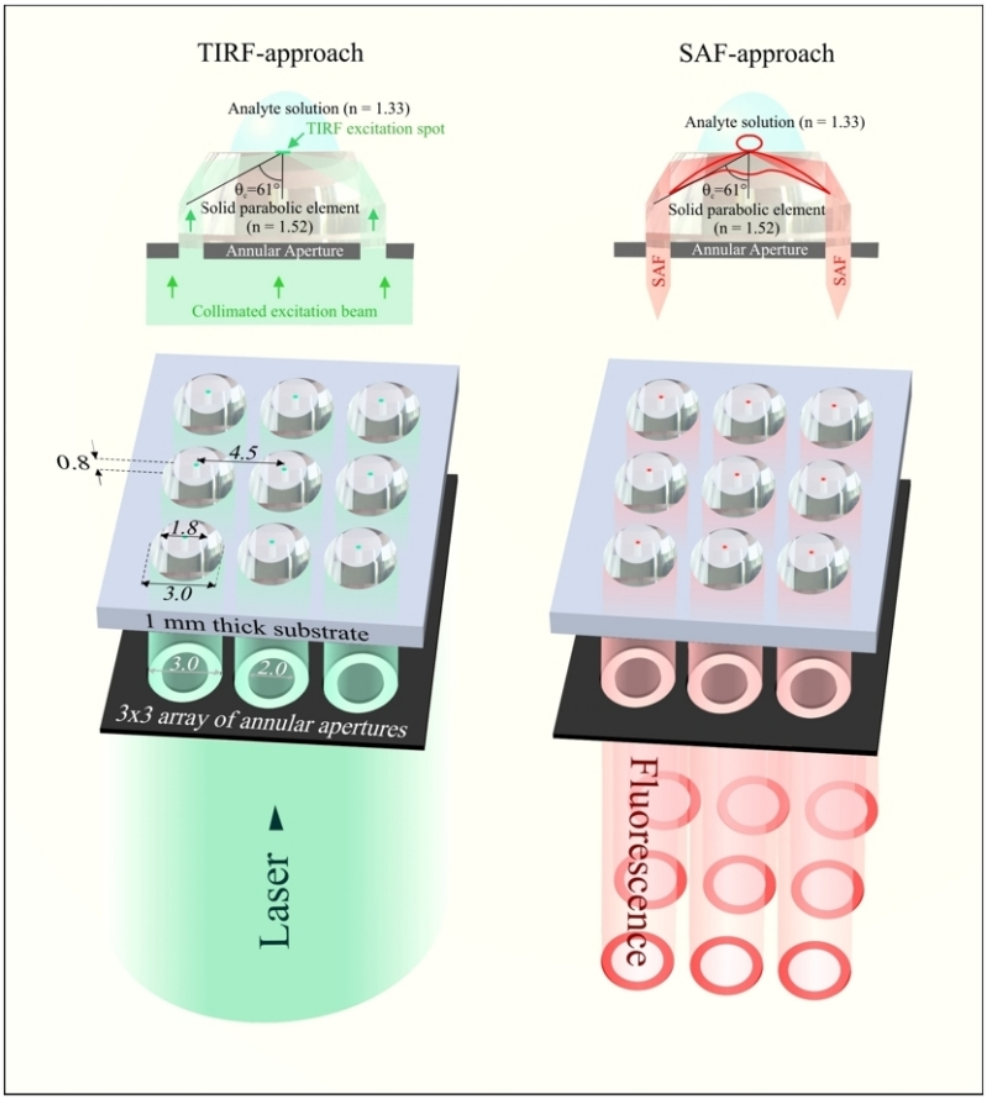

Figure 4.2: Design of the biochip as a 3×3 array of parabolic elements. The panel on the right shows the fluorescence rings. Image copyrighted by Thomas Ruckstuhl

for optical components can be achieved reproducibly in a mass fabrication process. Apart from excellent mouldability, which makes the mass production very cheap without compromising quality, this material possesses optical properties which are superior to commonly used optical polymers such as polycarbonate and polystyrene. It is highly transparent, with very low intrinsic autofluorescence in the red part of the spectrum and is optically interchangeable with glass due to almost identical refractive index. Low water absorption makes it compatible to use with aqueous analytes. Values of the major properties are summarised in table 4.1.

However, during the process of fabrication the chip dimensions were slightly modified which resulted in a shift of the plane of truncation slightly upwards (about 10μm). This means that the collimated laser beam incident on the surface is defocused, forming a ring of illu-

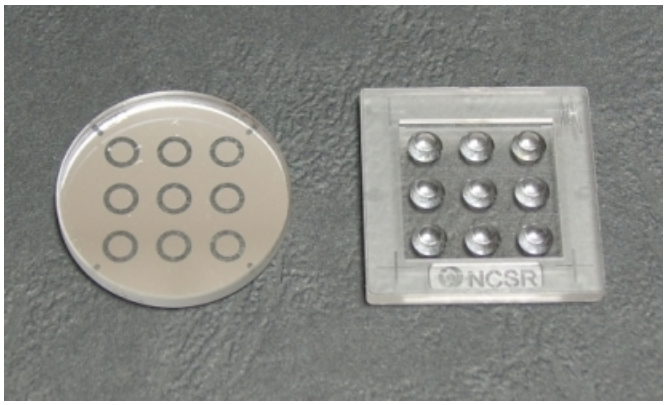

Figure 4.3: Photo of the annular mask and the disposable parabolic biochip

mination. This can, however, be convenient to prevent photobleaching and to average out surface imhomogenities and fluctuations in surface density of the immobilised receptors. On the other hand, the advantage of fluorescence collimation by the paraboloid is lost as it is emitted from a finite area and out of the focal plane. The design of the readout device compensates for this issue.

Water absorption	$< 0.01\%$
Heat distortion temperature	123°C
Absorption coefficient	0.03mm^{-1} above λ=500nm
Abbe number	56.2
Refractive index	1.525 at λ=587.56nm 1.522 at λ=656.27nm

Table 4.1: Properties of *ZEONEX 480R* cyclo olefin co-polymer at temperature 25°C

4.3.2 Metal and spacer layer coating for SPCE measurements

As presented in section 3.4.3 overall fluorescence intensities achievable with SPCE are lower as compared to SAF. On the other hand there are advantages of SPCE, which stem from the presence of the metal layer, that are worth exploiting in biomedical diagnostics. The the most promising advantages are using the metal film to enhance excitation, capability of the metal film to block bulk fluorescence and the possibility of multiwavelegth detection. As shown in section 2.4, the range of SPCE angles forms a sub-set of the entire SAF range, therefore making the parabolic collector perfectly compatible with the SPCE-based sensing scheme. Furthermore, it is straightforward to implement a plasmonic structure comprising a smooth metal film and a suitable spacer layer onto the biochip platform by adding them directly onto the planar top surface forming the recognition area. Thin polyelectrolyte

(PEL) films coated by a layer-by–layer (LbL) technique serve as a spacer layer and also facilitate immobilisation of antibodies.

4.3.2.1 Chip cleaning and vacuum coating

Fresh chips were first precleaned by sonication in 1% Micro90 surfactant solution (Cole--Palmer) for 15 minutes, carefully rinsed in dH_2O and dried in a stream of nitrogen. Subsequently, the chips were cleaned by oxygen plasma (Harrick) for 4 minutes. This is an important step for achieving improved adhesion of metal onto the chip surface. The vacuum coating step proceeded immediately after the plasma treatment.

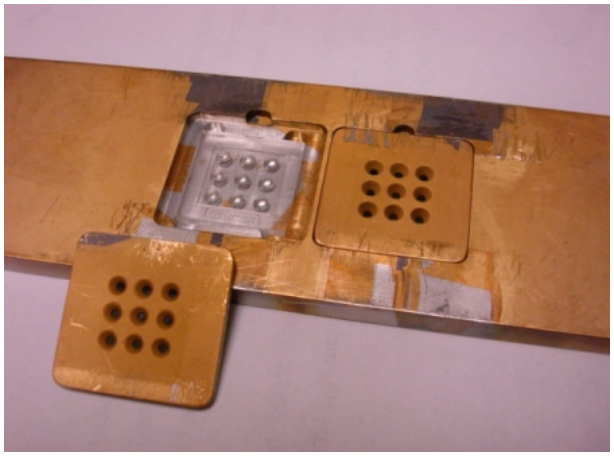

Figure 4.4: Detail of the chip holder and mask for vacuum coating of the parabolic chips

The metal films (use of both silver and gold was investigated in this study) are deposited in the same coating system as described in paragraph 3.2.1. In order to coat the planar tops of the parabolic elements only, a special substrate holder as shown in fig. 4.4 was designed. Here, the clean chip is inserted into a slot in the baseplate and covered with a mask containing a 3×3 array of holes, with the hole pitch the same as the pitch of the centers of the parabolic elements. The holes taper from 3mm to 1.5mm to prevent shadowing due to oblique vapour incidence. Two chips can be coated in one cycle.
Due to the chamber layout and dimensions, variations in the thickness profiles of the films must be taken into account. The further from the axial point at the sample plane (see fig. 4.5) the thinner the film will be. Assuming evaporation from a point source, the thickness d at the distance l from the axial point can be expressed as [16]

$$d = d_0 \left[1 + \left(\frac{l}{h} \right)^2 \right]^{-\frac{3}{2}} \tag{4.1}$$

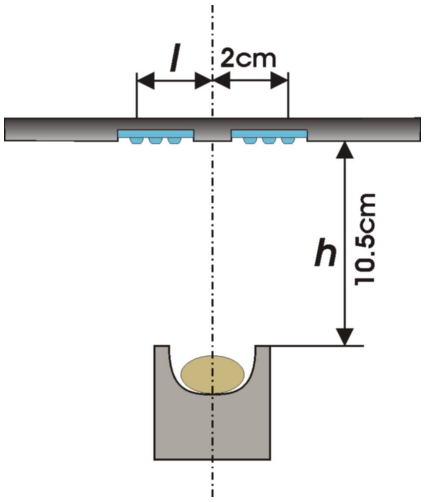

Figure 4.5: Chip coating geometry: crucible-chip holder distance $h = 10.5$cm, the distance of the axial point to the nearest and furthermost parabolic element is $l_{min} = 0.8$cm and $l_{max} = 2$cm, respectively

where d_0 denotes the film thickness at the axial point and h the source-sample holder axial distance.

After the base pressure dropped below 5×10^{-7} mbar, the substrate holder was allowed to preheat above 35°C. Gentle preheating was found to yield better resistance of the coatings to the subsequent cleaning step. The temperature of the substrate holder after the deposition did not exceed 50°C. First, a 3.5nm thin adhesion-promoting chromium film was deposited at the rate 0.1nm.sec^{-1}, followed by growth of a metal film (silver or gold, both 99.99% purity). Gold was coated with nominal thickness 47nm and silver with thickness of 50nm, both at the rate of 0.2nm.sec^{-1}. With respect to the coating geometry described above the thickness range calculated from eq. (4.1) varied between 44.5 and 46.6nm for the gold film and 47.5nm and 49.5nm for the silver film. As mentioned in section 3.4, these small variations in the film thickness have only a negligible effect on the fluorescence emission. The process pressure did not exceed 7×10^{-6} mbar. After the deposition step, chips were left in high vacuum for at least 45 minutes to cool down below 30°C. The bell jar was then filled with dry N_2, vented, and coated chips taken out and used immediately or stored in a desiccator and used later.

4.3.2.2 Layer-by-layer technique

A polyelectrolyte layer deposited by the LbL technique was chosen as the spacer layer instead of an oxide material which was used in previous experiments (section 3.2.1). The LbL technique enables the formation of ultrathin layers on substrates with nanometer precision. Polyelectrolyte materials for LbL desposition have been studied extensively [17–20] also for their potential to facilitate protein immobilisation [21–24].

The principle of the LbL technique is based on the properties of charged PEL polymers

which, depending on their chemical structure, can be either negatively or positively charged at a given pH (fig. 4.6). The mechanism for the LbL growth is based on electrostatic

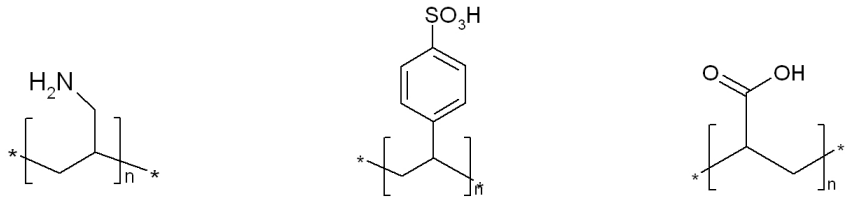

Figure 4.6: Chemical structure of the polyelectrolytes used in this work: (a) poly(allylamine) hydrochloride (PAH), (b) poly(styrene sulfonate) (PSS) and (c) poly(acrylic acid) (PAC). At pH=7, PAH and PAC are positively charged and PSS negatively charged

attraction between positively and negatively charged polymer layers as is shown in fig. 4.7. Prior to the PEL deposition, the substrate charge is rendered opposite to the charge of the first PEL layer (negative in fig. 4.7a). The strong electrostatic interaction between the substrate and the polymer causes a deposition of the polymer with nanometer thickness (fig.4.7b). The substrate is then multiply rinsed with dH_2O in order to remove unbound polymer and immersed into a solution with opposite charge (fig. 4.7c). This leads to deposition of a new layer with nm thickness (fig. 4.7d). This process can be repeated multiple times until the desired multilayer thickness is achieved. Several parameters such as type of PEL, pH and type of salt in the solution influence significantly the process of growth and and allows for its control [17, 25, 26].

Interestingly, it was shown in [24] that the process of growth initiates irrespective of the charge and substrate material type and the properties of the underlying substrate are masked after several PEL layers are deposited.

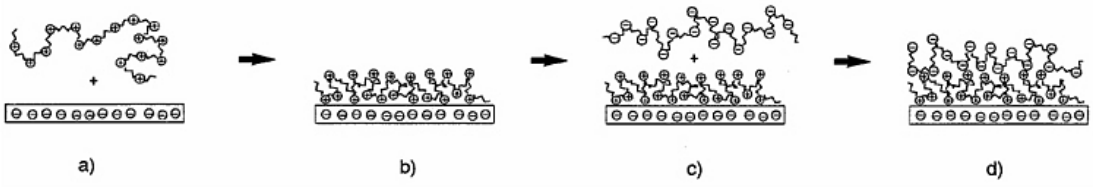

Figure 4.7: Schematics of PEL layer-by-layer growth

In this work, the PEL multilayer serves two purposes: first, as a spacer layer to guarantee a separation between the metal coating and excited fluorophores (prevention of quenching and defining the coupling distance) and second, to provide a chemically functionalised surface facilitating reproducible covalent antibody attachment.

Experimental

To guarantee the utmost reproducibility of the bioassay experiments, gold-coated surfaces were first cleaned by immersion in a 5 : 1 : 1 mixture by volume of dH_2O, 30% H_2O_2 in water and aqueous solution of NH_4OH (both Aldrich) at room temperature for 15 minutes, followed by multiple rinsing in dH_2O and drying by nitrogen. By employing the cleaning step, gold films are left free from adsorbed contaminants (fig. 4.9a). The clean chips were then left in a 5mM solution of MUA (Aldrich) in pure ethanol overnight. The SAM deposited upon the gold surface (fig. 4.9b) serves as a linker between the metal and PEL spacer layer, where the carboxylic termination groups on MUA are rendered negatively-charged by dropping a 0.05M NaOH (adjusted to pH=12) solution onto the paraboloids (fig. 4.9c). The cleaning step was not performed on the silver-coated chips due to the reactivity of silver. Fresh silver-coated chips were just rinsed with pure ethanol, dried and the PEL deposition step proceeded immediately. The issues associated with silver stability are discussed later. The PAH, PSS and PAC solutions were prepared at the concentration 2mg of polymer per ml of solvent. The solvents varied as follows: PAH was dissolved in 0.1M NaCl in dH_2O with pH adjusted to 7.4, PSS dissolved in PBS (pH=7.4) and PAC in 0.1M NaCl in fresh dH_2O (pH$\sim$6.5). Each layer was deposited as described above by immersion in the PEL solution for 10 minutes, followed by washing in three exchanges of deionised water and drying with nitrogen. First, the PAH layer was deposited upon the negatively charged surface, followed by PSS (fig. 4.9d). Five bilayers were desposited in total, four with PAH/PSS composition and in the final fifth bilayer PSS was replaced with PAC to obtain carboxylic termination groups on the surface (fig. 4.9e).

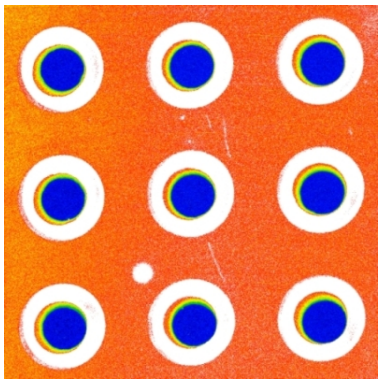

Figure 4.8: Fluorescence scanner image of Cy3-PAH conjugate deposited onto a 5-bilayer PEL stack. The nine blue circles represent fluorescence from the metal-coated areas

In order to check the homogeneity and reproducibility of the PEL coating, two chips were prepared by depositing a Cy3-labelled PAH on top of the fifth, negatively charged layer and scanned with the GMS 418 fluorescence scanner (described in section 3.2.2 on page 47). The scan results showed an element-to-element and chip-to-chip reproducibility in PEL deposition greater then 95%. The image from the fluorescence scanner (displayed in false colour) is shown in fig. 4.8.

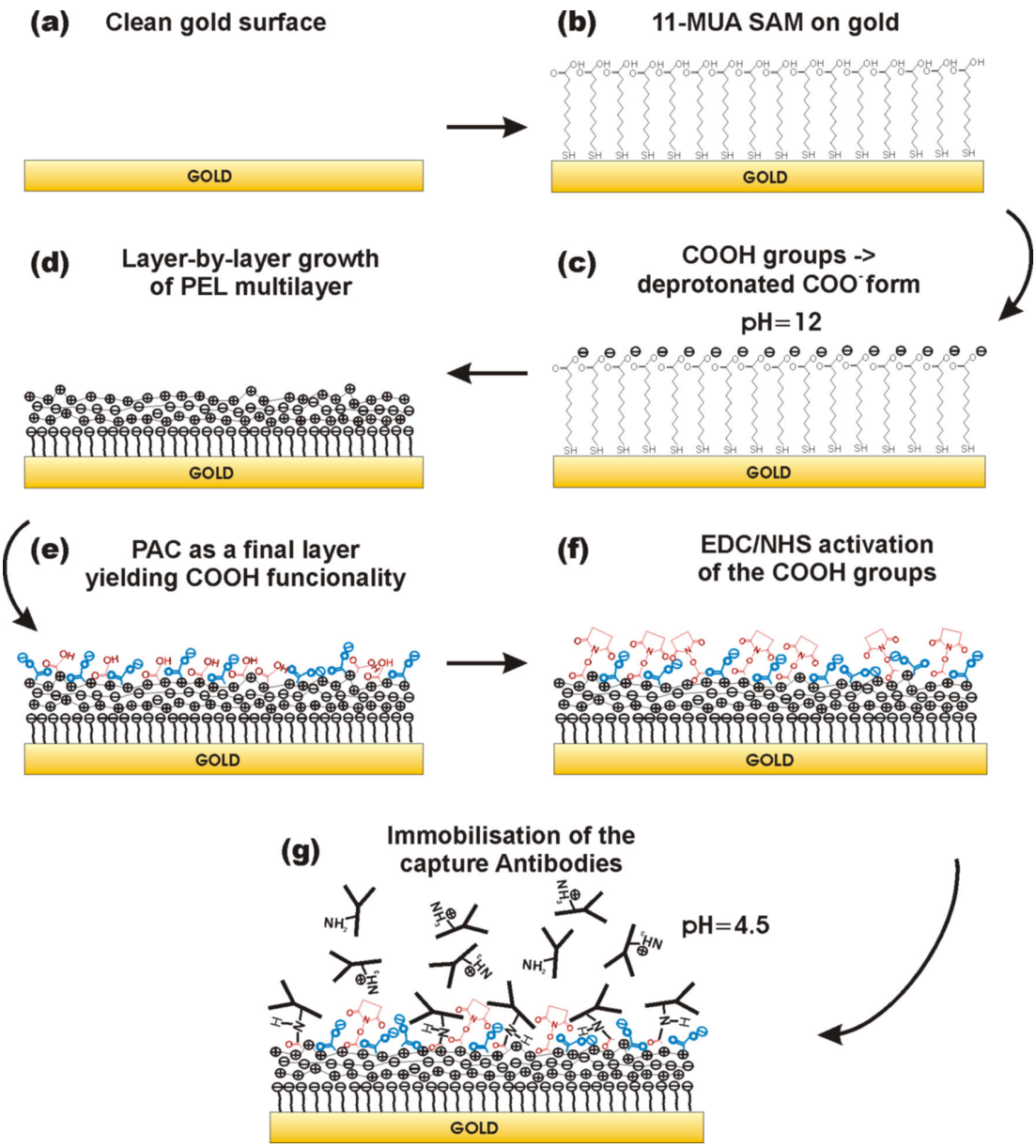

Figure 4.9: Surface modification steps on the gold-coated chips (explanation in text)

PEL multilayer characterisation: ellipsometric measurements

In order to determine the thickness and refractive index of the multilayer, ellipsometric measurements were carried out using the same instrument as in section 3.2.2. Here, 50nm of gold was deposited onto a clean glass slide and onto the back side of the parabolic chip followed by deposition of SAM of MUA on top; these served as substrates for measurements of the PEL growth. Measurements were carried out on each sample, first on the bare Au-MUA surface, and second after 5 PEL bilayers. The wavelength range was 500nm to 800nm with 5nm step and 3×0.5sec integration time at each wavelength. The experimental data are plotted in a form of I_s-I_c graph (explained in section 3.2.2) in fig. 4.10a. The

values of refractive index and thickness were obtained by fitting the ellipsometric data to a three-layer model: (1) known substrate, (2) PEL film of unknown thickness and refractive index and (3) PEL roughness (modelled as PEL/void layer). The refractive index values were determined from the layered structure containing 5 bilayers with results shown in fig. 4.10b. The experimentally obtained values of refractive index served as a basis for system validation described later.

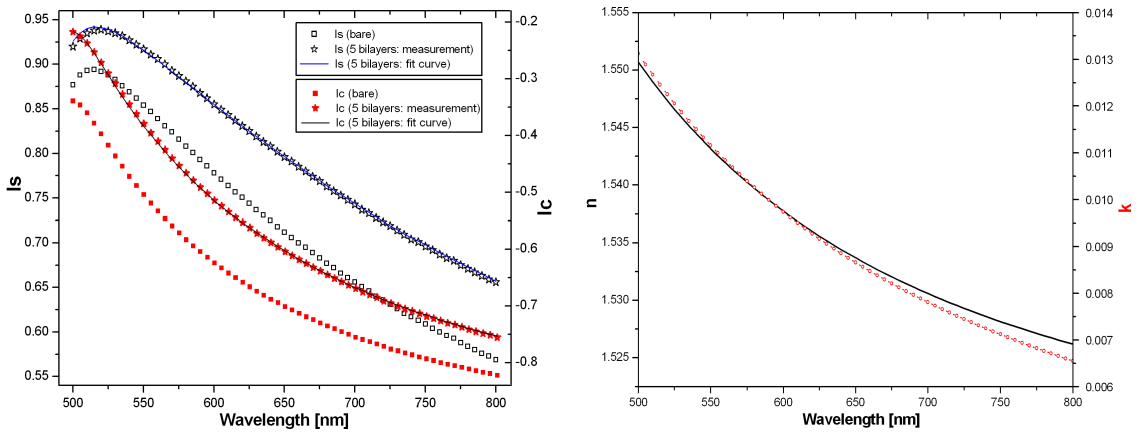

(a) (b)

Figure 4.10: (a) Plot of the measured I_s-I_c data for bare Au-MUA surface and 5 PEL bilayers and the fit curve, (b) Refractive index as a function of wavelength obtained from ellipsometric data

The thickness of the 5-bilayer stack obtained from the model was determined to be 9nm, with surface roughness below 0.5nm. This value is in accordance with thickness of 7.5$\pm$1.5nm obtained by earlier measurements on gold-coated slides with no linker. In the latter case, the increased roughness can be attributed to more pronounced island-like growth of the first PEL layers as a consequence of substrate-independent PEL growth [24].

4.3.3 Choice of materials: practical considerations

The selection of suitable materials is a critical task for the SPCE-based platform to be robust and reliable. Material issues include choice of metal supporting surface plasmon resonance and type and thickness of the dielectric spacer layer deposited upon it. The following requirements must be met:

- the layered structure must be optimised to enhance the surface plasmon resonance field and to maximise plasmon coupled emission within the spectral range of excitation and emission of the fluorophore used
- the range of SPR and SPCE angles must be compatible with the chip design

- the surface must facilitate reproducible immobilisation of biomolecules
- the layered structure is capable of withstanding all preparation steps without deterioration

Although SPR and SPCE have been reported for a range of metals (section 2.2 and 2.4), the use of fluorophores emitting in the red to mid-IR range restricts our selection to Ag and Au as they best support surface plasmons in this spectral range. Gold as a widely used metal shows lower field enhancement and the SP field is spatially more confined then in silver. However it is convenient for its superior chemical stability to silver. The use of both materials is investigated here.

The dielectric spacer serves two main roles: to define spacing between the metal film and fluorophore (to avoid quenching and to set the coupling distance for surface-bound flurophores) and to provide a support for reproducible immobilisation of bioreceptors. However no exact determination of the optimum spacer thickness has been carried out, it is expected that it can lie in the interval 20nm to 40nm. Since the SPR excitaion - SPCE detection scheme is employed, this estimation is taken as a trade-off between the maximum SPR field intensity (which is highest directly at the metal-water interface) and the optimum SPCE coupling distance (fluorescence from molecules located directly at the metal-water interface is quenched). With regard to earlier experiments (section 3.2.1) the use of a thin silica layer was first investigated. It was found, however, that poor adhesion to both silver and gold leads to its deterioration after prolonged exposure to aqueous solution and its use was therefore discontinued. Polyelectrolytes as described in section 4.3.2 were found to be suitable spacer layer materials for their robustness, ease of preparation, fine tunability of thickness and selection of surface functionalities. Another option is to immobilise receptor molecules directly onto the metal film via SAM of alkanethiols where the biomolecules themselves serve as a spacer layer.

4.3.3.1 Compatibility with the chip design

As shown in section 2.2.2 the angular spectrum of SPR/SPCE depends strongly on the layer composition. The SPR reflection minimum and SPCE peak occur at larger angles for gold than for silver. Any dielectric layer on top the metal causes a shift towards larger SPR/SPCE angles. Since the chip is designed to capture angles between 62° and 80° the amount of allowable shift must be determined in terms of the maximum thickness of the dielectric layer covering the metal film. The biomolecules immobilised upon the spacer layer contribute to its total thickness. In order to estimate the maximum spacer thickness SPR

and SPCE curves were obtained for both silver and gold films using mathematical models. The SPR reflection curves were calculated using the freely-available program WinSpall©. The model for calculating the SPCE curves is based on the theory described in section 2.3.2.

In the model procedure the following assumptions have been made. Metal layers (silver and gold) are 50nm thick plus 2nm Cr underneath as an adhesion layer. Total thickness of the dielecric layer on the metal film is the sum of the thicknesses of the spacer layer (∼10nm; experimentally determined) and the stack of biomolecules (thickness depends on the assay format). This layer is assumed to be smooth and represented by a single value of dielectric constant. Fluorophores (Cy5 or AlexaFluor 647) are placed on top of the dielectric film with isotropic orientation. In the model the excitation wavelength is 635nm, emission wavelength 670nm and the dielectric layer is characterised by values of n and k obtained from graph 4.10b at the respective wavelength. As presented in section 4.6.2 a

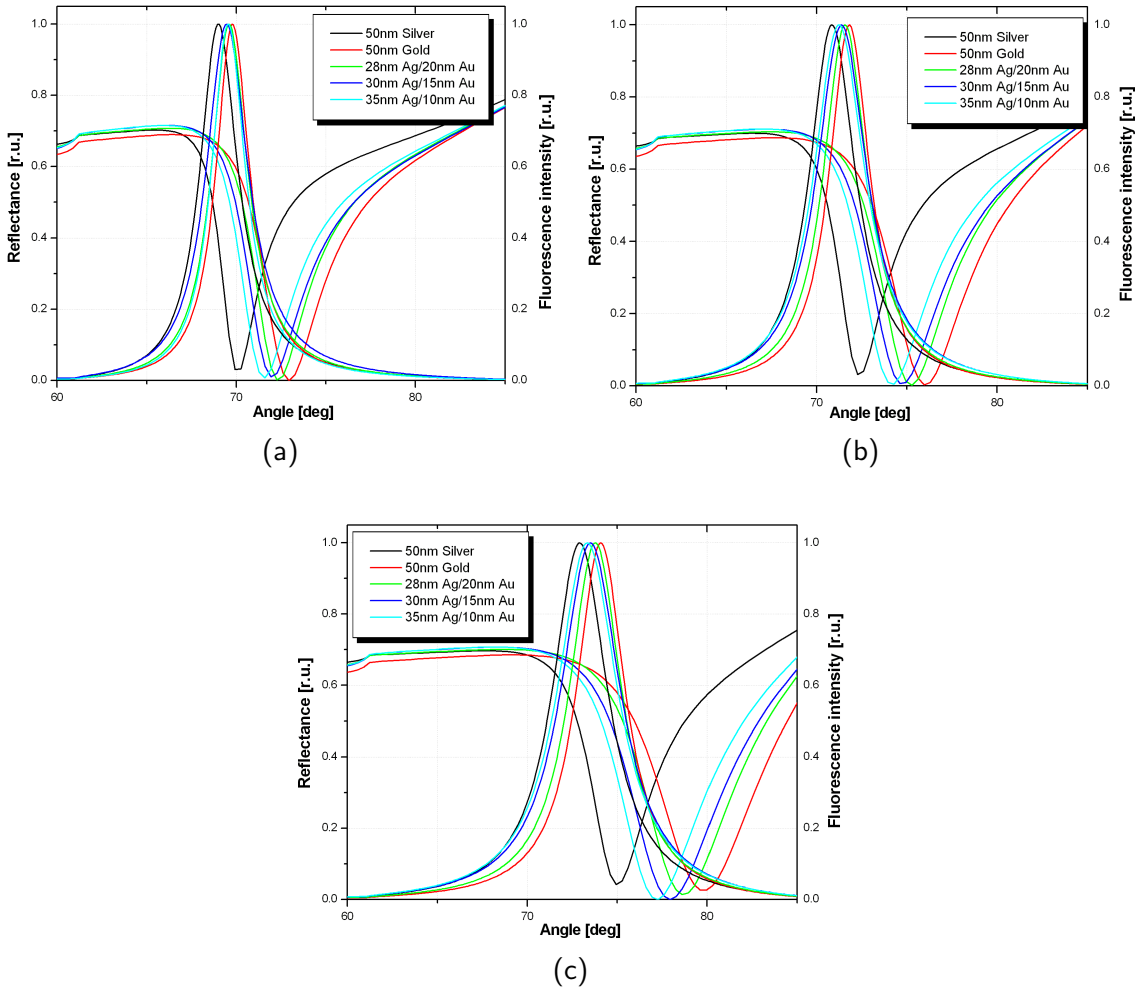

Figure 4.11: Dependence of SPR reflection minimum and SPCE peak angle on total thickness of dielectric layer deposited on top the metal film. Thickness (a) 10nm, (b) 20nm and (c) 30nm

human IgG sandwich assay is the subject of this study. Human IgG is a Y-shaped molecule with the following dimensions [28]: height=14.5nm, width=8.5nm and thickness=4.0nm. Surface-bound antibodies are most likely to be lying flat on the surface, in their energetically most favourable state [29]. This is valid for both physisorbed and covalently immobilised molecules. Orientation of the subsequently attached antigen and the labelled secondary antibody can be arbitrary. The total thickess of the dielectric layer thus ranges between 14nm (all proteins lying flat on the surface) and 42nm (both antigen and the labelled antibody standing upright), however the latter is very unlikely. It can therefore be well assumed that the average thickness of the dielectric layer will be well below the maximum, and range between 20nm and 30nm.

The model curves for various thicknesses of the dielectric layer are shown in fig. 4.11. Various compositions of the metal film have also been considered; pure silver and gold and also silver/gold bilayer (with gold on top) with varying thickness ratio. The combination of thicknesses (45-50nm) was chosen so that the value of reflectivity at the SPR angle is minimised. The advantage of using Ag/Au bilayer is that it combines the favourable properties of both metals, i.e. narrower peaks and larger field enhancements of silver and superior stability of gold [30, 31]. As can be seen in the graphs, the combination of pure gold film with the 30nm thick dielectric layer defines a limit for the SPR angle given by the chip design. As the content of gold in the composite film decreases, so does the value of the SPR reflection minimum. For our measurements, the cut-off thickness of the dielectric layer is therefore well compatible with the thickness estimation of the combined PEL and biomolecule stack layer.

4.3.3.2 Stability of the coatings

Stability of the metal/dielectric coatings on the polymer chip substrate represents another major requirement for a bioassay application. Any damage (mechanical, optical) of the layers during an arbitrary process step would lead to deviation of its properties or a complete loss of functionality. Here, the stability of metal film deposited onto the polymer substrate is the main issue. As the substrate temperature is one of the critical factors for achieving good adhesion of vapor-deposited films to the substrate, there is an issue with the polymer substrate, where temperature can only be slightly elevated above ambient to avoid thermal damage.

For application in the SPCE biochip, silver was first considered for its larger field enhancement and lower SPR/SPCE angles. Deterioration of silver films leading to their cracking

and peeling (visible even by eye) occurred after a few immersions in polyelectrolyte solutions. The fact that not all coatings were damaged led us to carry out a more systematic investigation. The effect of deposition temperature and the presence of an alkanethiol linker were assessed in a comparison of surface quality prior to and after PEL deposition.

Surface images were obtained by measurements on a white light interferometer (Wyko NT1100, Veeco Instruments). With this technique, the height profile of a surface area is obtained from an interferogram of a reference beam and that reflected by the measured surface. All measurements were done in a phase-shift interferometry (PSI) mode. Here, the phase of the reference beam is modulated by a piezoelectric element and the resultant phase map of the interferogram translated into path difference and ultimately into a height map. It offers vertical resolution below 1nm and lateral resolution given by the size of the camera pixel and magnification of the objective used.

Firstly, two sets of piranha acid-cleaned glass slides were coated with 2-3nm Cr followed by 50nm Ag. In the first set, substrates were preheated above 100°C, in the second the substrate temperature just slightly exceeded ambient (30-40°C). Glass was chosen for the temperature test over the chips as they showed signs of distortion due to direct heating. Pressures and deposition rates varied slightly from coating-to-coating. The silver films on preheated substrates withstood the PEL deposition without an increase of surface roughness while those grown on the cold substrates showed signs of cracking and peeling, but not over the entire coated area. The same results were observed with 'cold' slides just plasma-treated prior to deposition and when a mercaptopropionic acid (MPA) linker between metal and PEL was used.

When the tests were repeated on the chips, the metal films were coated at the temperature of the substrate holder (fig. 4.4) not exceeding 55°C with pressures and deposition rates close to those used for coating the glass substrates. The chromium film was also used. A reference image of the top plane of the parabolic chip is shown in fig. 4.12a. The concentric peak-trough structure originates from the mould fabrication. With typical peak-trough vertical distance $\sim$10nm and lateral distance $\sim 6\mu$m the aspect ratio above 500:1 yields smooth surface. The same image was obtained by independent atomic force mictroscopy measurement. Deposition of neither the metal film nor subsequent alkanethiol SAM does not cause an increase in surface roughness as illustrated in fig. 4.12b. Serious damage to the silver films occurs after eight immersions in PAH and PSS solution (details of PEL solution preparation in section 4.3.2 on page 71). This is accompanied by a significant rise of surface inhomogenity and roughness as shown in fig. 4.12c. The same type of the

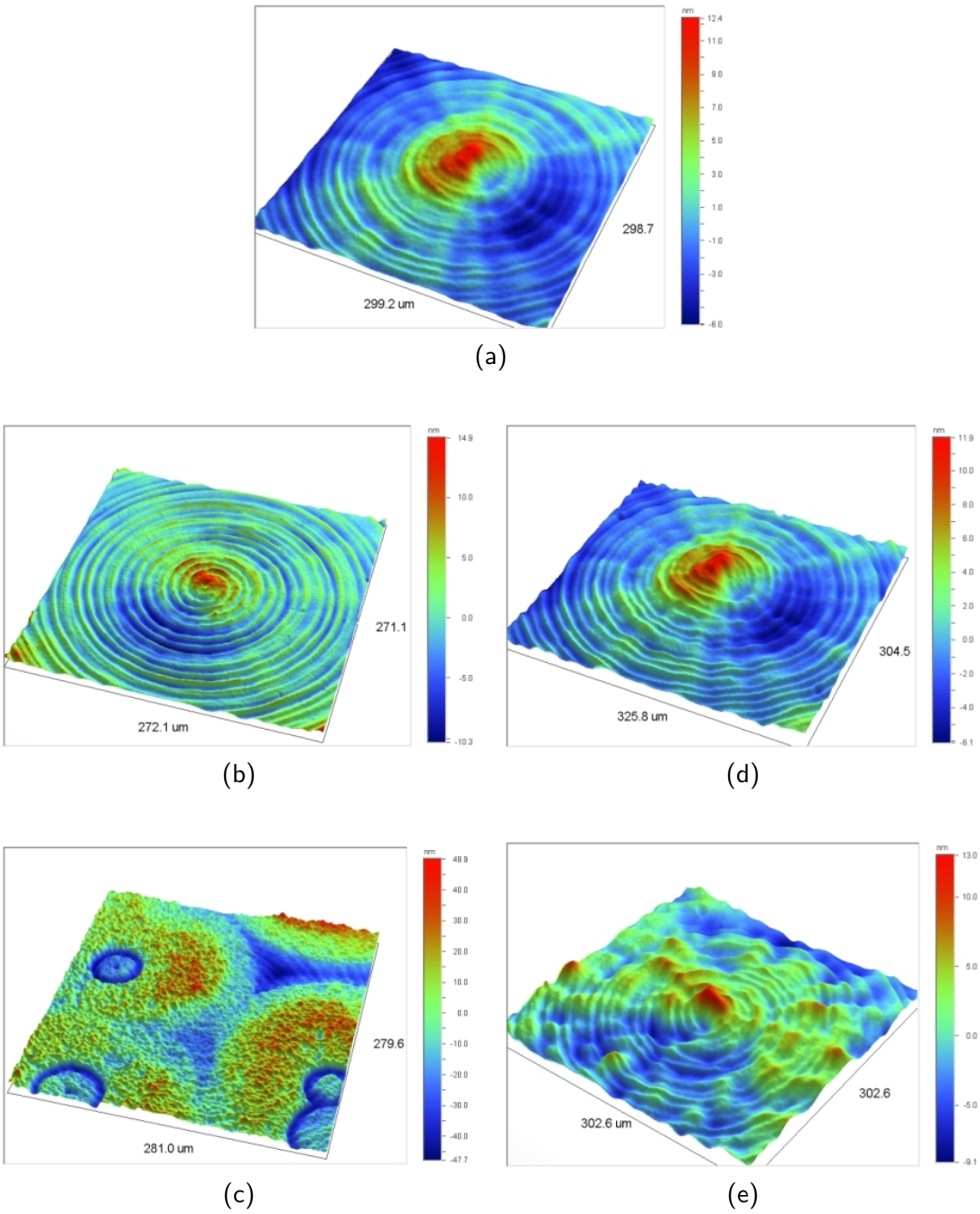

Figure 4.12: Images of chip surface topography obtained by white light interferometry measurements. (a) clean chip, (b) 50nm silver with alkanethiol SAM, (c) Ag-alkanethiol linker surface after four immersions in PAH/PSS solution, (d) 45nm gold with MUA SAM, (e) Au-MUA surface after completion of the PEL deposition process

silver film damage was observed when a chip was immersed in pure PBS solution. This would lead to the conclusion that it is saline solution rather then PEL material that causes the damage. Application of short-chain (mercaptopropionic acid) or long-chain (mercapto-hexanedecanoic acid) alkanethiol linker did not prevent the silver damage. However, not all silver-coated chips were damaged (the binding kinetics experiment described in section

4.7 was carried out on silver-coated chips). But the lack of reproducibility in preparation of stable silver films caused us to switch to gold films which exhibited superior stability in the PEL solutions (figs. 4.12d and 4.12e).
This test was also carried out on a Ag/Au bilayer (30nm Ag overcoated with 15nm Au) deposited onto a chip with no deterioation of the multilayer observed.

4.4 Chip reader: design, validation and practical limitations

As discussed in the previous section, fluorescence emitted above the critical angle of the interface can be easily redirected by means of a solid parabolic element, producing a (nearly) collimated beam. The fabrication tolerance together with material properties of Zeonex, however, caused a deviation from the originally required chip dimensions. As a consequence of a slight shift of the focus of a single paraboloid below the secant plane forming the recognition area, the fluorescence emitted into the chip substrate does not follow a parallel path. Divergence of the fluorescence beam has therefore an impact on the design of the chip reader, and the distances and dimensions of the optical components used need to be assessed carefully in order to minimise losses on the outer parabolic elements due to the insufficiently large aperture of the imaging system.
In this section, the chip reader and its assembly and alignment are first described along with the fabrication of the annular mask. Choice of the optical components is justified by raytracing analysis performed for both SAF- and SPCE-based schemes.

4.4.1 Description of the instrument

4.4.1.1 Assembly and alignment

The instrument is assembled on an optical board making use of a four-rod mount system (Thorlabs, USA). Apart from offering great flexibility in component positioning, this setup provides inherent alignment along a common optical axis.
A schematic diagram of the instrument is shown in fig. 4.13. The same laser source as that described in section 3.2.3, operated at 7mW of the output optical power, was employed in the chip reader. The divergent laser beam is collimated with an achromatic doublet lens with f=75mm and diameter 25mm (Edmund Optics, UK) and passed through an excitation filter (FF01 630/20, Semrock, USA; spectral transmittance plotted in blue line in fig. 4.14)

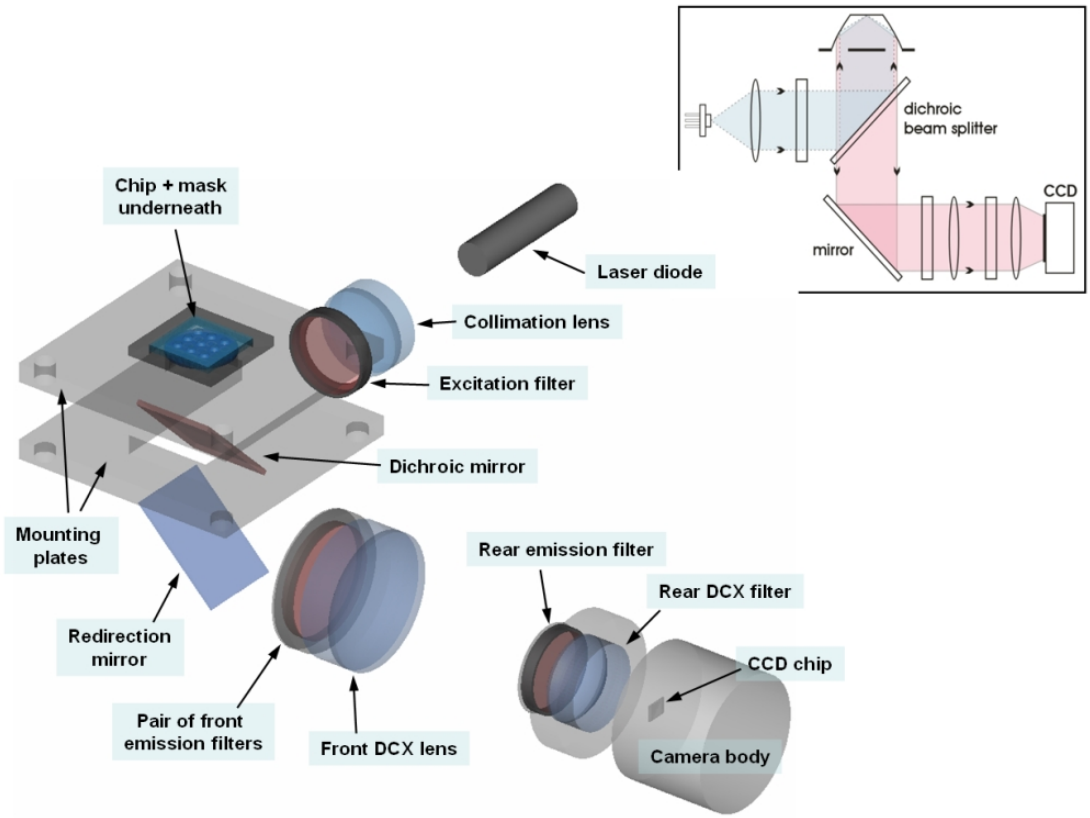

Figure 4.13: Layout of the optical elements in the chip reader. Mounting plates in the imaging arm have been omitted for clarity. The planview is displayed in the inset

with a 23mm clear aperture. The collimated beam is redirected onto the mask and biochip with a dichroic mirror (FF650 Di01, 25×36mm, Semrock; green line in fig. 4.14), which makes an angle of 45° with the incident beam. The annular mask is fixed in a slot, and the chip is placed directly upon it. No optical matching of the chip and the mask is used.

The fluorescence emitted from a surface into the biochip is redirected by the redirection mirror (25×35mm, Edmund Optics), which is adjustable in position and angle, passed through a set of three emission filters (2× FF01 692/40, Semrock and 1× HQ700/75m, Chroma, USA; transmittance of a single filter plotted in the red line in fig. 4.14, total transmittance over 85%) and imaged onto a CCD chip with active size 6.3×4.8mm (752×580 pixels) of a 16-bit camera (SXVF-MX7, Starlight Xpress, UK). The camera communicates with the computer via a USB interface.

From the knowledge of the required magnification of the imaging system (since the size of the fluorescent ring and its angular emission spectrum as well as the dimensions of the CCD chip are known) the distance margins and minimum dimensions of the optical components are determined by raytracing simulations, presented in section 4.4.2. The imaging optics comprises two double-convex (DCX) lenses. The role of the front one (f=80mm,

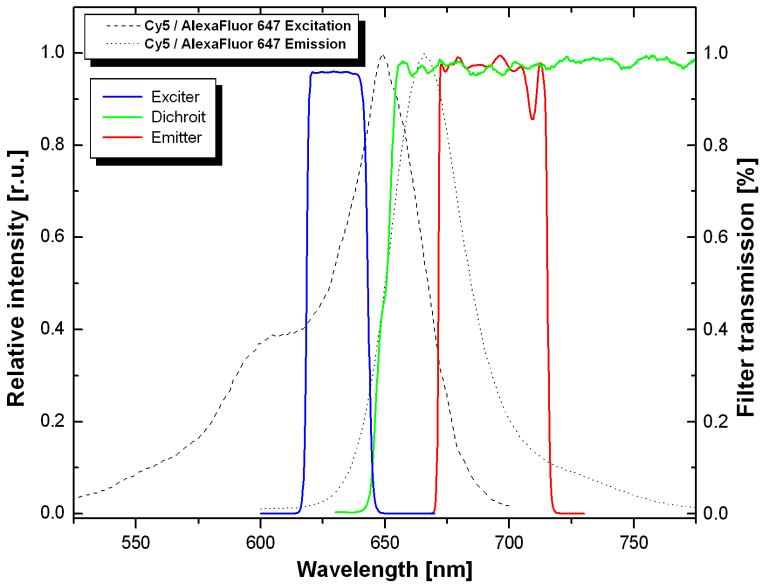

Figure 4.14: Spectral transmittance of the used filter set. The filters are compatible with Cy5 and AlexaFluor 647 dyes. Their excitation and emission spectra of the dyes (in solution) are also illustrated

diameter 40mm, Edmund Optics) is to render the divergent fluorescence beam convergent and the rear lens (f=30mm, diameter 25mm, Edmund Optics) creates a sharp image of the fluorescence pattern at its focal plane, which is coincident with the plane of the CCD chip. A 33mm clear aperture of the first emission filter, placed directly in front of the front lens, defines the maximum angle of acceptance of the imaging system. In order to capture the entire fluorescence beam, the distance of the chip to the front emission filter should not exceed 100mm. However, the limitation imposed by the physical dimensions of the mounting plates and mirrors means that this distance is exceeded by a several mm, which leads to a fractional loss of signal from the outer elements (see table 4.2). The distance of the front lens to the rear emission filter (clear aperture 23mm) is set to cover the whole convergent beam. Insertion of the rear emission filter has no impact on the image quality, but helps to improve signal to noise ratio. Fig. 4.15 shows an image of the instrument.

Alignment

As described above, the system comprises two main paths, excitation and emission. The emission path is aligned first followed by the excitation one. The position and angle of the redirection mirror is adjusted first with the aid of a collimated laser beam placed above the slot containing the annular mask until the central ring of the mask coincides with the centre of the mirror and the reflected pattern is parallel to the optical table. The camera, mounted on an XYZ table, can be translated independently in all three directions to guarantee that

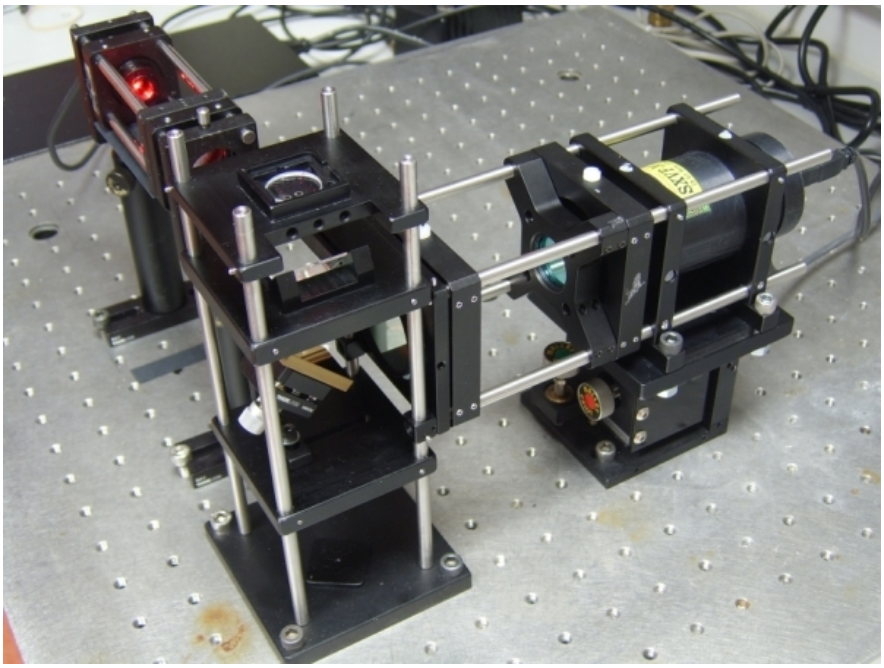

Figure 4.15: Image of the chip reader

the central ring of the mask coincides with the centre of the CCD chip. Due to the choice of the type of mounting, the optical axis of the imaging optics coincides with the centre of the chip. Any misalignment of the imaging path with respect to the centre of the chip will therefore result in distortion of an image on the CCD chip due to off-axis incidence and loss of signal from the outer elements through vignetting. The dichroic mirror and chip mount plates are then fixed onto the vertical rods.

Finally, the laser, collimation lens and excitation filter, forming an independent, self-aligned block, is mounted separately onto the optical table and adjusted so that the laser beam reflected from the dichroic mirror makes normal incidence upon the mask and chip.

4.4.1.2 Mask fabrication

The array of annular apertures is fabricated by means of photolitographic patterning of an opaque aluminium film deposited onto a circular optical window (Edmund Optics). The window with diameter 20mm and thickness 2mm is made of BK7 glass and has antireflection coatings on both faces. An opaque (>100nm) aluminium film was vacuum-coated onto one face. Aluminium was chosen because it can be etched easily and has a high adhesion to the glass surface. To facilitate the aluminium patterning, 0.5ml of negative photoresist (MicroResist ma-N 420, peak absorption λ=365nm) was dispensed onto the Al-coated side of the window, spin-coated for 35sec at 3000rpm and prebaked for 65sec at 100°C.

Patterning of the photoresist was carried out by a MA56 mask aligner (Karl Süss, Germany).

As a master, a negative of the mask, printed in high quality onto a thicker acetate sheet (JD Photo, UK) in a 1:1 scale and attached to a glass plate, is used. Four crossed lines located at the circumference of the mask facilitate precise alignment of the master against the window (fig. 4.3). The substrate was exposed for 85sec, which is a sufficient time for the exposed photoresist to undergo complete photopolymerisation.

The unexposed resist was removed by immersion in developer solution (MicroResist ma-D 332 S) for 2 minutes, thoroughly rinsed and dried. Exposed photoresist was then hardened by post-baking at 100°C for 125sec and the window was allowed to cool down to room temperature prior to the etching step. Etching of the Al pattern was carried out in a mixture of phosphoric acid, deionised water, acetic acid and nitric acid in the ratio of constituents 16:2:1:1., prepared at room temperature. The etching process was controlled visually and was aborted immediately as soon as the mask pattern was completely etched. The excess etchant was removed by thorough rinsing with dH_2O. Finally, the exposed resist was washed off with acetone, the mask rinsed with isopropanol and water and blown dry.

4.4.1.3 Fluorescence image capture and analysis

The camera communication and control functions are embedded into the custom-written graphical user interface (fig. 4.16). Apart from the control of the camera integration time, the software also features a recurrent image capture function, used in the binding kinetics experiments.

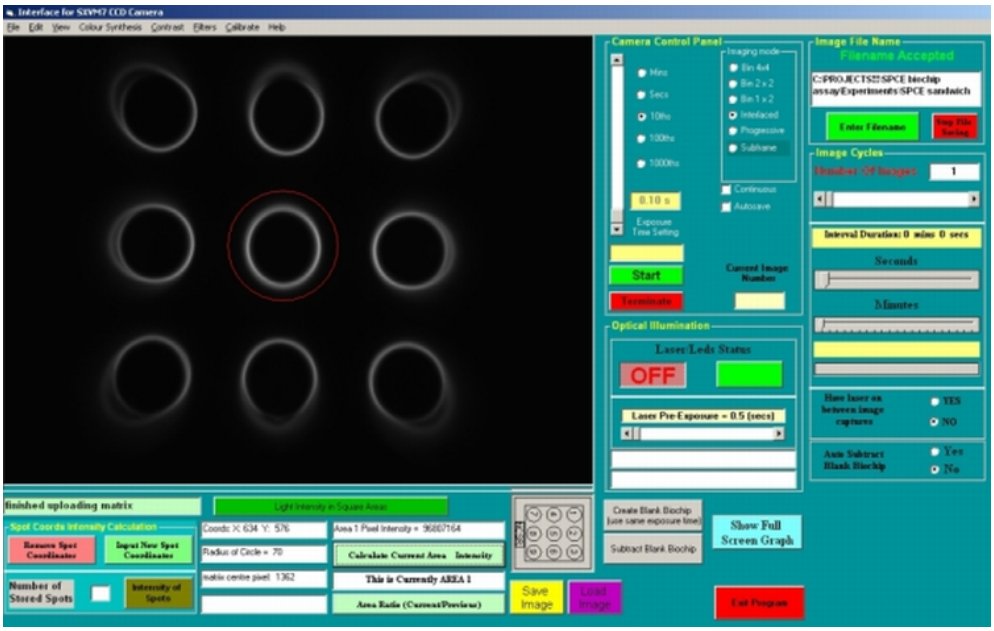

Figure 4.16: Graphical user interface of the image capture and analysis software

The captured fluorescence image is saved into both bitmap image file and a bitmap matrix,

which stores an intensity map of the captured image. To obtain an intensity of each fluorescence ring, a circular area with a known diameter around the ring is defined (illustrated by the red circle in fig. 4.16) displaying the total fluorescence signal within. This extraction is performed manually for each fluorescence ring.

It is important to mention that the issue of spatial intensity profile of the collimated laser beam (approximately Gaussian since the laser produces a single transverse mode) was also addressed. Element-to-element variation of the illumination intensity would reflect in element-to-element fluorescence intensity variation unless compensated by an appropriate weighting factor. How critical this issue is in the set of experiments presented in this thesis was checked by preparing two chips (with and without metal coating) with immobilised labelled antibodies on top. Element-to-element inhomogeneity in Ab coating was first checked with a fluorescence scanner. SAF and SPCE measurements were carried out next, with the intensity of the captured fluorescence rings weighed by factors obtained from the scanner measurement. The distortion of the outer rings, caused by the properties of the imaging optics, does not lead to a loss of signal. In both cases it was found that the amount of fluorescence from the central element exceeded that from the rest of elements, where the element-to-element fluorescence intensity variations, imposed by the inhomogenous illumination, were non-significant. Since the central element in all assay experiments presented in section 4.6 served as a control, no weighting was required in the analysis of the fluorescence signal.

4.4.2 Validation of the chip reader design: raytracing simulations

Raytracing provided a useful tool for validation of the chosen chip reader design and specification of what optical components would be the most suitable to use. To carry out the analysis, commercial software *TracePro v. 3.1.0* (Lambda Research) was used. System analysis is performed by emitting a finite number of rays from a predefined grid with an option of setting their direction, divergence and polarisation. In this mode rays from a single source can only be emitted. Alternatively, a custom-defined grid of (multiple) sources can be created, each source emitting a predefined number of rays into predefined directions and with predefined intensities. In the case of the chip, where fluorescence from a surface is emitted into a known angular range from all nine elements simultaneously, the latter approach was employed.

Validation of the chip reader design was carried out in several steps. First, to determine the

exact position of the paraboloid foci and hence the dimensions of the ring of illumination and, second, to evaluate the system performance when fluorescence with a known angular range is emitted from such an area.

4.4.2.1 Illumination

To model the excitation beam, parallel rays are emitted from random locations across a mask-wide circular grid (fig. 4.17a). Those rays, which are not blocked by the annular mask, undergo total internal reflection at the side faces of the paraboloids, from where they are reflected into the focus and pass beyond to an interface. The focus is shifted 9μm below the top plane of a single truncated paraboloid. Due to the cylindrical symmetry of a paraboloid the illuminated area has thus the shape of an annular ring with inner radius 17μm and outer radius 90μm (fig. 4.17b). As the angular range remains unmodified by a shift of the focal plane, the fluorophores lying within the ring of illumination are excited by an evanescent field induced by light incident above the critical angle (TIRF scheme). Any deviation from good collimation of the laser beam would cause further stretching of this ring of illumination.

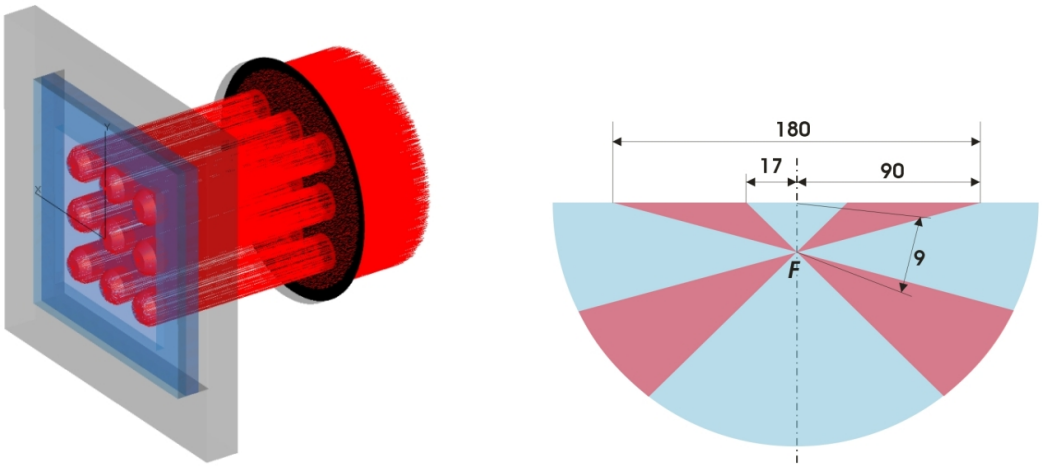

(a) (b)

Figure 4.17: (a) Focusing of a collimated laser beam with elements of the parabolic biochip, (b) cross-section of the excitation beam (red) in a single paraboloid near its focus. Dimensions are in μm

4.4.2.2 Emission: source grid and ray directions

A fluorescent, (diffraction-limited) point source lying at the interface will emit fluorescence into a cone of light with the range of angles determined by properties of the layered structure. A spatially extended source can be regarded as an infinite sum of point sources (but emitting

finite fluorescent energy). Because only a finite number of rays can be traced, it is therefore necessary to define a finite number of (point) sources within the ring of illumination which would fully represent the area from which fluorescence can be emitted, irrespective of the fluorophore density distribution inside. Such a grid is illustrated in fig. 4.18a. Point sources (twelve in total), denoted with full dots in the figure, located along the inner and outer circumference, were found to satisfactorily mimic the full ring of illumination. It was proved by random insertion of additional point sources into the existing grid that adding extra points will not bring any new information about the instrument performance.

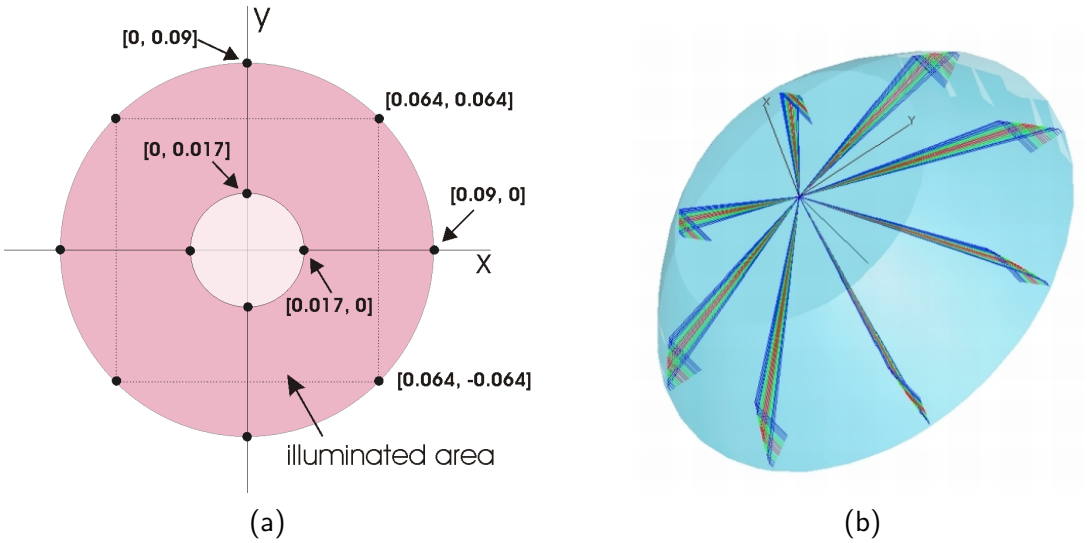

Figure 4.18: (a) Definition of the grid for raytracing. Rays are emitted from the points (full dots) placed within the annular ring of illumination. Point source coordinates are in mm. (b) Directions of rays emerging from a single point on the grid. To mimic fully 3D nature of fluorescence emission, rays are sent along x and y axes as well as along the axes of the quadrants

The 3D nature of fluorescence emission from a point source at a surface can be mimicked by choice of ray directions illustrated in fig. 4.18b. As shown in the figure, rays from every point on the grid are sent along the directions of the x and y axes as well as along the axes of the four quadrants defined by the major axes. The angular range of emitted rays is obviously the same in each direction. The choice of sampling distance (and therefore number of traced rays) depends on the type of fluorescence emission pattern. This is going to be fully addressed in the next section.

Although this analysis, due to simplification of the model compared to the real situation, gives only approximate information about the image pattern at the CCD chip, the modelling played an important role in the instrument design and characterisation.

4.4.2.3 SPCE and SAF emission: raytracing results

Rays were traced through the system for both SPCE- and SAF-based sensing configurations. In the case of SPCE, where the ADE is strongly dependent on the thickness of the dielectric layer upon the metal film, experimental conditions as used in the bioassay experiments described in sections 4.3.2 and 4.3.3 were modelled: ∼45nm gold film is coated with ∼25nm thick dielectric layer (combined spacer layer and a stack of proteins) with effective refractive index 1.53 at λ=670nm (fig. 4.10), followed by a fluorescent layer. The peak emission occurs at 73° (fig. 4.19a). Tracing of the SAF emission pattern (fig. 4.19b) was performed for the supercritical as well as the subcritical range. The latter was carried out to investigate whether the annular mask is capable of blocking the light emitted into subcritical angles from the entire ring of illumination.

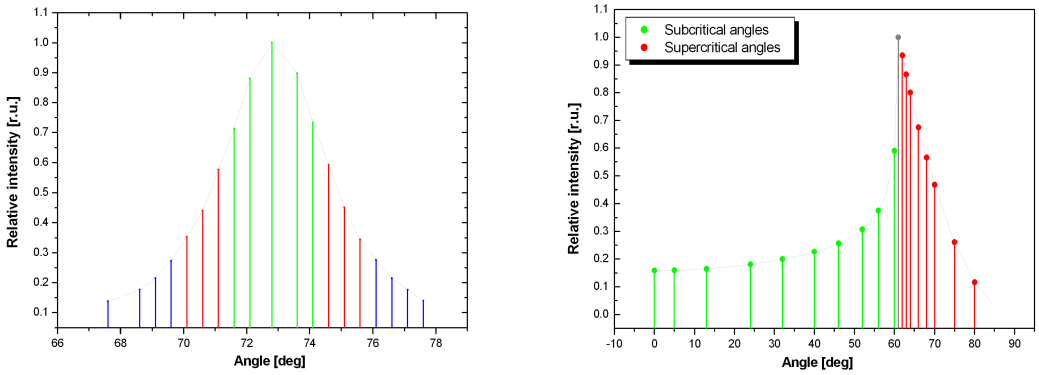

(a) (b)

Figure 4.19: (a) Selection of rays for tracing from the model SPCE envelope. (b) Selection of rays for tracing from the SAF envelope (random orientation of molecules is assumed). Separate tracings are performed for both subcritical and supercritical range of angles

In order to trace optical losses in the system, the ray flux was monitored at several surfaces along the path for both sensing configurations. Each emitted ray from the grid (fig. 4.18) is assigned a value of emitted power normalised to unity (y axis in fig 4.19). The total power emitted from a single paraboloid grid calculated as a sum of the powers of all rays is normalised to unity and taken as a reference to express fractions of power incident onto the monitored surfaces. For SPCE, the light with relative intensity below 0.1 of maximum was cut-off, SAF was traced within the range of the chip-mask acceptance angles (62° - 80°, highlighted in red in fig. 4.19b), thus omitting the ray at 61° (greyed out in fig. 4.19b). Different relative positions of the parabolic elements with respect to the optical axis will result in differences in losses. Because of the cylindrical symmetry of the chip and all of the optical elements with respect to the optical axis, the central and

arbitrary 'axial' and diagonal parabolic element (fig. 4.20) fully characterise the whole chip. In the analysis, transmittances of the filters are taken into account (four filters with 95% transmission at 670nm) and the reflectivity of the redirection mirror is assumed to be unity. Results of the analysis are summarised in table 4.2. In the case of SPCE all emitted rays are reflected by the paraboloid reflective face and the losses can be attributed solely to reflection losses at the interfaces due to oblique incidence and absorption in the chip itself (note minimum loss between the source and the parabola face in table 4.2). Significantly more power is lost in the SAF scheme where, as the analysis shows, a significant fraction of rays is captured within the chip. Due to the shift of the top paraboloid plane above the focus, the lowest angles (and incidentally those carrying the highest proportion of power) from the off-axis sources do not undergo the redirection by means of reflection at the paraboloid side face and, as they are emitted at the angles larger than the critical angle of the bottom interface, are therefore captured within the chip. This effect occurs for rays originating from the inner and outer circumference alike, and is gradually more pronounced for rays originating further from the axis of symmetry of the parabolic element. The flux between the front emission filter and the camera chip is reduced equally for all elements and only as a consequence of reflection at the lenses and absorption in the emission filters. Tracing of rays in the subcritical range (highlighed in green in fig. 4.19) showed that none reached the camera chip plane; they were either blocked by the annular mask underneath or reflected outside the aperture of the dichroic mirror.

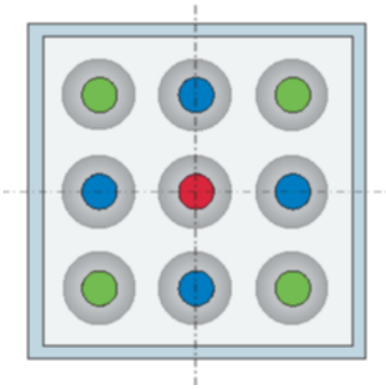

Figure 4.20: Marking of parabolic elements for ray-tracing analysis: central (red), axial (blue) and diagonal (green)

Surface	**SPCE**			**SAF**		
	Central elm.	Axial elm.	Diagonal elm.	Central elm.	Axial elm.	Diagonal elm.
Total flux	1	1	1	1	1	1
Parabola refl. face	0.96	0.96	0.96	0.78	0.78	0.78
Front emiss. filter	0.85	0.85	0.83	0.61	0.61	0.60
CCD chip	0.67	0.67	0.65	0.48	0.48	0.47

Table 4.2: Summary of the flux losses on various elements of the chip reader obtained from ray analysis. Flux at the range of interfaces is expressed as a fraction of the total ray flux emerging from a single paraboloid

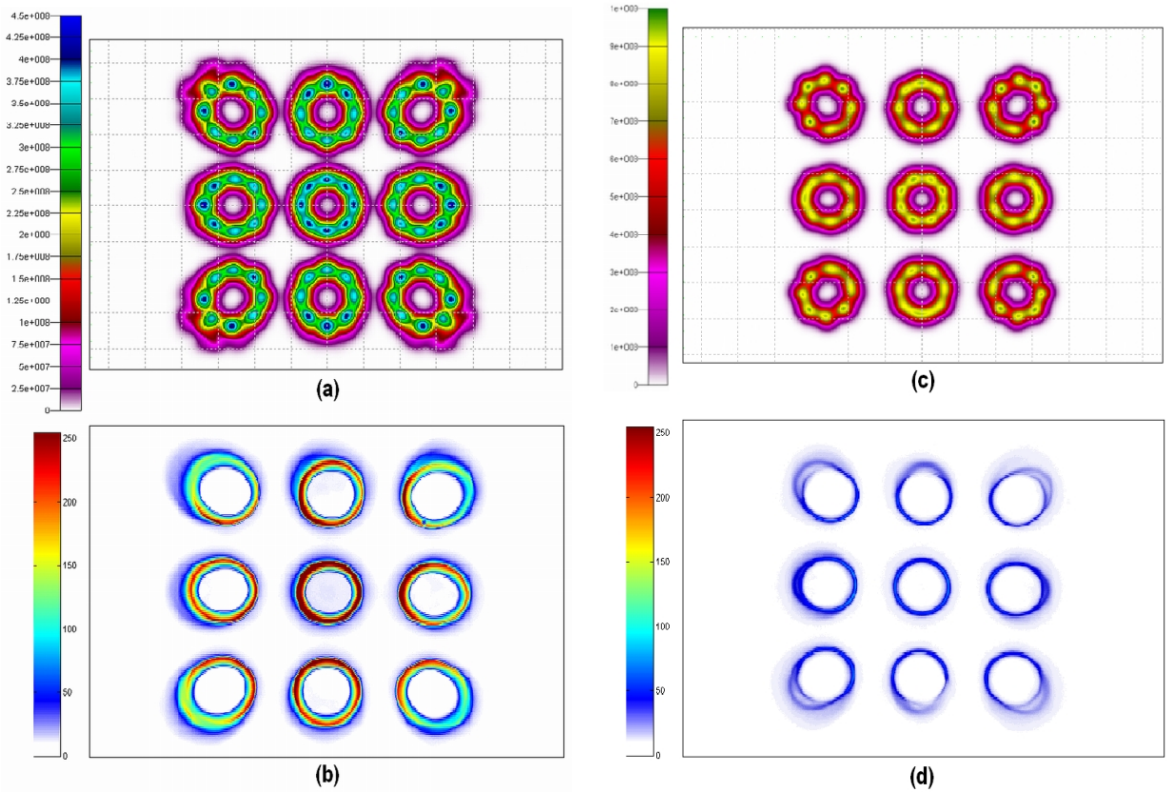

Figure 4.21: Model fluorescence images on the camera chip obtained from the raytracing simulation and actual images from the CCD camera (displayed in false colours): (a) SAF emission (raytracing simulation), (b) SAF emission (camera image), (c) plasmon-coupled emission with a 25nm thick dielectric layer (raytracing simulation) and (d) plasmon-coupled emission (camera image). Full area of the camera chip is displayed for both simulated and captured images

Images of both SPCE and SAF, obtained from the raytracing simnulation and the actual images captured on the CCD camera at the plane of the camera chip (image focal plane of the rear lens), are illustrated in fig. 4.21. However both simulated and real images show narrowing of the SPCE ring in comparison to the SAF ring, the cross-section comparison of the ring profiles is very difficult since the images are obtained in a very different way. The images of the off-axis elements are cushion-distorted as a consequence of a wide, non-axial incident beam and lens with large numerical aperture. As shown in table 4.2, all fluorescence rings contain equal amount of power, apart from the fractional losses on the outer elements caused by reflection and geometrical constraints.

4.4.3 SPCE and SAF detection: illumination considerations

As stated in section 4.4.2 the fluorescence pattern detected by the camera CCD chip is an integral of the fluorescence emission pattern emitted from a single point (which is an approximation of a single dipole emitter) over the source area and imaged by the imaging

system. In the model, an equal contribution of the fluorescence sources was assumed irrespective of their position within the ring of illumination.

The assumption that fluorescence is emitted from the full ring of illumination (fig. 4.18a) is only valid for the configuration without metallic film (TIRF-SAF scheme), where the evanescent field at the interface is excited by all angles of incidence above the critical angle. As mentioned in section 2.2.1, the intensity of the evanescent field decreases with increasing angle of incidence, but is relatively independent on the polarisation of the incident wave.

In the SPR-SPCE scheme fluorescence will no longer be generated from the full ring of illumination as in the TIRF-SAF scheme, since the evanescent field will not be excited by the full angular range of the incident light. Most of the light incident upon the layered structure will be reflected except the narrow beam around the plasmon resonance angle. As shown in fig. 4.22 the area of illumination thus reduces to a narrow ring with radius corresponding to the θ_{SPR} and with the thickness equal to the propagation length of surface plasmon at the metal-water interface.

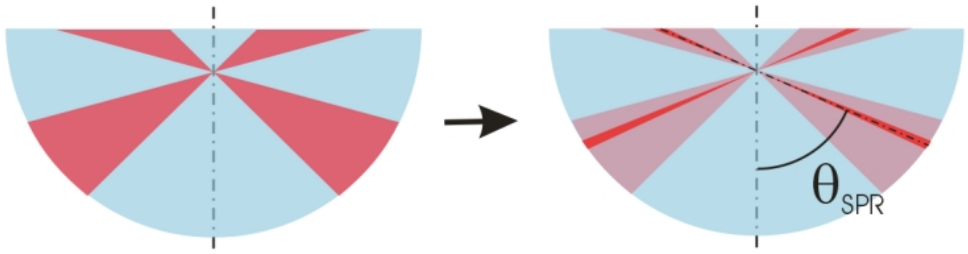

Figure 4.22: Reduction of the full ring of illumination into a narrow ring when the metallic film is present on the paraboloids

It is interesting to find out whether the reduced area of illumination with the SPR-SPCE scheme is offset by the enhanced fluorophore excitation due to the surface plasmon. To estimate the ratios of the generated fluorescence from polymer/metal/water and polymer/water interfaces, several assumptions have been made. The amount of fluorescence generated from the respective area for each scheme is proportional to the excitation intensity. The magnitude of the electric field within both rings of illumination varies along their width, so for convenience it is substituted with a single, averaged value, characterising the entire ring. Equal strength of the electric field along the ring circumference is also assumed.

The plasmon propagation lengths at gold/water and silver/water interface for the laser wavelength (635nm) are $\sim 3\mu$m and $\sim 19\mu$m respectively [32]. If 50nm thick metal films are used, the plasmon resonance angles are θ_{SPR}=70° for gold and θ_{SPR}=68° for silver,

which makes the ratios of TIRF-SAF to SPR-SPCE illumination ring areas equal to ∼40 for gold and only ∼7 for silver. Averaged values of field enhancements at the metal/water interfaces, calculated from maximum enhancement factors shown on page 24, are ∼18 for gold and ∼45 for silver, whereas the averaged enhancement factor for the polymer/water interface is ∼2. The ratios of the products of field enhancements and surface areas suggest that a total excitation enhancement can be achieved with silver film. For gold, which was used in majority of our experiments, the total excitation field intensity is lower than in TIRF-SAF scheme by a factor ∼4. However, the presence of the additional dielectric layer (spacer and biomolecules) will mean that the actual field enhancement factor will be lower than that directly at the metal-water interface. Furthermore, the SP field intensity is not constant along the entire ring of illumination due to polarisation (discussed in section 4.4.4). Taking these facts into account it is possible to conclude that the total excitation intensity in the SPR-SPCE scheme will be at best comparable to that in the TIRF-SAF scheme for silver and several times lower for gold.

As suggested in section 4.4.2, in the SAF scheme the presence of the annular mask is essential for two reasons: to provide the surface-specific excitation and to block the fluorescence emitted below the critical angle. In the SPCE scheme, however, the need for the mask and therefore precise alignment with the chip can be avoided. This is schematically illustrated in fig. 4.23. The plasmonic structure comprising metal and dielectric film defines the SPR and SPCE angles and rejects light which fails to meet the plasmon-coupling condition. If the chip is illuminated by an expanded beam from below, but not modified by the annular mask, the excitation light comprises two components. The direct one, where some laser light, incident directly upon the metal film, passes into the sample volume, but is strongly attenuated by the metal film. Light which is reflected by the side face of parabola is mostly back-reflected by the metal film, except the narrow beam around θ_{SPR}. The second component provides the plasmon-enhanced excitation field for the fluorophores within its range. Fluorophores outside the lateral extent of the surface plasmon wave, both in the proximity of the metal film and in the bulk solution, are also excited, but only by the direct light, which is weaker by orders of magnitude. Only the fluorophores within the small distance from the interface (defined by the coupling length rather the the spatial extension of the SPR field as described in section 2.4.2) are back-coupled into the surface plasmon and detected as SPCE.

Furthermore, the back-coupling is significantly more efficient for perpendicular dipoles than for the horizontal ones. The amount of the plasmon-coupled fluorescence, which is produced

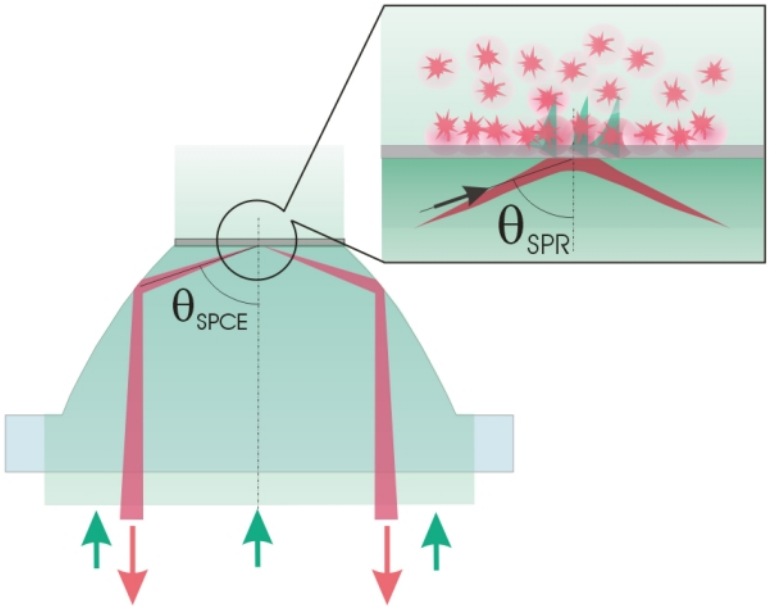

Figure 4.23: Schematic illustration of SPCE chip with wide-beam illumination from below without the annular mask. Strong coupling of fluorescence into SPCE only occurrs within the small volume defined by spatial extent of the SPR field and fluorescence coupling length

by the perpendicular dipoles (excited by the SPR field due to the vector matching) will be orders of magnitude stronger than that originating from the horizontal dipoles excited by the direct light.

Taking advantage of the inherent surface selectivity of the fluorescence plasmon coupling, excitation from above can be useful in some applications for its simplicity. Examples of the possible geometries are illustrated in fig. 4.24.

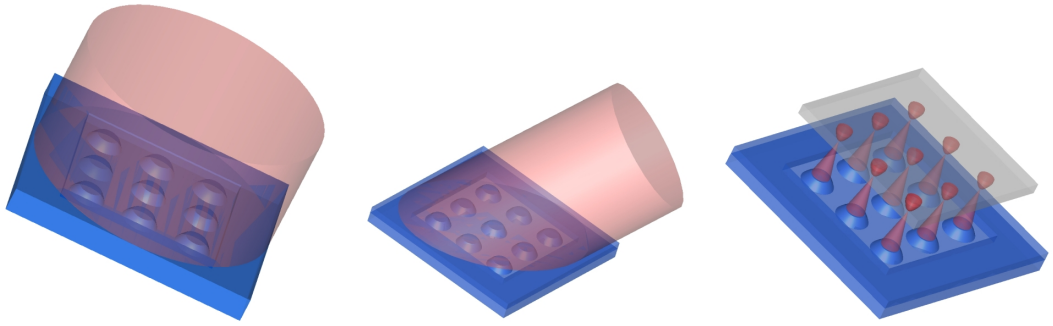

(a) (b) (c)

Figure 4.24: Examples of the geometries utilising chip illumination from above: (a) wide-beam illumination with normal incidence, (b) wide-beam illumination with offset angle of incidence and (c) individual illumination with an array of light sources

4.4.4 SPCE and SAF detection: polarisation considerations

Polarisation of the incident light and the emitted fluorescence is an important issue. As said in the previous paragraph, the TIRF-SAF scheme is independent of the polarisation of the incident light. The polarisation of the incident light has, however, an impact on the excitation efficiency of the bound fluorophores as both *s*- and *p*- polarisations of the incident light can excite the evanescent field. The overlap of the dipole momentum vector and the electric vector of the incident light means that dipoles with various orientations are efficiently excited as follows: horizontal dipoles with orientation normal to the plane of incidence with *s*-polarised wave and both horizontal and vertical dipoles with the dipole momentum vector lying in the plane of incidence with *p*-polarised wave. However, as discussed in section 2.3.3 the vertically oriented dipoles contribute to the SAF intensity significantly stronger that the horizontal ones.

Given that the chip is a 3D structure and that each of the nine elements has its own symmetry in general terms the plane of incidence is somewhat ill-defined. Due to the cylindrical symmetry of each of the nine elements the planes of incidence inside a single paraboloid form a continuous manifold of azimuthal vectors. If the incident beam is linearly polarised, following the total internal reflection at the side face of parabola the polarisation varies from *p*- to *s*- depending on the azimuthal angle referenced to the orientation of the polarisation vector of the incident wave. The total internal reflection induces a phase shift, which renders the manifold of the incident waves generally ellipticaly polarised. The amount of the phase shift depends on the angle of incidence. Since the polarisation of the beam

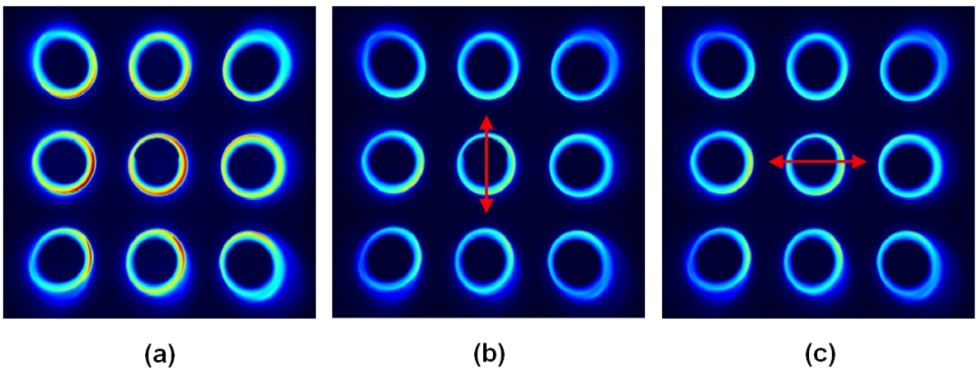

Figure 4.25: False colour images of SAF radiation observed through a linear polariser. (a) no polariser, (b) and (c) with polariser. Arrow denotes the orientation of the polarisation axis of the polariser

incident upon the parabola-water interface is generally elliptical, it can be assumed that in the TIRF-SAF scheme all the dipole orientations are excited uniformly. The molecules, immobilised on the surface, possess certain rotational degree of freedom, so their orientation,

averaged over the integration period (0.05-0.1sec), can be assumed to be isotropic. The dipoles thus emit both *p*- and *s*-polarised radiation. Since all polarisations are also transmitted by the interface, the detected SAF radiation is therefore unpolarised. This means that the fluorescence rings shape are independent on the polarisation axis of apolariser, if this is placed into the fluorescence signal path. This fact was verified experimentally by inserting a linear polariser between the imaging lenses with results shown in fig. 4.25. The independence of SAF polarisation and relative intensity on polarisation of the incident light was confirmed by carrying out a full set of measurements also with varying orientation of the linearly polarised laser.

In the SPCE scheme, not all polarisations of the incident waves are suitable for fluorophore excitation since surface plasmons can only be excited with *p*-polarised waves. Since the complex wave reflected from the parabola side face is elliptically polarised, it is possible to excite a surface plasmon at the metal-water interface, where only the component of the electric field vector projected onto the plane of incidence is utilised for SP excitation. When the illumination is done with linearly-polarised laser beam (as is in the chip reader), the intensity of the *p*-polarised component is highest in the direction of the polarisation vector of the incident wave. Consequently the excitation intensity is not uniform along the ring of illumination (reaching almost zero in the plane perpendicular to the polarisation axis of the laser) which results in a loss of some fluorescence signal. The optically most efficient solution to overcome this issue is to illuminate each element individually with a radially-polarised beam (electric vector pointing towards the centre of the beam for each azimuthal angle as illustrated in fig. 4.26). This solution is however impractical, bulky and expensive. Somewhat less efficient, but still superior to illumination with linear polarisation is to employ a circularly polarised beam. As the electric vector sweeps through all planes of incidence uniformly with period comparable to the absorption transition time ($\sim 10^{-15}$sec) it is capable to excite surface plasmons along the whole ring of illumination in times shorter than the average

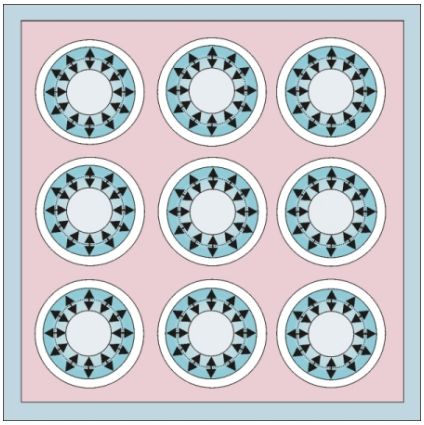

Figure 4.26: Orientation of the polarisation vectors of the light beams for most efficient excitation of SPs in the parabolic biochip. Also polarisation of plasmon-coupled fluorescence when observed from below

fluorescence emission lifetime ($\sim 10^{-9}$sec). However this needs to be investigated experimentally.

The electric vector of the excited surface plasmon wave is oriented normally to the interface, thereby efficiently exciting dipoles with the dipole momentum vector oriented perpendicular to the interface over parallel ones. The molecules with vertical orientation thus almost exclusively contribute to the plasmon-coupled fluorescence intensity. As mentioned in section 3.4.2 plasmon-coupled fluorescence originating from vertical dipoles is emitted into each azimuthal angle with equal intensity and with *p*-polarisation. Not surprisingly, the plasmon-coupled fluorescence emerging from each element is thus almost radially polarised when observed from below. This is illustrated in fig. 4.26. This fact was experimentally verified with result shown in fig. 4.27. The intensity along the fluorescence ring varies when

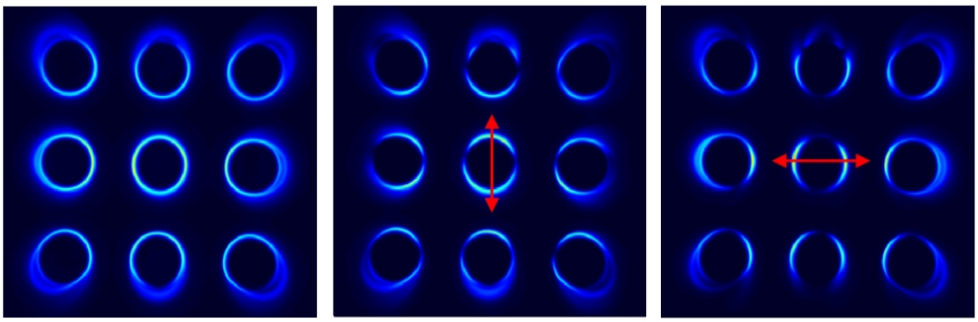

Figure 4.27: False colour images of SPCE radiation observed through a linear polariser. (a) no polariser, (b) and (c) with polariser. Arrow denotes the orientation of the polarisation axis of the polariser

the polarisation axis is rotated, with maximum in the direction parallel the the polariser orientation and zero in the perpendicular direction. Measurements with more polariser orientations were taken with the same result. The orientation of the laser polarisation was also rotated, but neither polarisation nor relative intensity of the fluorescence rings varied. This observation is in accordance with considerations described above and also testifies that the detected fluorescence originates from plasmon coupling.

4.5 Fluid delivery: flowcell design

To demonstrate one of major advantages of SPCE, its sensitivity to fluorescence emission events originating from the close vicinity of the metallic film, a flowcell containing a single flowchannel (fig. 4.28a) was designed to faciliate delivery of a liquid sample to the recognition areas of the parabolic elements. The flowcell is fabricated in house from a clear,

1.5mm thick polycarbonate slide with dimensions 20×20mm matching those of the chip. The channel, which is 1mm wide and 150μm deep and containing small reservoirs at the positions corresponsing to each parabolic element has an active length (distance along the channel from the first to the nineth reservoir) of 5.5cm. The active channel volume is ∼10μl. Holes, drilled into two corners of the flowcell and with nozzles attached, serve as channel inlet and outlet.

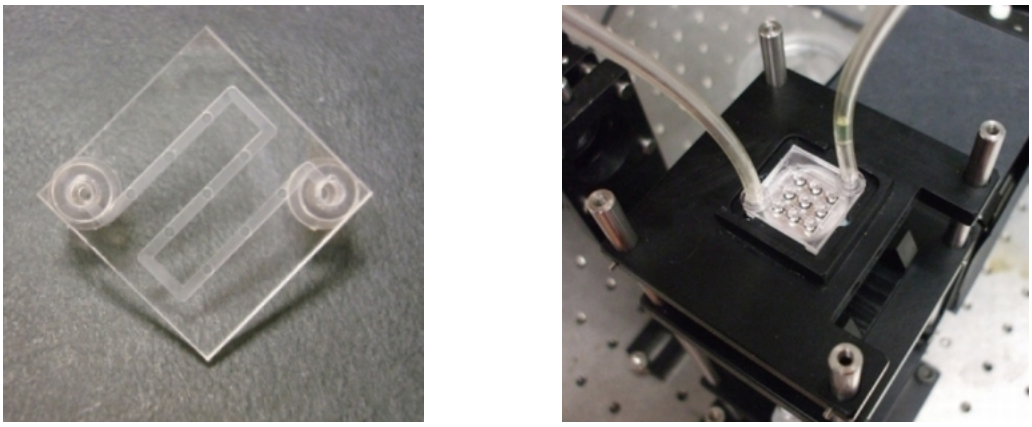

(a) (b)

Figure 4.28: Photo of the flowcell (a), detail of chip-flowcell inserted into the reader chip slot (b)

The flowcell is attached to a chip using pressure-sensitive adhesive sheet (PSA) containing nine ∼1mm in diameter laser-punched holes with the same pitch as that of the parabolic elements. The assembly is accomplished in two steps: first, PSA is attached to a clean and plasma-treated flowchannel so that the holes in it coincide with the reservoirs inside the flowchannel. The flowcell is subsequently manually attached to a chip. Precise alignment of a flowcell to a chip is essential. The diameter of the holes is smaller then the diameter of the top of the chip and the PSA serves as a gasket, preventing leakages into the chip which result in loss of the chip functionality. Figure 4.28b shows an image of the flowcell attached to a chip and placed in the chip slot of the chip reader.

4.6 Model hIgG bioassay with plasmonic structure

4.6.1 Surface functionalisation and immobilisation of the capture antibodies

The strategy for immobilisation of the primary antibody layer on top of the PEL multilayer is based on coupling of reactive nucleophile functionalities from protein molecules (most

commonly amine groups in lysine residues) to carboxylic groups on the surface, which are activated with EDC/NHS. Briefly, EDC serves as an activator, creating a reactive O-acyl isourea intermediate with the carboxylic group, which is then reacted with a suitable nucleophile. The intermediate (product of the first reaction illustrated in fig. 4.29) is extremely reactive and water hydrolysis rapidly transforms it back to carboxylic acid, unless another competing nucleophile is present. NHS was found to be a suitable reagent, forming an active ester derivative that is stable for several minutes to hours (second reaction in fig. 4.29).

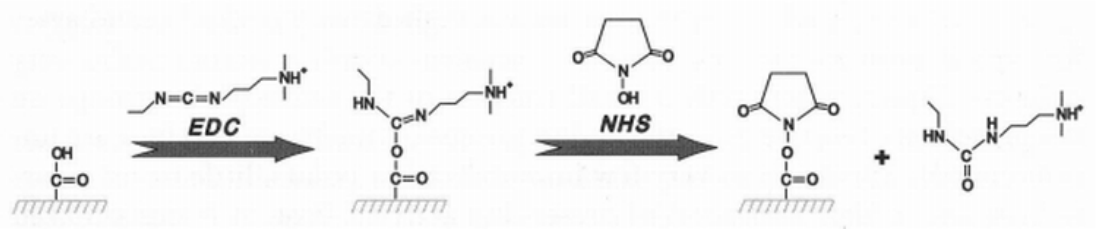

Figure 4.29: Activation sequence of the carboxylic acid group with EDC/NHS (adopted from [33])

Coupling to the active esters can be carried out under various conditions. The one used in this experiment was adopted from [34] and is used by Biacore to immobilise proteins onto a carboxymethylated dextran coupling matrix [35]. This approach relies on electrostatic attraction of the proteins and an NHS-activated carboxylated surface, where a portion of the carboxylic groups from PAC remains negatively charged (fig. 4.9f on page 72). The ratio of NHS-activated and unreacted carboxylic groups depends on ambient pH and pKa of the carboxylic group in the polyelectrolyte environment. To facilitate the binding reaction via the above described mechanism, proteins are prepared in a buffer with pH lower then is the isoelectric point of the protein molecule, thus rendering the reactive amino groups positively charged (fig. 4.9g). The high local surface concentration of the protein is obtained due to the strong electrostatic attraction. This favours a reaction of nucleophilic amines on the proteins over water hydrolysis of the ester.

Experimental

Freshly prepared 400mM EDC and 100mM NHS aqueous solutions were mixed in a 1:1 ratio just prior to the activation step. 1μl of the mixed 50mM NHS/200mM EDC solution was dropped on top of each parabolic element and left for 10 minutes to incubate in a humid atmosphere at room temperature. The chips were then rinsed in dH2O, dried with N_2 and used immediately.

Prior to the full bioassay experiments, a test in order to establish the optimum spotting technique was carried out. Labelled antibodies (AlexaFluor 647 goat-developed anti-human IgG) diluted in acetate buffer (pH=4.5) to a working concentration of 200μg.ml^{-1} were spotted onto the NHS-functionalised surface either manually (micropipette) or by a spotter robot (sciFLEXARRAYER, Scienion AG, Germany). Unlike the manual spotting, the spotter offers superior reproducibility in terms of spot position and dispensed volume. The volumes of liquid dispensed per element were 1.5μl for manually-spotted and 0.4μl for the machine-spotted chips. The chips were incubated for 1 hour in a humid atmosphere, inserted into glass vials containing washing solution and washed for 10 minutes in PBST and 5 minutes in dH2O by means of shaking on an orbital shaker and dried.

The comparison between the manually and machine-spotted proteins shows comparable element-to-element reproducibility (fig. 4.30). Although the latter method showed slightly higher Ab surface densities (larger fluorescence) and lower element-to-element signal fluctuations, the former method was chosen for its simplicity without any significant compromise on the coating quality. Further tests on manually spotted chips were performed by varying the volume of the protein solution dispensed (0.8-1.5μl) and incubation time (1 to 4 hours) and showed little fluorescence intensity variations with varying volume and incubation time.

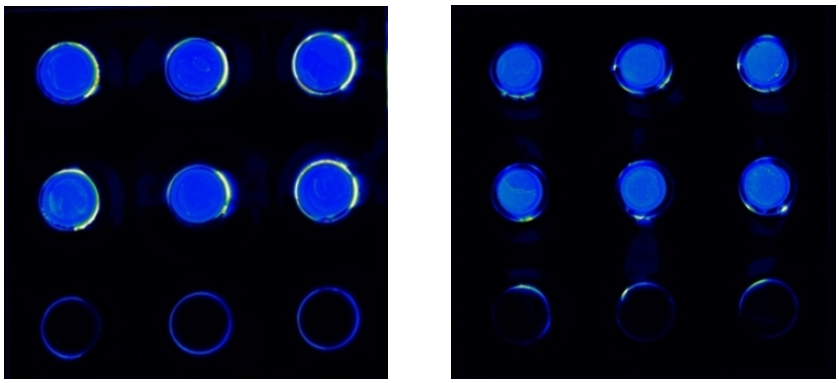

(a) (b)

Figure 4.30: Fluorescence scanner images of manually (a) and machine (b) spotted labelled antibodies onto NHS-functionalised surface. The deviation from the machine-produced spots is below 5% and from manual spots about 7%. The bottom row is left blank as negative control

4.6.2 Proof-of-concept: model hIgG sandwich immunoassay

Having established the cAb spotting technique, the following liquid volumes and incubation times were used throughout all incubation steps: 1μl of protein solution onto each element

and 1 hour incubation in a humid atmosphere at ambient temperature (20-23°C), followed by 10min washing in PBST and 5min washing in dH2O using the orbital shaker and drying with N_2. Fresh proteins (all from Invitrogen, USA) prepared shortly before the experiment from frozen aliquots by dilution in appropriate buffer were also used throughout.

The solution of primary polyclonal antibodies (goat-developed anti-human IgG) was prepared by dilution from a 2.3 mg.ml^{-1} aliquot to the working concentration of 200μg.ml^{-1} in acetate buffer at pH=4.5 and spotted onto all parabolic elements. Followed by the washing step the unreacted surface was blocked with 1% solution of BSA in PBS.

The analyte antigen (human IgG) concentration was chosen to span a broad range between 200μg.ml^{-1} down to 0.001μg.ml^{-1}. The dilution to an actual concentration used was carried out in series starting with the basic working concentration 200μg.ml^{-1}, obtained by dilution from a 2.5mg.ml^{-1} aliquot in PBS. This gives 0.5ml of solution at the basic working concentration. In order to avoid inaccuracies in analyte concentration arising in the dilution series, a 1:9 dilution ratio scheme was employed; with 1 part (50μl) of protein solution injected into 9 parts (450μl) of PBS and stirred thoroughly. The two one-multiple and two-multiple series dilutions were performed separately to maintain the dilution in the logarithmic scale. The first, one-multiple series comprised concentrations 10μg.ml^{-1} to 0.001μg.ml^{-1}, the 2-multiple one 200μg.ml^{-1} to 0.002μg.ml^{-1}, which means 11 concentrations in total. Six elements on each chip were spotted with a single antigen concentration (first and third column), with the central column spotted with PBS only and thus left as a negative control. One chip was prepared at each Ag concentration. The final step comprised spotting the elements containing bound antigen with the labelled counterpart (AlexaFluor 647 anti-human IgG) at concentration 100μg.ml^{-1} in PBS. The elements in the central column were again spotted with PBS solution.

The fluorescence measurements were performed in two steps. First, the fluorescence scanner measurements showing the fluorescence intensity emitted into free space and a spatial distribution of bound fluorophores were carried out. Depending on the Ag concentration, two gain settings of the PMT in the fluorescence scanner were used to obtain a detectable signal, namely at low concentrations. These measurements were taken in air. The chip reader measurements record the plasmon-coupled fluorescence originating from the fluorophores within the illuminated area. A droplet of buffer solution with n$\sim$1.33 was dispensed onto each element. The integration time of 0.5sec suited the entire analyte concentration range, preventing camera saturation for the highest and still discriminating signal from background for the lowest analyte concentration. The fluorescence scanner and chip reader camera im-

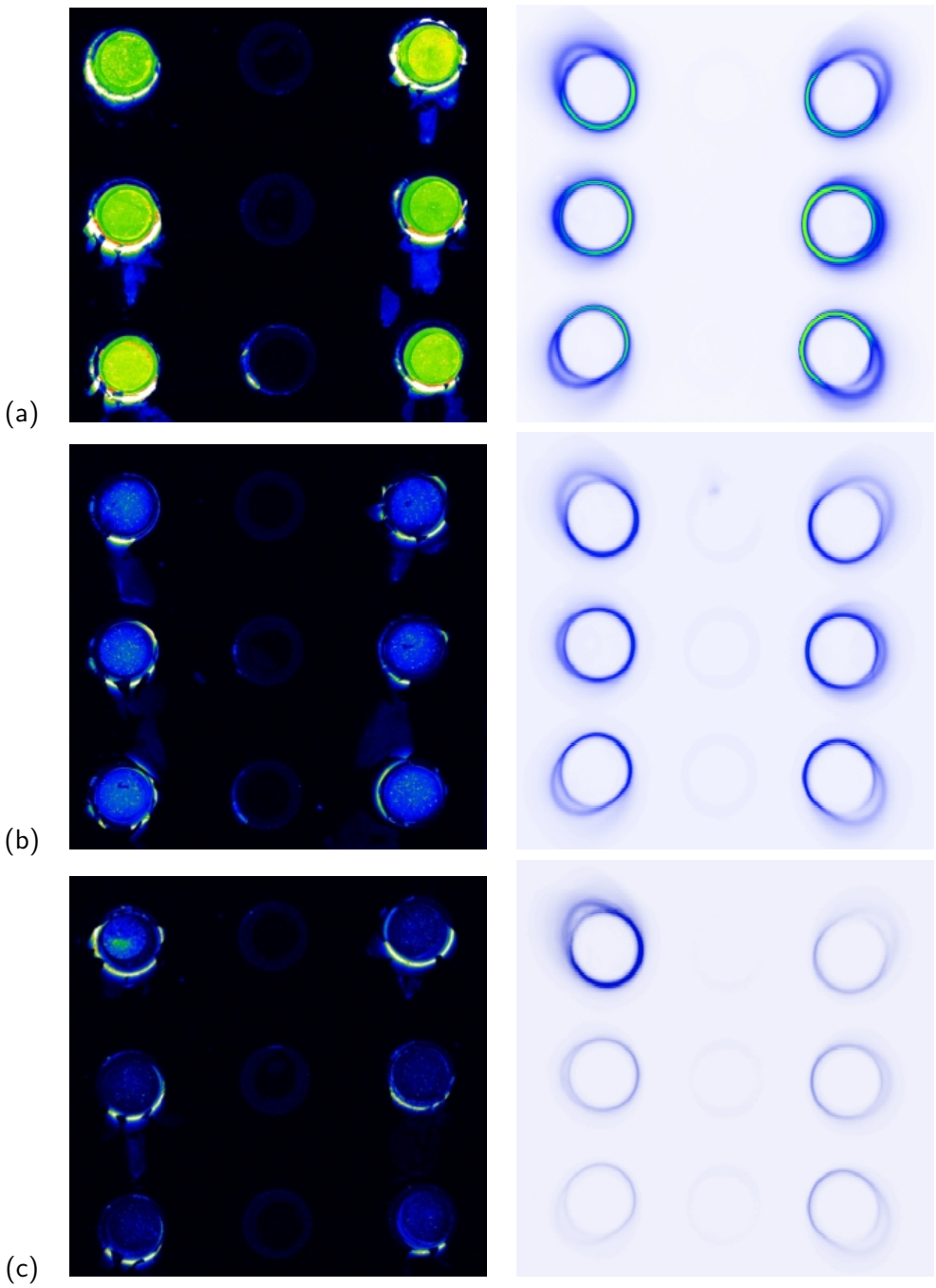

Figure 4.31: Fluorescence scanner (left column) and chip reader (right column) images (displayed in false colours) from the sandwich assay for hIgG concentration (a) 20μg.ml^{-1}, (b) 1μg.ml^{-1} and (c) 0.1μg.ml^{-1}

ages for three analyte concentrations (20, 1 and 0.1μg.ml^{-1}) are shown in fig. 4.31. Image analysis was performed on both fluorescence scanner and chip reader measurements in order to obtain quantitative values of the fluorescence intensities. In the former case, using the built-in scanner software function a square is drawn around the paraboloid centre (0.1mm^2, i.e. approximately 300μm edge) giving the intensity value within. The SPCE intensity is extracted from the image by drawing a circle with diameter 70 units around the

fluorescence ring (fig. 4.16), where each unit corresponds to one pixel on the camera. The fluorescence intensity for each analyte concentration is calculated as the mean of the intensities from each element. Distant values (such as that in top left element in fig. 4.31c) are excluded from the mean calculation. As the total fluorescence emitted from a unit recognition area is proportional solely to the number of Ag-Ab* conjugates (if non-specific binding is omitted) it is therefore obvious that the SPCE and free-space intensity will be in correlation. This is shown in fig. 4.32.

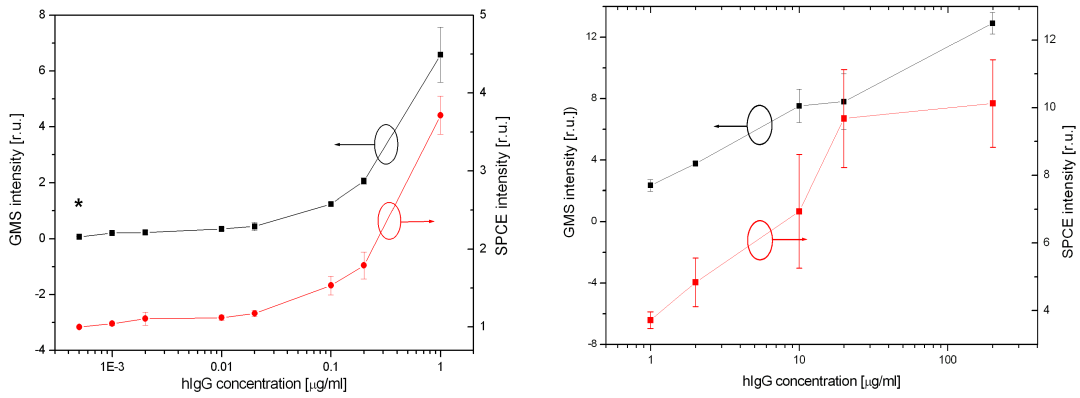

Figure 4.32: Correlation of free-space and SPCE intensity plotted for (a) low (0.001-1μg.ml^{-1}) and (b) high (1-200μg.ml^{-1}) hIgG concentration. The full concentration range was divided into two graphs as two different scanner gain settings were used. The GMS intensities in each graph denote the actual relative intensity values for each gain setting, the SPCE intensities are expressed as ratio fluorescence/blank. The asterisk denotes the blank signal

The dose dependence of the SPCE fluorescence signal versus the antigen concentration is shown in figure 4.33. Experimental datapoints for each Ag concentration are expressed as a ratio of the total signal (i.e. corresponding fluorescence signal plus background signal) and a background signal (obtained from the negative control on the chip with the lowest Ag concentration). This background signal is equal to the sum of the dark frame signal (with laser light off) and the reflection and scattering signal from the chip and the optical elements. The issue of background on limit of detection will be briefly addressed later in the text. The experimental dose profile was fitted with a sigmoidal curve (eq. (4.2), solid line in the graph) with resultant R^2=0.984.

$$y = \frac{A_1 - A_2}{1 + \left(\frac{x}{x_0}\right)^p} + A_2 \tag{4.2}$$

The limit of detection and quantification of the model system have been determined from both experimental data and the fitting curve. Defining the LOD as concentration c_L of analyte corresponding to the smallest measured signal Y_L that can be detected with reasonable certainty, c_L can be obtained from [33]

$$Y_L = Y_{blank} + m \cdot \sigma_{blank} \tag{4.3}$$

where Y_{blank} is the mean of the blank and σ_{blank} is the standard deviation of the blank measurements, m is the numerical factor chosen according tho the confidence level desired. For LOD, The confidence value for LOD is usually chosen as $m = 3$, whereas analyte quantification level (LOQ) is accepted for $m = 10$.

Taking the Y_{blank}=1 and σ_{blank}=0.003, the LOD and LOQ values obtained from both the experiment and the fitting curve are summarised in table 4.3. In the former case, the limit response values as defined by eq. (4.3) were compared with the actual mean signal response obtained from experiment. Due to very low blank variance (0.3%), both LOD and LOQ were found to equal to the lowest concentration used in the experiment (1ng.ml^{-1}). In the latter case, the concentration value x was sought by substitution of the parameters obtained from fit (listed in top figure 4.33) into the eq. (4.2); with mean LOD and LOQ obtained from the mean parameter values and the minimum and maximum calculated from the variations of the fitting curve parameters.

	Experimental [ng.ml^{-1}]	**Calculated from fit** [ng.ml^{-1}]		
		mean	min	max
LOD	1	1.0	0.2	4.1
LOQ	1	2.7	0.6	8.7

Table 4.3: Limit of detection and quantification of the model system obtained from experimental data and calculated from the fitting curve

From the results shown in table 4.3, the worst-case LOD and LOQ are equal to 4.1ng.ml^{-1} and 8.7ng.ml^{-1}, respectively. Throughout the entire set of experiments it turned out that the the largest proportion of the background signal originated from the dark frame (ratio of dark-frame signal to background from the blank biochip was $\sim 13 : 2.5$). This is rather surprising as the CCD chip on the camera is cooled. Since the dark-frame signal seemed to be constant irrespective of the integration time, it suggests that this could be caused by a software issue and the method of calculating the fluorescence signal. However sufficient for the demonstration purpose a more sophisticated method of image analysis needs to be

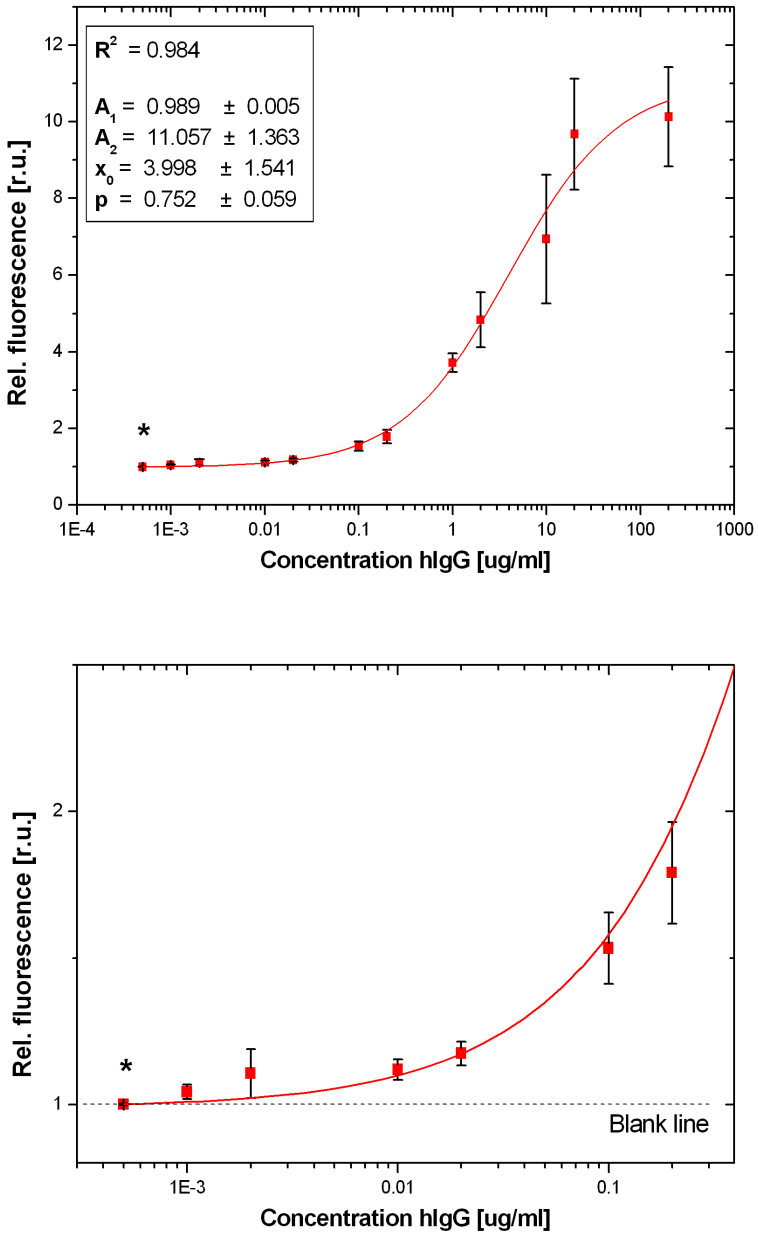

Figure 4.33: Normalised dose dependence of the SPCE fluorescence signal versus the hIgG concentration. Top graph shows full hIgG range and the bottom graph detail of low concentration range with a blank line at unity. The dots show the experimental data, solid line represents the sigmoidal fit. The blank signal (marked with an asterisk above the data point) was obtained as mean of the blanks from the chip with the lowest Ag concentration value. The parameters of the fitted curve are displayed in the top graph

implemented. For the sake of further decreasing of the LOD value, it is important to look more deeply into the various sources of background signal (originating from the biochip, detector, non-specific binding, etc.). The first step would be to determine the limit of detection of the platform itself (by employing a well established, high-affinity and high specificity assay) or by depositing a fluorescent dye onto the functionalised surface with a

known surface density (number of dye molecules per square area). For real applications the method of the fluorescence detection (camera or an array of 'point' detectors and their specifications) needs to be addresses with respect to the particular application (analyte type and relevant range of concentrations in real samples, Ab properties, fluorophore used etc.)

4.7 Real-time binding: direct assay

Demonstration of real-time binding of free analyte present in solution to a surface-immobilised receptor was performed by means of the fluid delivery system as described in section 4.5. All elements of a clean chip were coated with 50nm silver, followed by deposition of five PEL bilayers. The receptor (human IgG) was immobilised by means of adsorption onto the surface of the elements 1-3 (fig. 4.34a) by incubation in the protein solution (50μg.ml^{-1} in PBS) for 30mins at 37°C, partly-immersed. Followed by gentle washing with PBS and deionised water, the surface was blocked by incubation of the fully immersed chip in 1% BSA in PBS. Having immobilised the receptor proteins, the flowcell was quicky mounted

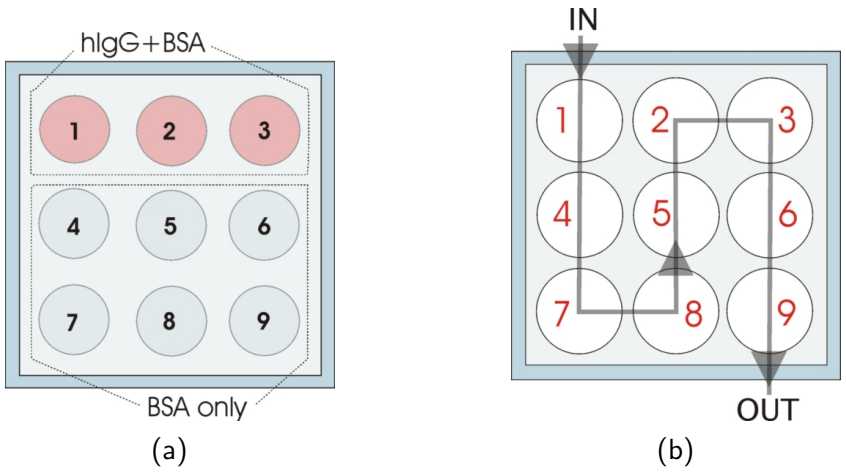

Figure 4.34: (a) Schematics of chip coating with proteins for binding kinetics experiment and (b) orientation of liquid flow on the chip

onto the chip (causing damage to the coating on the element 3) and the channel was filled with deionised water. Tubing was carefully connected to the inlet nozzle, inserted into the peristaltic pump head (MicroPulse 3, Gilson) and filled with the ligand solution (1μg.ml^{-1} of αhIgG* prepared in 0.1% BSA-PBS). Another tubing connected to the outlet nozzle served to drain the waste solution. No leakage of a liquid from the flowchannel into the chip was observed during the course of the experiment. Orientation of the flow with respect to the parabolic elements marking is illustrated in fig. 4.34b.

The peristaltic pump rate was set at 0.07rpm and with inner tubing diameter 2.06mm gave

a flow rate 7.6μl.min^{-1}. Compared to the channel volume of $\sim$10μl, liquid along the channel is completely replaced with a fresh one in just over a minute. With a sufficient flow it is assumed that the the boundary layer adjacent to the capture protein binding sites is constantly replenished with fresh labelled proteins thus keeping its concentration constant. A typical temporal profile of the binding curve, described by pseudo-first order kinetics [33], is therefore expected. The first fluorescence image was taken just before the protein solution entered the flowchannel and then every minute during the course of the binding process (fig. 4.35).

The time dependence of fluorescence signal is shown in fig. 4.36. The binding occurs on parabolic elements 1 and 2 as expected. The response on both elements was identical until a bubble appeared at paraboloid 1 as indicated in the figure, partially obstructing the recognition area. This resulted in deviated response compared to element 2, over which clean, bubble-free flow was maintained. No binding of labelled Ab to the surface-immobilised Ag was observed on the elements 3-9.

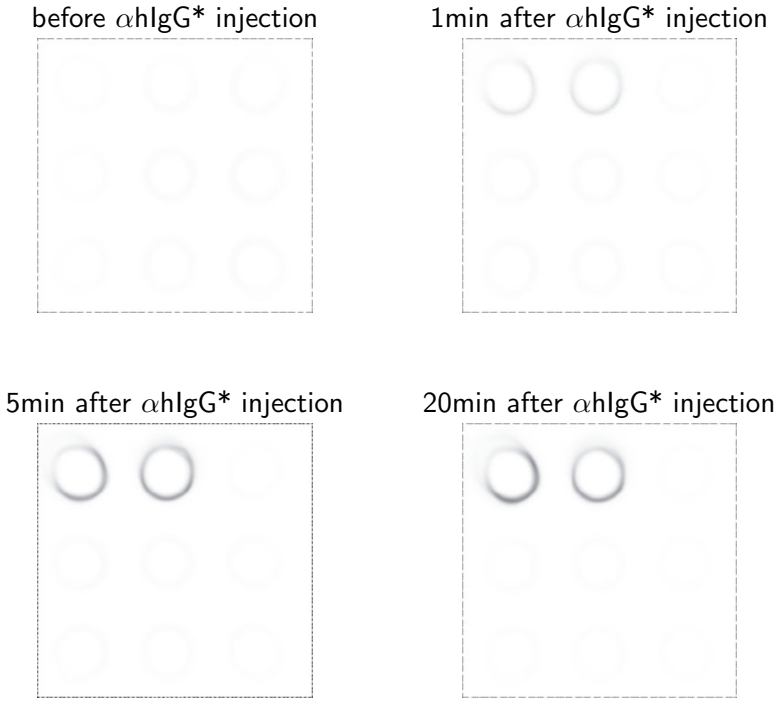

Figure 4.35: Chip reader images taken at various times of the binding process

After equilibrium was reached ($\sim$20mins), the inlet tubing was disconnected from the nozzle, emptied, rinsed, filled with dH_2O and carefully reconnected. Dissociation of the surface-bound antigen-antibody complex is represented by the decrease in the fluorescence signal, as seen in graph 4.36.

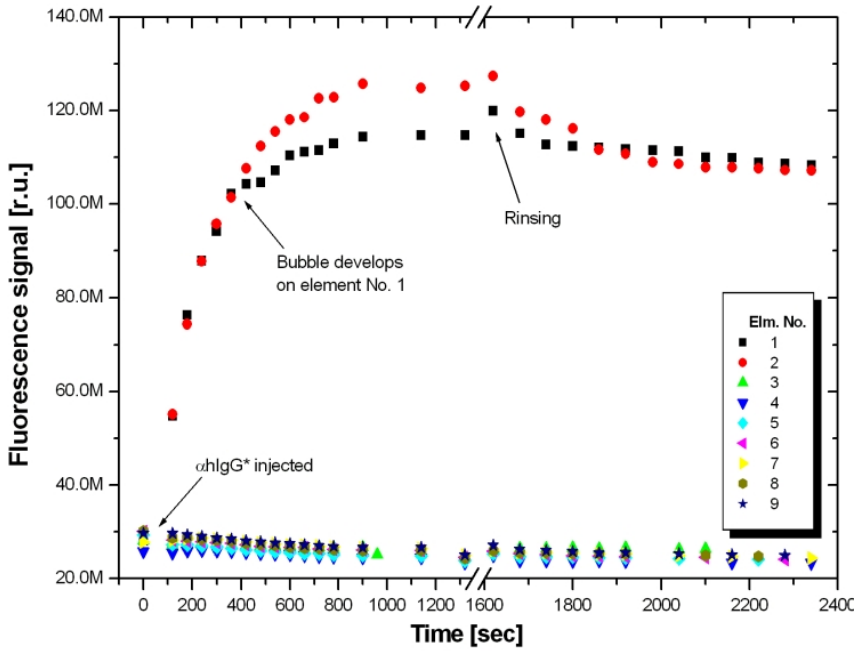

Figure 4.36: Real-time binding of αhIgG* to surface-bound hIgG. Binding reaction only occurrs at elements 1 and 2 as expected (damaged coating at parab. 3)

Although more experiments were to be carried out with a range of analyte concentrations and detection geometries, the high proportion of damaged chips (caused by damage to the coatings during incubations and flowcell assembly, leaks and mainly bubbles occurring in the flowchannel) meant that further experiments were suspended. This experiment, however, demonstrates the capability of the plasmonic structure integrated onto the chip to facilitate parallel real-time detection of the binding events.

4.8 Conclusions

This chapter dealt with integration of a plasmonic structure into an optical biochip designed as a mass producible, miniature, low cost and disposable array of high collection efficiency parabolic elements. The chapter is introduced with a description of a single parabolic element and how an array of such elements can be used as a mass producible biochip. It is also described how a plasmonic structure comprising smooth metal and dielectric films is integrated onto each parabolic element.

Raytracing analysis performed on both SAF emission and SPCE peak emission around 73° (model bioassay system) helped to specify required the dimensions of optical components and their maximum mutual distances. The analysis revealed that the shift of focus and associated modification of the fluorescence source area results in a loss of capability of a

parabola to redirect fluorescence emitted just above critical angle, where this effect is more pronounced as going further from the axis of a paraboloid. The design and assembly of the chip reader, compensating for the divergence of the fluorescence signal, is described along with the data acquistion and analysis software.

Practical aspects of a SPCE-based biochip system are discussed in detail. The aspect of material choice is addressed in terms of compatibility with the chip design and chemical stability of the coatings. It was shown that silver coatings exhibited lack of stability when exposed to saline solutions and were replaced with significantly more stable gold. Numerical models of the SPR dip/SPCE peak angle position performed for a range of metal layer types overcoated with a dielectric indicated that even the sandwich hIgG protein structure upon a 10nm-thick PEL film deposited on gold will not cause a shift of the plasmon angles which would exceed the cut-off angle of the chip and annular mask. Due to the presence of a metal film the area of illumination is reduced to a narrow ring with diameter corresponsing to the SPR angle. It is discussed that despite the reduced area from which fluorescence can be emitted this is counterbalanced by an enhanced SPR excitation field. Possible illumination geometries which may suit various applications are also depicted such as bottom illumination without a mask and a number of direct illumination schemes. The issues of polarisation of the excitation beam and the emitted fluorescence are broadly discussed. It is demonstrated experimentally that the plasmon-coupled fluorescence emerging from a single element of the chip is radially polarised.

In the final section, the development of a model hIgG-based sandwich bioassay is described. To immobilise capture antobodies onto a carboxylated surface a EDC/NHS chemistry is used, yielding good reproducibility of the capture Ab density. The hIgG limit of detection obtained from experiment was 1ng.ml^{-1}. Real-time binding of labelled Ag to a surface--bound Ab was also observed demonstrating strong capability of the SPCE-based scheme to confine the detection volume to a close vicinity of a surface.

To my knowledge, this is the first demostration of an SPCE-based bioassay on a disposable and low-cost biochip platform.

References

[1] D. Axelrod. Total internal reflection fluorescence microscopy in cell biology. *Traffic*, 2(11):764–774, 2001.

[2] F. D. Stefani, K. Vasilev, N. Bocchio, N. Stoyanova, and M. Kreiter. Surface plasmon-mediated single-molecule fluorescence through a thin metallic film. *Physical Review Letters*, 94(2), 2005.

[3] J. Borejdo, N. Calander, Z. Gryczynski, and I. Gryczynski. Fluorescence correlation spectroscopy in surface-plasmon coupled emission microscope. *Optics Express*, 14(17):7878–7888, 2006.

[4] T. P. Burghardt, J. E. Charlesworth, M. F. Halstead, J. E. Tarara, and K. Ajtai. In situ fluorescent protein imaging with metal film-enhanced total internal reflection microscopy. *Biophysical Journal*, 90(12):4662–4671, 2006.

[5] L. Polerecky. *Optimisation of Multimode Waveguide Platforms for Optical Chemical Sensors and Biosensors*. PhD. Thesis, DCU Dublin, 2002.

[6] R. Blue, N. Kent, L. Polerecky, H. McEvoy, D. Gray, and B.D. MacCraith. Platform for enhanced detection efficiency in luminescence-based sensors. *Electronics Letters*, 41(12), 2005.

[7] J. Enderlein, T. Ruckstuhl, and S. Seeger. Highly efficient optical detection of surface-generated fluorescence. *Applied Optics*, 38(4):724–732, 1999.

[8] T. Ruckstuhl, J. Enderlein, S. Jung, and S. Seeger. Forbidden light detection from single molecules. *Analytical Chemistry*, 72(9):2117–2123, 2000.

[9] T. Ruckstuhl, M. Rankl, and S. Seeger. Highly sensitive biosensing using a supercritical angle fluorescence (SAF) instrument. *Biosensors & Bioelectronics*, 18(9):1193–1199, 2003.

[10] T. Ruckstuhl and S. Seeger. Confocal total-internal-reflection fluorescence microscopy with a high-aperture parabolic mirror lens. *Applied Optics*, 42(16):3277–3283, 2003.

[11] T. Ruckstuhl and D. Verdes. Supercritical angle fluorescence (SAF) microscopy. *Optics Express*, 12(18):4246–4254, 2004.

[12] D. Kurzbuch, J. Bakker, J. Melin, C. Jonsson, T. Ruckstuhl, and B.D. MacCraith. A biochip reader using super critical angle fluorescence. *Sensors and Actuators B*, 137(1):1–6, 2009.

[13] C.S. Burke, T. Ruckstuhl, and J. Moore. Optical probe; Patent application No. WO 2008/029298 A2, May 7 2007.

[14] C.S. Burke, J.P Moore, D. Wencel, and B. MacCraith. Development of a compact optical sensor for real-time, breath-by-breath detection of oxygen. *Journal of Breath Research*, 2, 2008.

[15] B. MacCraith and T. Ruckstuhl. Polymer biochip for detecting fluorescence; US patent application No. 20070262265, June 10 2006.

[16] L. I. Maissel and R. Glang. *Handbook of thin film technology*. McGraw-Hill, New York, 1983.

[17] A. Tronin, Y. Lvov, and C. Nicolini. Ellipsometry and X-ray reflectometry characterization of self-assembly process of polystyrenesulfonate and polyallylamine. *Colloid and Polymer Science*, 272(10):1317–1321, 1994.

[18] G. Decher. Fuzzy nanoassemblies: Toward layered polymeric multicomposites. *Science*, 277(5330):1232–1237, 1997.

[19] F. Caruso, K. Niikura, D. N. Furlong, and Y. Okahata. Ultrathin multilayer polyelectrolyte films on gold: 1. Construction and thickness determination. *Langmuir*, 13(13):3422–3426, 1997.

[20] J. B. Schlenoff and S. T. Dubas. Mechanism of polyelectrolyte multilayer growth: Charge overcompensation and distribution. *Macromolecules*, 34(3):592–598, 2001.

[21] G. Ladam, P. Schaaf, F. J. G. Cuisinier, G. Decher, and J. C. Voegel. Protein adsorption onto auto-assembled polyelectrolyte films. *Langmuir*, 17(3):878–882, 2001.

[22] D. S. Salloum and J. B. Schlenoff. Protein adsorption modalities on polyelectrolyte multilayers. *Biomacromolecules*, 5(3):1089–1096, 2004.

[23] X. C. Zhou and J. Z. Zhou. Protein microarrays on hybrid polymeric thin films prepared by self-assembly of polyelectrolytes for multiple-protein immunoassays. *Proteomics*, 6(5):1415–1426, 2006.

[24] S. D. Spillman, H. A. McEvoy, and B. D. MacCraith. Fabrication of substrate-independent protein microarrays using polyelectrolyte scaffolding. *Langmuir*, 25(3):1403–1411, 2009.

[25] D. Yoo, S. S. Shiratori, and M. F. Rubner. Controlling bilayer composition and surface wettability of sequentially adsorbed multilayers of weak polyelectrolytes. *Macromolecules*, 31(13):4309–4318, 1998.

[26] R. A. McAloney, M. Sinyor, V. Dudnik, and M. C. Goh. Atomic force microscopy studies of salt effects on polyelectrolyte multilayer film morphology. *Langmuir*, 17(21):6655–6663, 2001.

[27] J. Enderlein and T. Ruckstuhl. The efficiency of surface-plasmon coupled emission for sensitive fluorescence detection. *Optics Express*, 13(22):8855–8865, 2005.

[28] K.B. Lee, S.J. Park, C.A. Mirkin, J.C. Smith, and M. Mrksich. Protein nanoarrays generated by dip-pen nanolithography. *Science*, 295(5560):1702–1705, 2002.

[29] H. Xu, R. J. Lu, and D. E. Williams. Effect of surface packing density of interfacially adsorbed monoclonal antibody on the binding of hormonal antigen human chorionic gonadotrophin. *J. Phys. Chem. B*, 110(4):1907–1914, 2006.

[30] S. A. Zynio, A. V. Samoylov, E. R. Surovtseva, V. M. Mirsky, and Y. M. Shirshov. Bimetallic layers increase sensitivity of affinity sensors based on surface plasmon resonance. *Sensors*, 2(2):62–70, 2002.

[31] X. C. Yuan, B. Hong, Y. G. Tan, D. W. Zhang, R. Irawan, and S. C. Tjin. Sensitivity-stability-optimized surface plasmon resonance sensing with double metal layers. *Journal of Optics a-Pure and Applied Optics*, 8(11):959–963, 2006.

[32] J. Homola and S. S. Yee. Surface plasmon resonance sensors: review. *Sensors and Actuators B*, 54:3–15, 1999.

[33] J. Homola. *Surface Plasmon Resonance Based Sensors*, Volume 4 of *Springer Series on Chemical Sensors and Biosensors*. Springer, Heidelberg, 2006.

[34] B. Johnsson, S. Lofas, and G. Lindquist. Immobilization of proteins to a carboxymethyldextran-modified gold surface for biospecific interaction analysis in surface-plasmon resonance sensors. *Analytical Biochemistry*, 198(2):268–277, 1991.

[35] S. Lofas and B. Johnsson. A novel hydrogel matrix on gold surfaces in surface-plasmon resonance sensors for fast and efficient covalent immobilization of ligands. *Journal of the Chemical Society-Chemical Communications*, (21):1526–1528, 1990.

Chapter 5

Conclusions and future directions

The development of biosensor platforms for the detection and the monitoring of diseases is a very important area of research that can have a dramatic impact on the delivery of health services globally. Towards the successful adoption of these sensors, performance criteria such as sensitivity, low cost (preferably disposable) and ease of use have to be addressed. However, many of these requirements, such as low cost combined with high sensitivity, are challenging. Therefore, new technologies and approaches have to be continually developed and adopted to improve the performance of the sensors.

5.1 Summary of achievements

The aim of this work was to experimentally investigate the surface plasmon-coupled emission effect and its implementation into a disposable, low cost biochip platform.
Overall, the objectives of this work (as outlined in section 1.4) were achieved and are discussed below:

1. The methodology for investigation of the effect of metal-fluorophore separation was established by preparing samples with 50nm silver film and silica spacer with variable thickness and Cy5 dye immobilised on top. Direct comparison of SPCE fluorescence intensity with that without metal film was facilitated by preparing both silver-coated and silver-free areas on a single slide. Overall good control of the layer parameters was achieved. Although fluctuations in dye density were observed, this did not pose a problem.

   The angular profiles of plasmon-coupled emission were experimentally measured and compared with the theoretical model. Very good agreement was achieved with over-

all consistent result for molecules lying in the plane of the sample. The appearance of multiple peaks for larger spacer thicknesses was explained as a consequence of the constructive superposition of surface plasmon and waveguide modes in the spacer layer. It was also shown how dipoles with various orientations contribute to the resultant emission pattern. Again, the experimental result is consistent with the orientation of dipoles determined by the model.

The SPCE fluorescence intensity is compared to that detected without the metal film and expressed as a function of the spacer thickness. It is shown that an overall reduction of fluorescence is observed with SPCE, which is in accordance with a theoretical study published previously. In the single peak emission, the SPCE intensity is about 30% of the metal-free value for the experimental geometry and sample structure used and when measured over the angular range (-80°,80°). The fluorescence intensity is approximately doubled when compared with the SAF range only. Again, there is overall good agreement with the model result; however a discrepancy is present for larger spacer thicknesses due to the likely extra excitation of the fluorophores by the evanescent tail of the wave entrapped in the silica layer, which is not accounted for in the model.

2. A parabolic biochip, which is a generic platform for highly efficient detection of surface-generated fluorescence, has been modified for SPCE measurements by implementation of additional thin metal and dielectric layers. A metal film (Ag,Au) was deposited locally on top of the parabolic elements using a mask. A polyelectrolyte layer with thickness ∼9nm and refractive index ∼1.53 serves as a spacer layer and also facilitates covalent attachment of protein molecules.

   A chip containing the SPCE structure has been analysed from two perspectives. Firstly, the limits imposed by the layered structure (in terms of thickness and dielectric constants) to facilitate the angular range required for excitation and collection of fluorescence have been investigated. It is shown that the protein stack on a PEL and Ag/Au film will not cause excessive angular shift for excitation beyond the value delimited by the chip/mask, which is 80°. This cut-off angle corresponds to the minimum SPR angle for a gold film overlaid with a dielectric layer with total thickness 30nm and refractive index 1.53. In practice, the average thickness of the dielectric ranges between 20 and 30nm for the human IgG sandwich structure, which is perfectly compatible with the chip. Secondly the lack of stability of silver coatings on the polymer substrate is also demonstrated, which justifies the use of gold rather

then silver.

The shift of the parabolic focus resulting in loss of collimation of fluorescence generated from a spatially extended surface source is discussed. This has an impact on dimensions and distances of the optical elements of the read-out device. These have been determined with the aid of raytracing analysis. This analysis also revealed that all plasmon-coupled fluorescence is redirected by the parabolas (emission angle around 73°, corresponding to the real conditions described above), whereas a proportion of fluorescence is captured within the chip in the SAF scheme.

It is shown that the presence of the metal film leads to a reduction of the area of illumination due to plasmon coupling. It is also outlined that the reduction of the total excitation intensity due to the smaller area can be partly compensated by the enhanced excitation field. It is described how the SPCE chip can be operated without the annular mask without loss of performance due to properties of plasmon coupling.

The polarisation issues are discussed, both on the excitation and emission side. It is suggested that using a circularly polarised rahther then linearly polarised excitation beam should lead to larger fluorescence intensities achievable with the SPR-SPCE scheme.

Finally, design of the flowcell facilitating real-time kinetic experiments is described.

3. The immobilisation of biomolecules was facilitated by means of functionalisation of the polyelectrolyte layer with EDC/NHS-based surface chemistry. This allowed covalent immobilisation of the primary antibodies in a reproducible fashion.

   A dose response curve was established for the human IgG - anti-human IgG sandwich assay, covering the experimental analyte range 1ng.ml^{-1} to 200μg.ml^{-1}. The range stretches from the lowest detectable values to the saturation region. The experimentally obtained limit of detection was 1ng.ml^{-1}, which is also an experimental value of the quantification limit. The mean values, calculated from the sigmoidal fit, are 1ng.ml^{-1} for limit of detection and 2.7ng.ml^{-1} for limit of quantification, respectively. Binding of labelled antibody to the surface-bound antigen is demonstrated in real time, where the fluorescence was only detected from the specific binding reaction.

   This is, to my knowledge, the first demonstration of a SPCE-based bioassay on a disposable and low-cost biochip platform.

5.2 Future directions

The next stage of this work will follow on from the initial experiments on the SPCE chip. This will include optimisation of the the layered structure to maximise the fluorescence signal. The utilisation of various surface modifications will be further investigated (self--assembled monolayers, polyelectrolytes, branched polymers etc.). An experimental comparison of the achievable limit of detection will be carried out for SPCE- and SAF-based platforms and will be benchmarked against other existing biochip platforms.

The feasibility of the employment of techniques such as multi-wavelength discrimination and electrochemiluminescence into the SPCE biochip will be carefully assessed. The former technique would allow for multi-analyte detection or real-time comparison of binding activity of biomolecules. However spatial constraints imposed by the miniature design of the biochip may represent an obstacle. The advantage of ECL-based scheme is that no optical excitation is required which eliminates noise associated with the scattering etc. The metal film, used for plasmon mediation of fluorescence, also serves as an electrode. Modifications to the chip will be necessary to incorporate the interface facilitating charge transfer for excitation. The selection and synthesis of suitable labels, as well as robust metal coatings, will need to be addressed.

List of publications

Peer-reviewed publications:

1. M. Trnavsky, J. Enderlein, T. Ruckstuhl, C. McDonagh, and B.D. MacCraith. Experimental and theoretical evaluation of surface plasmon-coupled emission for sensitive fluorescence detection. Journal of Biomedical Optics, Vol. 13, No. 5, 2008

2. J.S. Yuk, M. Trnavsky, C. McDonagh, and B.D. MacCraith. Surface plasmon-coupled emission (SPCE) based immunoassay using a novel parabolic biochip. Submitted to Biosensors & Bioelectronics

Oral presentations:

1. M. Trnavsky, T. Ruckstuhl, and B. D. MacCraith. Evaluation of surface plasmon-coupled emission (SPCE) for fluorescence-based biochips. BiOS 2007 at SPIE Photonics West, 2007, San Jose, CA, USA

2. M. Trnavsky, O. Stranik, T. Ruckstuhl, J. Enderlein, and B. D. MacCraith. Optical biochip with a plasmonic (SPCE) structure. BiOS 2008 at SPIE Photonics West, 2008, San Jose, CA, USA

3. Monitoring of aromatic hydrocarbons in oil/water emulsion. Group project presentation at ASCOS 2006, Sept 4-8, 2006, Tihany, Hungary; won 2^{nd} price

4. Towards future biomedical diagnostics: Optical biochips and fluorescence enhancement. Invited lecture given 9 May 2007 at the FNSPE, Czech Technical University in Prague, CZ

Poster presentations:

1. M. Trnavsky, T. Ruckstuhl, C. McDonagh, and B. D. MacCraith. Surface Plasmon-Coupled Emission (SPCE) for fluorescence-based biochips. Poster at Europtrode VIII, 2-5 April 2006, Tübingen, Germany

2. M. Trnavsky, T. Ruckstuhl, C. McDonagh, and B. D. MacCraith. Optical Biochip Platform Based on Surface Plasmon-Coupled Emission (SPCE). Poster at Europtrode IX, 30 March - 2 April 2008, Dublin, Ireland

3. M. Trnavsky, J. Enderlein, and B. D. MacCraith. Experimental Study of Surface Plasmon-Coupled Emission (SPCE) for Sensitive Detection in Fluorescence-Based Biosensors. BOC poster competition, 16 November 2007, DCU Dublin, Ireland

Patent applications:

B. D. MacCraith, and M. Trnavsky. Optical Biochip Platform with Plasmonic Structure. Patent application PCT/EP2008/060621, 13 August, 2008